

**THE THEORETICAL FOUNDATION OF SPIN-ECHO
SMALL-ANGLE NEUTRON SCATTERING (SESANS)
APPLIED IN COLLOIDAL SYSTEM**

By

Xin Li

A Thesis Submitted to the Graduate
Faculty of Rensselaer Polytechnic Institute
in Partial Fulfillment of the
Requirements for the Degree of
DOCTOR OF PHILOSOPHY
Major Subject: NUCLEAR ENGINEERING

Approved by the
Examining Committee:

Li Liu, Thesis Adviser

Shekhar Garde, Member

Kenneth W. Herwig, Member

Amir H. Hirsa, Member

Michael K. Jensen, Member

Chwen-Yang Shew, Member

Rensselaer Polytechnic Institute
Troy, New York

May 2011
(For Graduation Aug 2011)

© Copyright 2011

by

Xin Li

All Rights Reserved

CONTENTS

LIST OF FIGURES	v
ACKNOWLEDGMENT	xi
ABSTRACT	xii
1. Introduction	1
1.1 Layout of the Thesis	1
1.2 Introduction of SESANS	1
2. Concepts and Theories	5
2.1 Contrast, Distribution and Correlation	5
2.2 SESANS Correlation Function	7
2.2.1 Multiple Scattering	8
2.2.2 Coherent and Incoherent Scattering	10
3. Interaction in Concentrated Spherical Colloid System	12
3.1 Decomposition of SESANS Correlation Function	13
3.1.1 Calculation of the Pair Distribution Function $g(r)$	17
3.1.2 Potential Models	19
3.2 SESANS Spectra for Different Interaction Potentials	21
4. Interaction in Soft Colloidal System	34
4.1 Core-Shell Structure	35
4.2 Soft Colloidal Structure	40
5. Contrast Variation in SESANS	49
5.1 Create a Contrast	53
5.2 Sensitivity to the Geometric Shape	57
LITERATURE CITED	64
APPENDICES	
A. Mathematical Transforms in SESANS	70
B. Data Statistics in SESANS	72

C. SESANS Correlation Function for Dumbbell	74
D. SESANS Correlation Function for Soft Colloid	81
E. Scattering Amplitude for Icosahedron	88
F. Issues about the Structure Characterization in Metallic Systems	91
G. Issues about the Partial Strucutre Factor in Binary Hard Sphere System . .	94
H. List of Publications	98

LIST OF FIGURES

3.1	SESANS spatial correlation functions of hard sphere colloidal suspension with volume fraction $\phi = 0.2$. The solid line is the normalized SESANS spatial correlation function $G(z)$, the dotted line is the auto correlation function $G_{auto}(z)$, the dashed line is the correlation of the excluded volume $\phi G_{excl}(z)$, and the dash dot dot line is the structure correlation function $\phi G_{struct}(z)$. The $g(r)$ used in $G_{auto}(z)$ is calculated from the solution of OZ equation with PY closure.	26
3.2	The interaction potential models used in the calculation of this study. (a) hard sphere (HS) potential, (b) adhesive hard sphere (AHS) potential, (c) screened Coulomb (SC) repulsion and (d) two-Yukawa (TY) potential.	27
3.3	Calculated small angle coherent scattering cross sections $I(Q)$ of colloidal suspensions with different potential models displayed in Figure 3.2, along with the form factor $P(Q)$ (dotted lines) and the structure factor $S(Q)$ (dashed lines). In this calculation, the colloidal volume fraction ϕ is set at a constant value of 0.2. The corresponding potential parameters used in the calculation are also presented.	28
3.4	The dependence of the partial SESANS correlation functions $G_{11}(z)$ and its structural component $G_{11struct}(z)$ (inset) on the concentration of the secondary phase of small particle 2. The solid line gives the reference correlation functions of the colloidal suspensions without the presence of particle 2. Upon the increase of the second phase concentration, the attraction due to the depletion force is progressively strengthening which is reflected in the enhancing correlation within the range of $z/R_1 < 3$	29
3.5	$G(z)$ of a colloidal suspension with adhesive hard sphere (AHS) potential whose parameters are specified in the figure. Similar to the features of Figure 3.4, the short range ($z/R < 3$) correlation is progressively enhanced upon increasing the attraction.	30
3.6	The structure factor $S(Q)$, pair distribution function $g(r)$ and SESANS spectrum were calculated with the same parameters selected in the paper from Uca and coworkers. (a) $S(Q)$ in the regular Q range, (b) $S(Q)$ in high Q range, in which the structure factor derived by Menon [25] has an enormous oscillation, (c) the pair distribution function $g(r)$ in which the divergence is observed, (d) SESANS spectrum $G(z)$. The negative part of the diverging $g(r)$ renders the decline of $G(z)$	31

3.7	$G(z)$ for a colloidal suspension with screened Coulomb (SC) repulsion. The screening length Z_1^{-1} is fixed at 0.2. With the increase of repulsion strength K_1 , the fluctuation of $G(z)$ becomes more pronounced.	32
3.8	The dependence of $G(z)$ for a colloidal suspension with Two-Yukawa (TY) potential as a function of short-range attraction with a fixed repulsion. Detailed description is given in the text.	33
4.1	The semilog plots of the SANS coherent scattering cross section $I(Q)$ (solid lines), the form factor $P(Q)$ (dashed lines) and the structure factor $S(Q)$ (black dotted lines) for the uniform hard spheres (black) and spherical shell (red). The radius of the hard sphere R is identical to the outer radius of the shell radius. The volume fraction ϕ is set to be 0.2 in the calculation. The ratio of the shell thickness δ to R is 0.1. At low Q , $I_{SS}(Q)$ and $I_{HS}(Q)$ are seen to be characterized by a single peak originating from the suppression of scattering at $Q = 0$ by the structure factor, $S(Q)$	36
4.2	The SESANS correlation function $G(z)$ for hard sphere (a) and impermeable spherical shell (b) calculated based on the same structural parameters used in Figure 4.1. As shown in the inset of Figure 4.2(b), although $I_{SS}(Q)$ is seen to be qualitatively similar to $I_{HS}(Q)$ (Figure 4.1), $G_{SS}(z)$ is found to be characteristically different from $G_{HS}(z)$. The comparison of $G_{HS}(z)$ (black solid line) and $G_{SS}(z)$ (red solid line) is given in the inset of Figure 4.2(b). The observed difference, as discussed in the text, is attributed to the radial intraparticle inhomogeneity.	38
4.3	The dependence of the SESANS correlation function $G(z)$ on the colloidal volume fraction ϕ : (a) For the hard spherical particles with uniform density profile, upon increasing ϕ from 0.1 to 0.3, the minimum of $G_{HS}(z)$ is seen to shift from 1.8 to 1.4. (b) For the impermeable hollow spherical system, the locations of the minima for the $G_{SS}(z)$ corresponding to different ϕ , however, in principle remain at a constant value of $z_{\min}/R \sim 2$. As indicated by the insets, this invariance is mainly due to the difference in the evolution of $G_{struct}(z)$, and z_{\min} is strongly related to the peak position of $G_{struct}(z)$. However, in hollow spheres, $G_{struct}(z)$ is greatly suppressed, so its influence on the minimum position is diminished.	41

4.8	The calculated $G_{HS}(z)$ and $G_{SC}(z)$, and their constituent components given in Eq. (4.2), with colloidal number density $n = 0.0241 \text{ nm}^{-3}$. It is clear that the oscillation of $G_{HS}(z)$ is reminiscent of $G_{HS_struct}(z)$, which reflects the exclusive volume effect of the hard sphere system. The inset give an enlarged view of the $G_{HS}(z)$ and $G_{SC}(z)$	48
5.1	(a) The scattering length density profile for a homogeneous hard sphere particle. The scattering contrast is set to three different levels (orange, blue and black) by changing the H/D ratio of the surrounding solvent. (b) The calculated SANS $I(Q)$ at different levels of scattering contrast. The dash lines are the spectra for dilute solutions and the solid lines represent those for concentrated cases with a colloidal volume fraction of 0.2. (c) The corresponding SESANS correlation functions $G(z)$ are seen to be identical even though the absolute value of $\Delta\rho(r)$ changes significantly.	54
5.2	The scattering length density profile for a concentric sphere particle with (a) deuterated core and protonated shell and (b) protonated core and deuterated shell. The scattering contrast is set to three different levels (dotted, dashed, and solid lines) by changing the H/D ratio of the surrounding solvent.	55
5.3	The SANS $I(Q)$ (a) and SESANS $G(z)$ (c) calculated from the model of core-shell particle with a deuterated core and the SANS $I(Q)$ (b) and SESANS $G(z)$ (d) corresponding to the particle with deuterated shell. The colloidal volume fraction ϕ and the core radius δ in this calculation are set to be 0.4 and 0.6 respectively. The dotted, dashed, and solid lines correspond to the $I(Q)$ and $G(z)$ with the three different levels of scattering length density given in Figure 5.2.	59
5.4	The SANS $I(Q)$ (a) and SESANS $G(z)$ (c) calculated from the model of core-shell particle with deuterated core and the SANS $I(Q)$ (b) and SESANS $G(z)$ (d) corresponding to the particle with deuterated shell. The colloidal volume fraction ϕ and η in this calculation are set to be 0.4 and 1 respectively. The dotted, dashed, and solid lines are corresponding to the $I(Q)$ and $G(z)$ with the three different levels of scattering length density given in Figure 5.2.	60
5.5	The schematic representation of a colloidal suspension consisting of (a) protonated particles with a volume fraction of 0.4 and deuterated solvent; (b) protonated particles with volume fraction of 0.2, deuterated particles whose scattering length density matches that of the solvent with a volume fraction of 0.2, and deuterated solvent; (c) protonated particles with volume fraction of 0.2 and deuterated solvent.	61

5.6	The SANS $I(Q)$ and SESANS $G(z)$ calculated from the models of colloidal suspensions presented in Figure 5.5.	61
5.7	The theoretical model for the density profile of a multi-layered virus. The variation of the scattering length density along the radial direction is based on the organized intra-viral structure revealed by a SANS experiment by He and coworkers using a multi-layer spherical shell model, as shown in panel (a). Panel (b) gives the icosahedral counterpart with the isovolumic constraint.	62
5.8	The SANS $I(Q)$ and SESANS $G(z)$ calculated from the viral model shown in Figure 5.7.	63
B.1	SESANS spectra for a hard sphere system with different transmission values and the corresponding statistical error levels. (a) The measured depolarization $P(z)$ spectra with different transmission values. (b) The SESANS correlation function $G(z)$ which is exactly the same for different contrasts but with different errors. For the sake of simplicity, the case of $T_R = 0.87$ is only presented. (c) The statistical error level rises with the increase of sample transmission. Different symbols and line types are used for the corresponding transmission values, as shown in the legend.	72
C.1	Numerically and analytically calculated $G(z)$ of a binary mixture system. The symbols of square (autocorrelation function), circle (the correlation function of excluded volume) and triangle (structure correlation function) represent the numerical solutions, while the solid lines are the analytically calculated results. For the sake of clarity, the ratio of number density n_2/n_1 is set to be 1 and the size ratio $R_2/R_1 = 0.9$. ϕ_1 is kept at fixed value of 0.2. For the contribution from the interaction between particles, 1 – 1 denotes the interaction among the large particles, 2 – 2 the interaction within the small ones, and 1 – 2 the interaction between the large and small ones with the effective volume fraction $\phi_{12} = \sqrt{\phi_1\phi_2}$. This agreement promises the prospect of numerically calculating the $G(z)$ corresponding to the mathematically intractable complex systems such as concentrated colloidal suspensions consisting of particle with non-uniform density profile and irregular shape.	79
D.1	Schematic representation of two spherical core particles with radius R_1 and scattering length density ρ_1 , surrounded by an outer concentric shell of another material characterized by R_2 and ρ_2 . The particle-particle distance used in our calculation of the corresponding Debye correlation function is given by a	82

D.2	(a) Two dimensional projection of the spatial correlation of two overlapping spheres. The geometric relations among the spatial variables of x, y, z, a, r_1 and r_2 required for the evaluation of $\gamma(r)$ of the spherical systems in this study. (b) The enlarged view of the red circled area in panel (a). θ is used to define the angle between \mathbf{r}_1 and \mathbf{r}_2	83
D.3	Visualization of self correlation a sphere: $\gamma_{auto}(r)$ is determined by the overlapping volume between the referential sphere (the left one) and its virtual one (the right one) separate by \mathbf{r}	84
D.4	Schematic representation regarding the determination of cross correlation in this study: $\gamma_{cross}(r)$ is calculated by the intersection volume of a second sphere (circle of solid lines on the left) with the virtual one (circle of dashed lines on the left) corresponding to the first referential sphere [16, 48] (circle of solid lines on the right).	85
F.1	The inter-precipitate structure factors $S(Q)$ calculated from a HS model with PY closure [12] and a phenomenological one [40]. A reasonably good agreement for the $S(Q)$ in the Q range around the first interaction peak is generally found, which gives rise to the nearly identical $I(Q)$ (inset) with the same $P(Q)$	92
F.2	The corresponding $G(z)$ for the two structural models presented in Figure F.1. A distinct difference between two correlation functions is clearly seen.	93
G.1	The total structure factors for an asymmetric colloidal mixture with parameters specified in the figures, along with the reference HS system. In comparison to the $S(Q)$ obtained from the model proposed by Roth and Kinoshita [30], the $S(Q)$ calculated from the OZ/PY approach [31, 32, 33] is seen to underestimate the low- Q enhancement. Moreover, an artificial sudden decrease in the low- Q region of the $S(Q)$ from the solution of OZ/PY approach is clearly observed in the inset.	95
G.2	Consistent with the results presented in Figure G.1, the PY closure is seen to underestimate the short-range correlation due to the underestimation of the short-range attraction.	96

ACKNOWLEDGMENT

Without Prof. Li (Emily) Liu, I could not come to the United States and finish my study for Ph.D. in Rensselaer Polytechnic Institute (RPI). Without Dr. Kenneth W. Herwig, it is impossible for me to come to Oak Ridge National Laboratory (ORNL) to join this project and experience the top level research in the world. Their scientific support and friendly personality made me believe the existence of perfect supervisor. In spite of their busy schedule, they have been very patient and thoughtful in their effort to inculcate me with a sense of scientific discovery. It is my fortune to work with them during these years and transfer from a student to a real researcher. It is also an honor for me to thank Prof. Shekhar Garde, Prof. Amir H. Hirsa, Prof. Michael K. Jensen, and Prof. Chwen-Yang Shew for participating in my thesis committee and giving their advices.

Special thanks go to Dr. Wei-Ren Chen at ORNL and Dr. Yun Liu at National Institute of Standards and Technology for teaching me the liquid theory and scattering technology. Many thanks are also given to Dr. Gregory S. Smith at ORNL, Prof. Roger Pynn at Indiana University, and Prof. Chwen-Yang Shew at City University of New York for providing me with the inspirations and directions. Without all the help and advice from them, none of the progress could be achieved.

Moreover, I owe my deepest gratitude to my fiancee Ms. Tingting Zhao. Without her continuous support, any of the achievement in my research or life could not be possible.

It is a pleasure to thank my friends who shared with me the depression and happiness during the four years: Ademola Akinlalu, Xiangyu Wang, Bin Wu, Juying Zhang, Binquan Zhang, Jianwei Gu, Matthew Mille, Yong-Hum Na, and Renge Li at RPI, Kunlun Hong, Abhijit Pramanick, Dazhi Liu, Yang Zhang, Xiangqiang Chu at ORNL, Wei-Shan Chiang at Massachusetts Institute of Technology, Xin Li at Johns Hopkins University, Hongqing Sun and Xin Li at Ohio State University.

Finally, this thesis is dedicated to all my family members: my most beloved father and mother, grandmother, aunts, uncles, and cousins.

ABSTRACT

The recently devenloped spin-echo small-angle neutron scattering (SESANS) is an elastic scattering technique to provide structures with the SESANS correlation function in real space. It probes the length scale from tens of nm to several microns. Because of the specific projection method implemented in SESANS instrument, it has the great advantage to overcome the limitations of multiple scattering and the incoherent background. The framework to apply SESANS for the concentrated spherical hard colloid system with different interaction potentials is developed, and a general discussion of the features in SESANS correlation functions for different model systems is presented. The prospect to apply SESANS for colloidal particles with nonuniform intraparticle mass distribution is then explored. As examples, the core-shell structure and the soft colloid with a Gaussian model are investigated in the concentrated case. Contrast variation, as a commonly used method in conventional small angle neutron scattering (SANS), is also combined with SESANS and it is demonstrated that contrast variation SESANS is sensitive in detecting both intra- and inter-colloidal heterogeneity.

CHAPTER 1

Introduction

1.1 Layout of the Thesis

Chapter 1 provides a brief introduction of SESANS technique, including a calculation to demonstrate the decoupling of length and time scales in SESANS and interpretation of the concept of spin-echo length.

Chapter 2 introduces the correlation functions in SESANS and compares them to small angle neutron scattering (SANS). The advantages of SESANS to overcome multiple scattering and incoherent background is explained along with the derivations in detail.

Chapter 3 presents the study of SESANS for the concentrated spherical hard colloid solution, and the SESANS spectra for different interaction potentials are discussed there.

Chapter 4 derives the SESANS spectrum for spherical hard core-shell and soft colloid systems. The effect of radial inhomogeneity and a soft potential can be reflected in SESANS spectra.

Chapter 5 discusses the application of the contrast variation technique in SESANS, with both its limitations and special merits. The sensitivity of SESANS to the geometric shape of the colloid is also demonstrated there.

In Appendix A to G, the derivation of several basic functions in SESANS are provided, and some fundamental topics about the structure correlation functions are discussed.

1.2 Introduction of SESANS

Elastic neutron scattering techniques, including small angle neutron scattering (SANS) and neutron reflectivity, have proven to be some of the most informative experimental means in probing materials with nanoscale structure [1, 2]. Traditionally, the scattered/reflected intensity renders the structural information in reciprocal space and the maximum length scale is determined by the minimum accessible mo-

mentum transfer Q . With this approach, structural investigation of materials with characteristic length scales larger than a few thousand angstroms requires tight collimation of the incident and reflected neutron beams and a narrow wavelength spread to access the very small momentum transfer. Inevitably, these optical conditions lead to a significant loss of intensity. Consequently, the noninvasive structural characterization at the mesoscopic length scale, especially for soft matter study, remains the territory of light scattering and optical microscopy [3].

The recently developed spin-echo small-angle neutron scattering (SESANS) technique presents an alternative to SANS for probing soft matter structure. As first proposed by Pynn and Mezei [4] this technique uses the Larmor precession principle which has been previously employed by neutron spin echo (NSE) spectrometers for registering dynamical information via encoding of neutron wavelength. The use of tilted precession magnets enables the SESANS spectrometer to encode the scattering angle of the neutron into a change of neutron polarization, providing structural information rather than the dynamic behavior accessed by traditional NSE methods [5]. Actually, the net spin precession is composed of both structural and dynamic contributions,

$$\Delta\phi_{SP} = \frac{\Delta v}{v^2} \omega L + \frac{\alpha \cot \theta}{v} \omega L, \quad (1.1)$$

where $\Delta\phi_{SP}$ is the net spin precession, v the speed of incident neutron and Δv the speed change, α the scattering angle, θ the tilt angle of the magnetic field, ω the Larmor frequency, and L the distance over which the neutron traverses the magnetic field. The first term contains information about dynamics while the second gives structural data. From Eq. (1.1), the ratio β_{DS} , which is defined as the dynamic contribution to $\Delta\phi_{SP}$ with respect to the structural one, can be expressed as

$$\beta_{DS} = \frac{\Delta v/v}{\alpha \cot \theta} = \frac{\Delta E/E}{2\alpha \cot \theta}, \quad (1.2)$$

where E is the initial kinetic energy of the neutron and ΔE the energy transfer due to inelastic neutron scattering. The magnitude of β_{DS} can be estimated considering the general experimental situation where a beam of thermal neutrons scatters from a

condensed matter system. Assuming the beam of neutrons is incident with a typical energy of 2 *meV* (corresponding to wavelength of 6 Å), and given a ΔE of μeV for a general quasi-elastic scattering event, $\Delta E/E$ is found to be $\sim 10^{-3}$. Given a typical $\theta = 20^\circ$, based on the design of the SESANS spectrometer at the Los Alamos Neutron Science Center (LANSCE), and $\alpha \sim 1^\circ$ ($\frac{\pi}{180}$) which represents the lower limit of scattering angle, the magnitude of $2\alpha \cot \theta$ is on the order of 10^{-1} . In other words, β_{DS} is generally less than $\sim 10^{-2}$, which means that the final measured polarization is dominated by elastic scattering contributions.

SESANS is able to achieve excellent spatial resolution by making use of the spin echo method, without excessive tightening of the collimation/monochromatization of neutron beams. As a result, SESANS probes spatial correlations over distances ranging from tens of nanometers to several microns, which covers the gap in accessible length scales between confocal optical techniques and currently available SANS and neutron reflectometry. This technique can provide new insights into the large-scale structure of soft matter which are crucial to material applications and of basic scientific interest, but which were previously difficult to explore by neutron scattering due to the difficulty of obtaining simultaneously sufficiently good spatial resolution and reasonable intensity of scattered neutrons.

As demonstrated by Van Hove [6], the neutron scattering cross section can be expressed in terms of correlation functions of relevant variables. For elastic scattering, the relevant spatial pair correlation function representing density fluctuations, namely the Debye correlation function $\gamma(r)$, in general cannot be directly measured experimentally. Instead, various transforms of $\gamma(r)$ [7] are measured depending on the practical scattering implementations. The familiar SANS coherent scattering cross section $I(Q)$, which presents the structural information in *reciprocal* space, is the Fourier transform of $\gamma(r)$ [2]. The physical process of spin-echo encoding in SESANS, on the other hand, measures the *real-space* spatial correlation function $G(z)$ which can be formulated mathematically as the Abel transform [8] of $\gamma(r)$. Here z , known as spin-echo length, is calculated as follow

$$z = \frac{c\lambda^2 BL \cot \theta}{2\pi}, \quad (1.3)$$

where $c = 4.63 \times 10^{14} T^{-1}m^{-2}$ is a constant determined by the magnetic moment of the neutrons, and B the magnetic field strength. z is the length scale variable in SESANS and is related to the neutron wavelength and various properties of the magnetic fields applied to the neutron beam as part of the SESANS method [5, 9]. Structural information can be retrieved from the spectrum $G(z)$. The characteristics of $G(z)$ in different colloidal systems will be discussed in the following chapters.

CHAPTER 2

Concepts and Theories

SESANS, as a real space scattering technique, describes the structure of scattering media with the real space correlation function $G(z)$, while conventional scattering techniques such as SANS and SAXS measure in reciprocal space the macroscopic cross section $I(Q)$ which gives the angular distribution of the scattering possibility. This chapter provides the connections between these two spaces for a colloidal system.

2.1 Contrast, Distribution and Correlation

In neutron scattering experiments, a beam including both coherent and incoherent contributions illuminate a sample of volume V , and the sample is described by scattering length density distribution $\rho(\mathbf{r})$. The mean scattering length density $\langle \rho \rangle$ can be expressed as

$$\langle \rho \rangle \equiv \frac{1}{V} \int_V \rho(\mathbf{r}) d^3\mathbf{r}, \quad (2.1)$$

where the bracket means a spatial average and the scattering length density contrast is defined as

$$\Delta\rho(\mathbf{r}) = \rho(\mathbf{r}) - \langle \rho \rangle. \quad (2.2)$$

The total scattering takes place on the scattering length density and the coherent part corresponds to the contrast, presented as follows.

In most cases, a common approximation can be made that the interaction with a scatterer at point \mathbf{r} is independent of the scattering by other scatterers (which is called Born Approximation in neutron and X-ray scattering and Rayleigh Approximation for light). Within this single-scattering framework, the scattering amplitude can be simply added up as

$$F(\mathbf{Q}) = \int_V \rho(\mathbf{r}) \exp(-i\mathbf{Q} \cdot \mathbf{r}) d^3\mathbf{r}, \quad (2.3)$$

where $\mathbf{Q} = \mathbf{k}_f - \mathbf{k}_i$ (\mathbf{k}_i and \mathbf{k}_f the wave vectors of the incident and scattered beam) is the scattering vector and its amplitude is related to the scattering angle θ by $Q = \frac{4\pi}{\lambda} \sin(\frac{\theta}{2})$ for wavelength λ .

Then the scattered intensity per unit volume can be expressed as

$$I(\mathbf{Q}) = \frac{F(\mathbf{Q})F^*(\mathbf{Q})}{V} = \frac{|F(\mathbf{Q})|^2}{V}, \quad (2.4)$$

which can be extended with the scattering length density distribution $\rho(\mathbf{r})$

$$I(\mathbf{Q}) = \frac{1}{V} \int_V \int_V \rho(\mathbf{r})\rho(\mathbf{r}') \exp[-i\mathbf{Q} \cdot (\mathbf{r} - \mathbf{r}')] d^3\mathbf{r} d^3\mathbf{r}'. \quad (2.5)$$

$F^*(\mathbf{Q})$ is the conjugate of $F(\mathbf{Q})$. The two-point correlation function introduced by Debye and Bueche $\gamma(\mathbf{r})$ can be defined as

$$\gamma(\mathbf{r}) = \frac{1}{V} \int_V \rho(\mathbf{r}' + \mathbf{r})\rho(\mathbf{r}') d^3\mathbf{r}', \quad (2.6)$$

and therefore, Eq. (2.5) becomes

$$I(\mathbf{Q}) = \int_V \gamma(\mathbf{r}) \exp(-i\mathbf{Q} \cdot \mathbf{r}) d^3\mathbf{r}. \quad (2.7)$$

Substituting Eq. (2.2) into Eq. (2.6), one easily gets

$$\begin{aligned} \gamma(\mathbf{r}) &= \frac{1}{V} \int_V \Delta\rho(\mathbf{r}' + \mathbf{r})\Delta\rho(\mathbf{r}') d^3\mathbf{r}' + <\rho>^2 \\ &= \gamma_0(\mathbf{r}) + <\rho>^2, \end{aligned} \quad (2.8)$$

where $\gamma_0(\mathbf{r})$ from the contrast is the usually named the Debye correlation function. Then the scattering amplitude and intensity become

$$F(\mathbf{Q}) = \int_V \Delta\rho(\mathbf{r}) \exp(-i\mathbf{Q} \cdot \mathbf{r}) d^3\mathbf{r} + <\rho> \delta(\mathbf{Q}), \quad (2.9)$$

and

$$\begin{aligned} I(\mathbf{Q}) &= \frac{1}{V} \int_V \int_V \Delta\rho(\mathbf{r})\Delta\rho(\mathbf{r}') \exp[-i\mathbf{Q}\cdot(\mathbf{r}-\mathbf{r}')] d^3\mathbf{r}d^3\mathbf{r}' + <\rho>^2 \delta(\mathbf{Q}) \\ &= \int_V \gamma_0(\mathbf{r}) \exp(-i\mathbf{Q}\cdot\mathbf{r}) d^3\mathbf{r} + <\rho>^2 \delta(\mathbf{Q}). \end{aligned} \quad (2.10)$$

The first terms in Eqs. (2.9) and (2.10) are the usually mentioned scattering amplitude and scattering intensity because the contribution from the $\delta(\mathbf{Q})$ function is negligible in the regular finite Q range measured with conventional small angle scattering instruments.

2.2 SESANS Correlation Function

In SESANS, the measurement of the depolarization of the scattered neutron beam at a certain spin-echo length z , which is called SESANS correlation function $G(z)$, gives the integration over the Q range in \hat{z} direction as follow

$$G(z) = \int \frac{d\Sigma}{d\Omega}(\mathbf{Q}) \cos(zQ_z) d^3\mathbf{Q}. \quad (2.11)$$

It performs a Fourier transform in \hat{z} direction and the macroscopic cross section is the intensity $I(\mathbf{Q})$ measured in conventional SANS. In the case of isotropic colloidal system, $y = 0$ can be substituted into $\mathbf{r}(x, y, z)$ with only scattering over z considered; in small angle scattering condition, $Q_x = 0$ can be assumed and put into the integration. With substituting Eq. (2.10) into Eq. (2.11), one finds

$$G(z) = \int_{-\infty}^{+\infty} \gamma(\mathbf{r}) dx = 2 \int_z^{+\infty} \frac{\gamma(r)r}{\sqrt{r^2 - z^2}} dr, \quad (2.12)$$

where $\gamma(r)$ is proportional to the square of scattering length density, $<\rho^2(\mathbf{r})>$, and with the SESANS projection length ξ defined as

$$\xi = 2 \int_0^{+\infty} \gamma(r) dr, \quad (2.13)$$

therefore the normalized $G(z)$

$$G(z) = \frac{2}{\xi} \int_z^{+\infty} \frac{\gamma(r)r}{\sqrt{r^2 - z^2}} dr, \quad (2.14)$$

is the SESANS correlation function which is generally referred to and gives $G(0) = 1$. As expressed in Eq. (2.8) the constant $\langle \rho \rangle^2$ in $\gamma(r)$ will give a $\delta(Q)$ function in reciprocal space and a constant value in real space which will be eliminated in the normalization, so the contribution to $G(z)$ mainly comes from the coherent scattering of the density contrast. Mathematically, Eqs. (2.12) and (2.14) are named Abel transform. The physical meaning of Abel transform and its relation with Fourier transform are thoroughly discussed in Appendix A.

2.2.1 Multiple Scattering

The ability of SESANS to overcome the multiple scattering in the sample is a remarkable advantage over conventional scattering techniques, which is caused by the specific projection operated in SESANS measurement.

The final measured polarization is attributed to two parts: the directly transmitted neutrons and the remaining polarization from the scattered ones, so

$$P(z) = T_R + G'(z, t), \quad (2.15)$$

and

$$T_R = \exp(-\Sigma t), \quad (2.16)$$

where $P(z)$ is the measured polarization, T_R the sample transmission, t the sample thickness, Σ the total macroscopic cross section and $G'(z, t)$ the fraction of beam modified in polarization by the change of scattering angle with multiple scattering taken into consideration. For a single scattering event in small angle scattering condition,

$$\mathbf{Q} = Q_y \hat{y} + Q_z \hat{z}, \quad (2.17)$$

$$\Sigma = \frac{1}{k_0^2} \int \frac{d\Sigma}{d\Omega}(\mathbf{Q}) dQ_y dQ_z, \quad (2.18)$$

and

$$G(z) = \frac{1}{\Sigma k_0^2} \int \frac{d\Sigma}{d\Omega}(\mathbf{Q}) \cos(zQ_z) dQ_y dQ_z, \quad (2.19)$$

where k_0 is the momentum of the incident beam. An n -time multiple scattering can be treated as a series of n single scattering events and any of them follows the law of a single scattering event within the sample range t . Therefore, let us consider the possibility of an n -time scattering event,

$$\begin{aligned} \rho_n &= \frac{T_R \times t^n}{k_0^{2n} 1 \times 2 \times \cdots \times n} \int \frac{d\Sigma}{d\Omega}(\mathbf{Q}_1) dQ_{1y} dQ_{1z} \\ &\times \int \frac{d\Sigma}{d\Omega}(\mathbf{Q}_2) dQ_{2y} dQ_{2z} \times \cdots \times \int \frac{d\Sigma}{d\Omega}(\mathbf{Q}_n) dQ_{ny} dQ_{nz} \\ &= \frac{(\Sigma t)^n}{n!} T_R, \end{aligned} \quad (2.20)$$

and the momentum transfer which is also mentioned above as the scattering vector \mathbf{Q} can be extended as

$$\mathbf{Q} = \mathbf{Q}_1 + \mathbf{Q}_2 + \cdots + \mathbf{Q}_n, \quad (2.21)$$

and its contribution in the correlation function

$$\cos(Q_z) = \cos(Q_{1z}) \cos(Q_{2z}) \cdots \cos(Q_{nz}) + \text{odd terms}, \quad (2.22)$$

where the odd terms will not contribute to the integration in Eq. (2.11). Therefore, the contribution of an n -time scattering event to the SESANS correlation function is

$$\begin{aligned} G_n(z) &= \frac{T_R \times t^n}{k_0^{2n} 1 \times 2 \times \cdots \times n} \int \frac{d\Sigma}{d\Omega}(\mathbf{Q}_1) \cos(zQ_{1z}) dQ_{1y} dQ_{1z} \\ &\times \int \frac{d\Sigma}{d\Omega}(\mathbf{Q}_2) \cos(zQ_{2z}) dQ_{2y} dQ_{2z} \times \cdots \times \int \frac{d\Sigma}{d\Omega}(\mathbf{Q}_n) \cos(zQ_{nz}) dQ_{ny} dQ_{nz} \\ &= \frac{(\Sigma t G(z))^n}{n!} T_R, \end{aligned} \quad (2.23)$$

and the total correlation for multiple scattering events is

$$G'(z, t) = \sum_n G_n(z) = \sum_{n=1}^{\infty} \frac{(\Sigma t G(z))^n}{n!} T_R = T_R [\exp(\Sigma t G(z)) - 1]. \quad (2.24)$$

Substituting Eq. (2.16) into Eq. (2.24), one can have

$$P(z) = \exp[\Sigma t(G(z) - 1)] = T_R^{1-G(z)}, \quad (2.25)$$

and

$$G(z) = 1 - \frac{\ln[P(z)]}{\ln(T_R)}, \quad (2.26)$$

as the measured polarization and SESANS correlation function which have the limits and normalization conditions as

$$\begin{aligned} P(\infty) &= T_R = \exp(-\Sigma t) \\ G(\infty) &= 0 \\ P(0) &= 1 \\ G(0) &= 1. \end{aligned} \quad (2.27)$$

2.2.2 Coherent and Incoherent Scattering

In neutron scattering, the scattering length b and scattering length density ρ depend on both the species of nuclei and the spin states. For the sake of convenience, the scattering cross section is generally separated into a coherent and incoherent part. Assuming the isotopic and spin states of each nucleus are uncorrelated with its position, one obtains

$$\frac{d\Sigma}{d\Omega}(\mathbf{Q}) = \frac{d\Sigma}{d\Omega_{coh}}(\mathbf{Q}) + \frac{d\Sigma}{d\Omega_{inc}}, \quad (2.28)$$

where

$$\frac{d\Sigma}{d\Omega_{coh}}(\mathbf{Q}) = \frac{1}{V} \left| \sum_{l=1}^N b_l^{coh} \exp(i\mathbf{Q} \cdot \mathbf{r}) \right|^2, \quad (2.29)$$

in the sample volume V containing N particles and

$$\frac{d\Sigma}{d\Omega_{inc}} = \frac{1}{V} \sum_{l=1}^N (b_l^{inc})^2 = N_H \frac{\sigma_{inc}^H}{4\pi}, \quad (2.30)$$

when hydrogen dominates the incoherent scattering and σ_{inc}^H is the microscopic incoherent scattering cross section of hydrogen. The incoherent scattering is uniformly distributed over the whole 4π solid angle. b_l^{inc} and b_l^{coh} are the incoherent and coherent scattering lengths, calculated as

$$\begin{aligned} b_l^{inc} &= \sqrt{\langle b_l^2 \rangle - \langle b_l \rangle^2} \\ b_l^{coh} &= \langle b_l \rangle, \end{aligned} \quad (2.31)$$

where the bracket symbol means the average taken over the spin and isotopic states for each species within the specific particle l .

The coherent contributions in Eqs. (2.28) and (2.29) are also described with continuum correlations defined in Eqs. (2.5) and (2.7). In SESANS, as presented in Eq. (2.11), the scattering possibility $\frac{d\Sigma}{d\Omega}(\mathbf{Q})$ contains both coherent and incoherent contributions. But the incoherent scattering, as a constant value independent of \mathbf{Q} , gives a $\delta(z)$ function which could be omitted in SESANS measured range. In principle, the measured SESANS spectrum $G(z)$ only records the coherent scattering information, while SANS $I(Q)$ collects both coherent and incoherent scattering and the strong incoherent background may inundate the signal with the variation of contrast. The only difference attributed to strong incoherent scattering is reflected in the data statistics due to the variation of scattering power. Further discussion regarding incoherent scattering in SESANS is presented in Chapter 5 and Appendix B.

CHAPTER 3

Interaction in Concentrated Spherical Colloid System

This new SESANS technique has been applied to several structural investigations of soft matter systems [10]. The technique focuses on relating the experimentally measured $G(z)$ to the corresponding structural properties of non-interacting dilute colloidal solutions consisting of particles with different simple geometry [10]. On the other hand, for the research in colloidal science, considerable effort has been devoted to understanding the manner in which interactions between individual colloids in real solutions affect various thermodynamical properties [11]. Considering the fact that numerous applications of colloids require concentrated solutions, understanding the interaction effect and phase behavior of this class of solutions is of significant scientific and technological importance. From a theoretical perspective, the basis for the understanding the equilibrium properties of soft matter in general and colloidal suspensions in particular is the pair distribution function $g(r)$, which gives the probability of finding a particle at the distance r from a reference [12]. Calculating specific form of $g(r)$ begins by hypothesizing the interaction between the constituent particles. However, in general, to avoid the complicated problem of treating the constituent components of the whole colloidal systems individually, the statistical mechanical description of general colloidal systems is simplified by means of the one-component model (OCM), in which the colloids are considered as gas of solute particles immersed in a continuous background. The effective interaction potential $V(r)$ is derived by integrating out the degrees of freedom of small solvent molecules onto the dimension of the colloidal particles in a coarse-grained manner. The colloidal phenomena is described by the $g(r)$ calculated from the Ornstein-Zernike (OZ) equation together with an additional closure equation whose validity depends on the different mathematical expression of $V(r)$.

¹This chapter previously appeared as: Xin Li, Chwen-Yang Shew, Yun Liu, Roger Pynn, Emily Liu, Kenneth W. Herwig, Gregory S. Smith, J. Lee Robertson, and Wei-Ren Chen, “Theoretical studies on the structure of interacting colloidal suspensions by spin-echo small angle neutron scattering”, *J. Chem. Phys.*, Vol. 132, 174509, 2010, pp. 1-14.

Most of the contemporary knowledge regarding the structural properties of colloidal suspensions is the result of scattering experiments. For example, light scattering has been used to render the structural information of colloidal suspensions [13, 14, 2]. It is not a surprise that the idea concerning identification of inter-colloidal interaction via SESANS measurement has been explored on an operational length scale comparable to that of static light scattering [15]. A recent effort of Krouglov and coworkers [16], concerning sterically stabilized silica spheres suspended in deuterated cyclohexane in which the excluded volume repulsion is the central feature of the colloidal interaction, was a first proof-of-principle demonstration. Within the concentration range where the colloidal interaction can be well approximated by a pairwise addition of an excluded hard sphere repulsion, the measured $G(z)$ is seen to be in a satisfactory quantitative agreement with the result of model calculations based on an integral equation approach proposed earlier by Glatter [17]. In the course of exploiting the scientific merits of SESANS for colloidal structural characterization, it becomes clear that it is essential to evaluate the extent to which the SESANS spectral measurements reflect more complex, underlying inter-colloidal interaction features in a quantitative manner. Our treatment focuses on simple systems, primarily those involving monodisperse spherical colloids with well-defined inter-colloidal interactions. Calculations of $G(z)$ are provided for the models corresponding to steric repulsion, depletion and van der Waals attractions, screened Coulomb repulsion, and two Yukawa potentials, within the concentration range where the validity of the various statistical mechanical models for determining structural properties have been rigorously tested against the corresponding computational simulations. In this chapter, a broad understanding, through identifying $G(z)$ calculated from our mean-field models, regarding the unique advantage of SESANS for structural characterization of concentrated colloidal suspensions is sought to be established.

3.1 Decomposition of SESANS Correlation Function

It is instructive to calculate the Debye correlation function $\gamma(r)$ prior to computing $G(z)$. In the case of isotropic interaction, it is known that the $\gamma(r)$ for

an assembly of diffusive monodisperse spheres can be expressed as the collective contribution [2, 18].

$$\gamma(r) = \gamma_{auto}(r) - n \int_0^{2R} \gamma_{ovl}(r, a) 4\pi a^2 da + n \int_{2R}^{\infty} \gamma_{cross}(r, a) [g(a) - 1] 4\pi a^2 da, \quad (3.1)$$

where a is the distance between two particles, n the colloidal number density, R the sphere radius and $g(r)$ the pair correlation function (note that r is replaced by the dummy variable a in Eq. (3.1)). In Eq. (3.1), the first term on the RHS originates from the self-correlation within a single particle, and the two-particle correlation function can be further divided into two parts, including the contribution due to the exclusive shadowing effect (the second term) and inter-particle correlation (the third term). Both $\gamma_{ovl}(r, a)$ and $\gamma_{cross}(r, a)$ are non-negligible as interactions become important. It is important to point out that $\gamma_{cross}(r, a)$ is a function of both the concentration and the mathematical expression of the inter-colloidal potential, while $\gamma_{ovl}(r, a)$ only depends on the former. The analytical expressions of $\gamma_{auto}(r)$, $\gamma_{ovl}(r, a)$ and $\gamma_{cross}(r, a)$ for spherical objects have been previously derived and $\gamma(r)$ can therefore be analytically calculated if the pair distribution function $g(r)$ is known. Alternatively $\gamma(r)$ can be calculated numerically with the same quantitative accuracy. The results and a further discussion of this "dumbbell model" are presented in Appendix C.

Via Eq. (2.14), the Abel component of Eq. (3.1) is found to be

$$G(z) = G_{auto}(z) - \phi G_{excl}(z) + \phi G_{struct}(z), \quad (3.2)$$

where ϕ is the colloidal volume fraction. As an example, the $G(z)$ corresponding to a hard sphere colloidal suspension with volume fraction of 0.2 and radius of 130 nm is presented in Figure 3.1. $G(z)$ is decomposed into a linear combination of three different functions attributable to the corresponding spatial correlations. The following work addresses the expressions for the SESANS correlation functions $G(z)$ of various interacting colloidal suspensions with finite concentrations, which can be applied in the analysis of experimental data. Here the focus is placed on

understanding the dependence of $G(z)$ on the specific form of the inter-colloidal interaction potential.

Before moving further to the discussion of the effect from different potential, it is important to point out the fundamental difference between the conventional SANS and the novel SESANS. Considering this coarse-grained one-component model (OCM) [2], the whole system can be compartmentalized into N constituent components each corresponding to a single colloidal particle. From Eq. (2.8) one finds that the corresponding Debye correlation function $\gamma_N(\mathbf{r})$ becomes

$$\begin{aligned}\gamma_N(\mathbf{r}) &= \int_V \sum_{i=1}^N \Delta\rho(\mathbf{r}' - \mathbf{r}_i) \sum_{j=1}^N \Delta\rho(\mathbf{r}' - \mathbf{r}_j - \mathbf{r}) d^3\mathbf{r}' \\ &= \sum_{i=1}^N \int_V \Delta\rho(\mathbf{r}' - \mathbf{r}_i) \Delta\rho(\mathbf{r}' - \mathbf{r}_i - \mathbf{r}) d^3\mathbf{r}' \\ &+ \sum_{\substack{i,j=1 \\ i \neq j}}^N \int_V \Delta\rho(\mathbf{r}' - \mathbf{r}_i) \Delta\rho(\mathbf{r}' - \mathbf{r}_j - \mathbf{r}) d^3\mathbf{r}'.\end{aligned}\quad (3.3)$$

The definite integral presented in the first term on the right-hand side (RHS) of Eq. (3.3) is the definition of the self autocorrelation function of a single particle $\gamma_{auto}(\mathbf{r})$, namely

$$\gamma_{auto}(\mathbf{r}) = \int_V \Delta\rho(\mathbf{r}') \Delta\rho(\mathbf{r}' - \mathbf{r}) d^3\mathbf{r}'.\quad (3.4)$$

The second term on the RHS of Eq. (3.3) is a convolution which contains the structural information of the intracolloidal self correlation and the intercolloidal spatial distribution. Because

$$\sum_{\substack{i,j=1 \\ i \neq j}}^N \delta(\mathbf{r} - \mathbf{r}_i + \mathbf{r}_j) = Nn[g(\mathbf{r}) - 1],\quad (3.5)$$

where $n \equiv \frac{N}{V}$ is the colloidal number density of the system and $g(r)$ the pair correlation function, $\gamma_N(\mathbf{r})$ is found to take the following form:

$$\gamma_N(\mathbf{r}) = N \int_V \gamma_{auto}(\mathbf{r} - \mathbf{a}) \{\delta(\mathbf{a}) + n[g(\mathbf{a}) - 1]\} d^3\mathbf{a}.\quad (3.6)$$

The factor N is due to the fact that all N colloidal particles are set to be identical in this study. \mathbf{a} is the variable of integration. It is clearly seen that Eq. (3.6) can be further expressed as

$$\gamma_N(\mathbf{r}) = N \{ \gamma_{auto}(\mathbf{r}) \otimes \delta(\mathbf{r}) + n \cdot \gamma_{auto}(\mathbf{r}) \otimes [g(\mathbf{r}) - 1] \}. \quad (3.7)$$

It is convenient to normalize $\gamma_N(\mathbf{r})$ by the probed sample volume. The mathematical relation between the normalized correlation $\gamma(r)$ and $\gamma_N(\mathbf{r})$ is found to be

$$\gamma(r) = \left\langle \frac{\gamma_N(\mathbf{r})}{V} \right\rangle. \quad (3.8)$$

Substituting Eqs. (3.7) and (3.8) into Eq. (2.10), based on the convolution theorem of the Fourier transform [8], one finds that $I(Q)$ can be expressed as

$$\begin{aligned} I(Q) &= \frac{N}{V} [P(Q) + P(Q)(S(Q) - 1)] \\ &= nP(Q)S(Q), \end{aligned} \quad (3.9)$$

which is the familiar expression for the coherent scattering cross section of small angle neutron scattering. The form factor, $P(Q)$, is the Fourier transform of the self correlation part of Eq. (3.7) and therefore gives information about the (intra-colloidal) density profile within a single colloidal particle. On the other hand, the structure factor, $S(Q)$, which is the Fourier transform of the intercolloidal term $g(\mathbf{r})$, contains information about the relative arrangement of colloidal particles. On the basis of the aforementioned mean-field approximation, the majority of SANS studies of colloids have placed the focus on extracting intra- and intercolloidal structural characteristics using various models of intercolloidal effective interaction potentials $V(r)$. It is worth emphasizing that, as evidenced by the above derivations, this convenient factorization approximation is strictly valid only for monodisperse spherical systems. Additional modifications of Eq. (3.9) are certainly required for modeling the coherent scattering intensity obtained from colloidal systems with non-spherical

shapes and/or with polydispersity in size to incorporate the effects of additional angular correlation and size asymmetry [19, 20, 21].

3.1.1 Calculation of the Pair Distribution Function $g(\mathbf{r})$

For a given microstructure of a homogeneous colloidal suspension, a viable theory for calculating its $g(r)$ with a given effective potential is the Ornstein-Zernike (OZ) equation [12, 2]:

$$h(\mathbf{r}_{12}) = c(\mathbf{r}_{12}) + n \int d\mathbf{r}_3 c(\mathbf{r}_{13}) h(\mathbf{r}_{32}), \quad (3.10)$$

where $h(r) = g(r) - 1$ is the total correlation function for two particles separated by the distance r , $c(r)$ the direct correlation function, and n the number density. $h(r)$ consists of two parts: The direct correlations between particles 1 and 2 measured by $c(\mathbf{r}_{12})$, and the indirect correction function that is convolution of total correlation function and direct correlation function. Eq. (3.10) is an recursive equation, and can be expanded as $h = c + c*c + c*c*c \dots$ where $*$ denotes convolution. This expression indicates that the pair correlation function between any two particles is influenced by the remaining particles in liquid, and can be calculated by propagating the direct correlation through the surrounding particles. In general, the direct correlation function $c(r)$ is also unknown. In order to make use of OZ equation for structural calculations, a second relation between $h(r)$ and $c(r)$ is needed. The so-called closure equation can be obtained via the expansion of the free energy in the excess particle density:

$$g(r) = \exp[-\beta V(r)] \exp[h(r) - c(r) + b(r)], \quad (3.11)$$

where $V(r)$ is the interaction potential, $\beta = \frac{1}{k_B T}$, T the thermodynamic temperature of the system, and $b(r)$ is named bridge function, which is a collection of elementary diagrams related to some higher order correlations. The indices are omitted for clarity.

Hypernetted chain (HNC) closure, which is well suited for long-ranged Coulombic systems, is obtained by neglecting $b(r)$ in Eq. (3.11):

$$g(r) = \exp[-\beta V(r)] \exp[h(r) - c(r)]. \quad (3.12)$$

Expanding the factor $\exp[h(r) - c(r)]$ to linear order one finds another commonly used Percus-Yevick (PY) closure, which gives satisfactory structural description for a system interacting via an effective short-range attractive or hard sphere potential [2]:

$$g(r) = \exp[-\beta V(r)][1 + h(r) - c(r)]. \quad (3.13)$$

Further linearization of the exponential term in Eq. (3.13) gives the mean spherical approximation (MSA)

$$c(r) = \exp[-\beta V(r)]. \quad (3.14)$$

MSA is a popular closure among theoretical works due to its mathematical simplicity. Moreover, the thermodynamic inconsistency introduced by the approximation of Eq. (3.11) can be removed by using a composite closure which mixes HNC and PY closures in a manner requiring the compressibility pressure to be identical to that obtained from the virial equation of state [22].

$$g(r) = \exp[-\beta V(r)][1 + \frac{\exp\{[h(r) - c(r)]f(r)\} - 1}{f(r)}], \quad (3.15)$$

and the empirical form of the mixing function $f(r)$ is found to be

$$f(r) = 1 - \exp(-\alpha r), \quad (3.16)$$

where α is determined from the thermodynamic consistency requirement. Evidenced by the corresponding simulation studies, this celebrated Rogers-Young (RY) closure is seen to work well for general repulsive systems, regardless of the detailed potential features [23].

To minimize the influence of the numerical error introduced by the many-body interaction which is not incorporated in the statistical mechanical model, the colloidal volume fraction ϕ is set at a constant value of 0.2. Moreover, the $G(z)$

generated from the $g(r)$ based on different closures, suitable for their corresponding interaction potential models and valid in this concentration, will be presented along with that of the hard sphere system in a comparative manner.

3.1.2 Potential Models

In the physical picture of OCM, the theoretical calculation of the structural and thermodynamical properties of any given colloidal suspensions requires the appropriate description of the inter-colloidal interaction potential. Prior to the calculation of various correlation functions it is instructive to briefly describe the potential models commonly encountered in structural characterization of general colloidal suspensions.

Figure 3.2 presents the potential models used in the calculation: The simplest potential model is the hard sphere (HS) potential as in Figure 3.2(a), namely

$$V_{HS}(r) = \begin{cases} \infty & \text{for } r < R \\ 0 & \text{for } r > R \end{cases}, \quad (3.17)$$

where R is the radius of the colloid. One example of an HS colloidal systems is sterically stabilized polymethylmethacrylate (PMMA) particles dissolved in organic solvents such as dodecane or cis-decalin [13]. Moreover, with the presence of a non-adsorbing smaller particle in the HS system, an additional effective attraction, due to the osmotic pressure caused by the secondary particles, can be introduced between the colloids along with the excluded volume repulsion given in Eq. (3.17). A mathematical expression of this effective potential is

$$V_{AHS}(r) = \begin{cases} \infty & \text{for } r < R \\ -u & \text{for } R < r < R + \varepsilon \\ 0 & \text{for } r > R + \varepsilon \end{cases}, \quad (3.18)$$

where u is the attractive strength and ε the width of the attractive well. Several models have been developed to express u and ε as the function of the volume fraction of the free smaller particles in the colloidal dispersion [13]. It is approximated by an adhesive hard sphere (AHS) potential, which consists of the excluded hard core and a

attractive square well [24], in our calculation for the sake of mathematical simplicity. In spite of its simplicity, AHS model accounts for the short-ranged attractive tail between spherical objects besides their excluded volume interaction, which has been applied to explain colloidal particles and nonionic micellar solutions by Menon [25], for example. A schematic representation of this potential with $u = 2k_BT$ and $\varepsilon = 0.02R$ is given in Figure 3.2(b).

The classical Derjaguin–Landau–Verwey–Overbeek (DLVO) theory provides an analytical expression for precise description of the electrostatic forces exerted by charged spherical colloidal particles, such as charged polystyrene spheres and latex particles. It explains the stability of highly charged colloidal systems based on the assumption that the primary interactions between two particles consist of the screened Coulomb repulsion and attractive van der Waals dispersion which arises from instantaneous fluctuations in the colloidal electron distributions. At low ionic strength, the screened Coulomb repulsion dominates at all distances. As the example given in Figure 3.2(c), it is specified by the Yukawa form [26, 27]:

$$V_{SC}(r) = -K_1 \frac{\exp[-Z_1(r - 2R)]}{r} \quad (r > 2R), \quad (3.19)$$

where K_1 is the interaction strength, normalized by thermal energy k_BT and the normalized interaction range, namely the screening length, is given as Z_1^{-1} , which is the function of the ionic strength of the medium. Moreover, the dispersion force can be revealed when the long-range Coulomb repulsion is properly adjusted by tuning the ionic strength. With the presence of a suitable amount of salt in the system, the effective potential in our calculation is given by the following approximation:

$$V_{TY}(r) = -K_1 \frac{\exp[-Z_1(r - 2R)]}{r} + K_2 \frac{\exp[-Z_2(r - 2R)]}{r} \quad (r > 2R), \quad (3.20)$$

where the second Yukawa potential with opposite sign of the interaction strength is used to represent the short-range attraction, whose detailed mathematical expression is described elsewhere [11, 28]. One example of this two-Yukawa potential is displayed in Figure 3.2(d).

3.2 SESANS Spectra for Different Interaction Potentials

To provide the basis for comparison and demonstrate the difference between SESANS and conventional elastic techniques in exploring the intermolecular interaction, the normalized coherent scattering cross section of small angle, $\frac{d\Sigma}{d\Omega}(Q)$, which is also commonly denoted as the absolute intensity $I(Q)$, are calculated based on the potential model list in the previous section. To avoid irrelevant mathematical complexity, a system of monodisperse spherical colloids with a uniform intraparticle density profile is chosen for the calculations of this Chapter. With this approximation, theoretically the corresponding $I(Q)$ can be further factorized and are found to be proportional to the particle density and the product of the form factor $P(Q)$ and the structure factor $S(Q)$, where $P(Q)$ is the Fourier transform of the molecular density profile $\rho(r)$, which is corresponding to the autocorrelation of a single particle. In the case of homogeneous sphere with radius of R , $P(Q)$ takes the familiar analytic expression:

$$P(Q) = \left| \frac{3 [\sin(QR) - QR \cos(QR)]}{(QR)^3} \right|^2. \quad (3.21)$$

$S(Q)$ is the particle center-to-center spatial correlation function, which is related to $g(r)$ by the exact result for an isotropic homogeneous system:

$$S(Q) = 1 + 4\pi n \int_0^\infty r^2 [g(r) - 1] \frac{\sin(Qr)}{Qr} dr. \quad (3.22)$$

Aside from dealing with the scattering contribution from the usually unavoidable factors such as polydispersity and anisotropic interaction, the main theme of a general small angle scattering experiment, either neutron, X-ray or light, is to determine separately the $P(Q)$ and the $S(Q)$. Calculated curves for $P(Q)$, $S(Q)$ and $I(Q)$ based on potential models are presented in Figure 3.3. The scaling factor of $I(Q)$ which is a function of the colloidal number density and contrast with the surrounding solvent is set to be unity. Due to the rapid decay of $P(Q)$, it is seen that the resulting $I(Q)$ are all characterized by a single peak manifesting the first order correlation peak of $S(Q)$. For the attraction dominated potential, such as AHS in Figure 3.3(c), a rise of $I(Q)$ at small wavevector emerges, whereas for

other repulsion dominated potentials, $I(Q)$ shares the common feature consisting of the prominent correlation peak. These results suggest that repulsive and attractive molecular forces may be discernible if the instrumental resolution allows resolving scattering signals at sufficiently small angles.

From the technical standpoint, except in some special cases such as SANS studies of the isotopically labeled colloids with deuterated molecular periphery dissolved in properly matching solvent, we note that the higher order correlation peaks of $S(Q)$ are generally invisible if the resolution of instrument is taken into consideration. Due to this constraint, the precise characterization of the colloidal phase behavior by conventional elastic scattering technique often requires complementary experimental means to provide the details of the interactions [24]. In comparison to the $I(Q)$ delivered by small angle scattering experiment, the structural information concealed in $G(z)$ measured by SESANS is largely preserved due to the fact that it is reflected in the superposition of the hierarchical spatial correlations, as evidenced by Figure 3.1. Appendix F gives another example to further support this argument. As will be discussed in the following text, this unique feature of SESANS is intended to be explored for structural characterization of concentrated colloidal suspensions using the aforementioned model potentials.

The calculation of the single component hard sphere system, presented in Figure 3.1, is further extended to study the binary mixture of hard spheres with large asymmetry in particle size. In the context of using the synergistic scattering/integral equation approach to extract the microstructure and thermodynamics of colloidal suspensions, the binary colloidal system is modeled as an bidisperse mixture of large hard spheres with radius R_1 and smaller second hard spheres with radius R_2 . In the structural calculation of this system, a numerical closure developed by Roth and Kinoshita [30] is chosen over the commonly used PY one [31, 32, 33] to generate the $g(r)$ from the OZ equation. The justification of this action is given in Appendix G. The dependence of the partial SESANS correlation function of particle 1, $G_{11}(z)$, on the volume fraction of the smaller particle 2, ϕ_2 , is given in Figure 3.4. In the calculation, the volume fraction of particle 1, ϕ_1 , is fixed at a constant value of 0.2 and its radius is set as 130 nm in the calculation. The ratio of $\frac{R_2}{R_1}$ is set to be 0.2. It is

clearly seen that, with an increase in ϕ_2 from 0 to 0.27, $G_{11}(z)$ exhibits a continuous increase in magnitude within the correlation length around $1 < z/R < 3$. Note that at the strongest interaction strength $u = 3k_BT$, the $G(z)$ in this region becomes greater than zero, which may provide a convenient mean to identify the attractive intermolecular force in a colloid liquid. According to Eq. (3.2), such a trend can be attributed to the increasingly large $G_{11\text{struct}}(z)$, as indicated in the inset, originating from the entropy-driven osmotic depletion attraction between particles 1 due the presence of particles 2.

In a neutron scattering experiment, this binary colloidal mixture can be further considered as one-component solution of particle 1 by eliminating the coherent scattering contribution from particle 2 by means of deuteration or increasing size asymmetry to a sufficient level. In other words, theoretically such a colloidal system can be alternatively viewed as the colloidal suspension whose interaction potential is composed of an excluded volume repulsion and an additional short-range attraction, as shown in Figure 3.2(b). Figure 3.5 presents the calculated $G(z)$ based on the AHS model [24] with $\phi = 0.2$, radius $R = 130$ nm and the attractive width $\varepsilon = 2.6$ nm, with aims at mimicking the attractive depletion force at a qualitative level. Upon strengthening the attraction from 0, namely the interaction of pure excluded volume repulsion, to $3k_BT$, the evolving qualitative feature corresponding $G(z)$ is consistent with the progressively enhanced local structuring revealed in Figure 3.4. It is also noticed that the findings presented in Figures 3.4 and 3.5 are not in an agreement with previous calculations of Uca and coworkers [34]. Their selected structure factor was derived using a perturbative solution of the factorized form of OZ equation and PY closure relation, and it exhibited agreement with Monte Carlo simulation results [25]. However, this solution of the structure factor has a tremendous oscillation in high Q range, which was not usually noticeable in traditional experiment and analysis. But this strong oscillation in high Q range will cause an abnormality in the pair distribution function $g(r)$, which will be definitely reflected in SESANS spectrum. As represented in Figure 3.6 even though the structure factors appear similar in the range of $2QR < 25$, the immense oscillation could generate a singular point of $g(r)$, and the negative value coming from $g(r)$ divergence gives the decline

of $G(z)$.

Considered next is the dependence of $G(z)$ on the strength of electrostatic repulsion between the charged colloids. Assuming a uniform charge distribution on the colloidal surface, the premise of this calculation of OZ/RY approach is that the intercolloidal interaction is dominated by the screened Coulomb repulsion while the excluded volume repulsion and dispersion attraction play no role on colloidal structural description. Figure 3.7 gives the evolutions of $G(z)$ and $G_{struct}(z)$ as a function of the repulsive strength with a fixed screening length $Z_1^{-1} = 0.5$. It is noticed that, as the repulsive strength K_1 is progressively increased from 0 to $6k_B T$, both $G(z)$ and $G_{struct}(z)$ develop an increasingly pronounced oscillation, within the calculated range of z , corresponding to the correlation length which is experimentally accessible. This observation is attributed to the enhancement in the degree of local ordering due to the increase in electrostatic repulsion. It is important to point out that, in the previous theoretical [34] and experimental [16] studies of hard sphere colloidal systems, the evolution of $G(z)$ upon increasing the colloidal concentration is seen to exhibit similar qualitative features to the dependence of $G(z)$ on increasing K_1 calculated based on our model of repulsively interacting charged colloids. The feasibility of describing the structural characteristics of the charged colloidal system using an equivalent hard sphere model has been explored in great detail: With the rescaled effective radius R_{eff} , which is larger than the original radius R of the charged colloidal particles, the OZ/PY/HS model is seen to reproduce the charge-stabilized colloidal structure in a quantitatively satisfactory manner [35, 36, 37, 38]. Therefore, the similarity between our finding presented in Figure 3.7 and the conclusion of previous works [34, 16] is hardly a surprise.

A series of calculated spatial correlations, based on the potential model of Eq. (3.20), are presented in Figure 3.8. In comparison to the $G(z)$ calculated from the potential model of Eq. (3.19) for the purely repulsive charged system (denoted as solid line), with the presence of the short-range attraction, the interplay between these two opposite forces renders a less pronounced oscillation in $G(z)$ due to the competition of the constituent colloids between the clustering structure and the monomeric one. Moreover, similar to the cases of presented in Figures 3.4 and 3.5,

the peak value of $G_{struct}(z)$ given in the inset is seen to shift to a smaller value of z upon an attraction increase, manifesting a greater probability of finding two different colloids at a smaller separation. This strengthening short-range correlation is also reflected in the corresponding $G(z)$, which exhibits a considerable enhancement in magnitude within the range of $1 < z/R < 2$, and the value of $G(z)$ in this region is above zero for the strongest attractive force $K_2 = 5k_B T$.

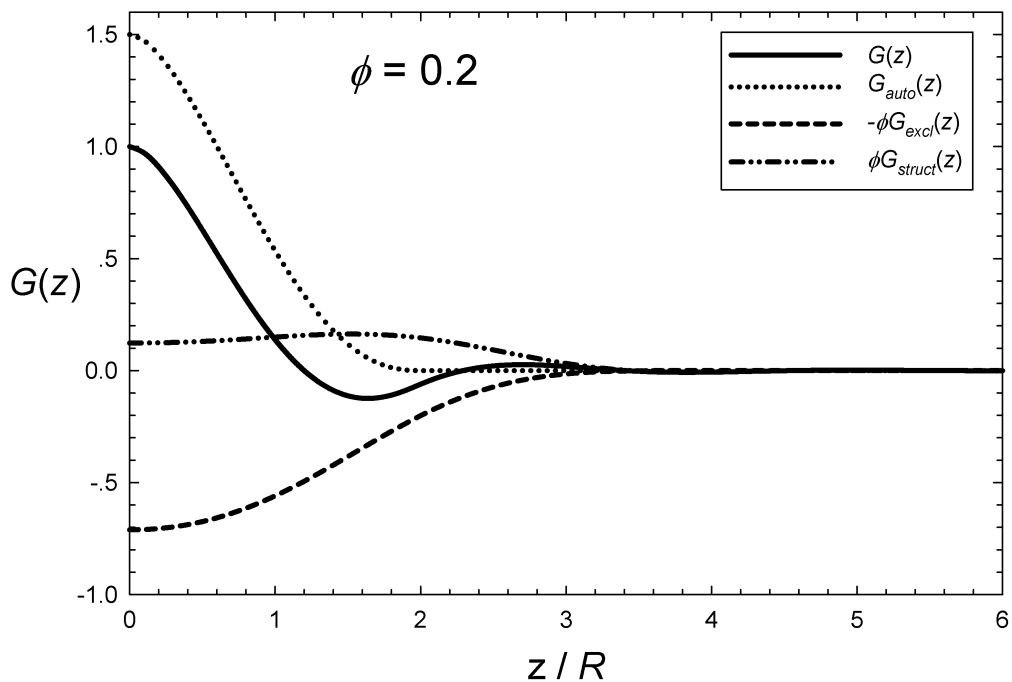


Figure 3.1: SESANS spatial correlation functions of hard sphere colloidal suspension with volume fraction $\phi = 0.2$. The solid line is the normalized SESANS spatial correlation function $G(z)$, the dotted line is the auto correlation function $G_{auto}(z)$, the dashed line is the correlation of the excluded volume $\phi G_{excl}(z)$, and the dash dot dot line is the structure correlation function $\phi G_{struct}(z)$. The $g(r)$ used in $G_{auto}(z)$ is calculated from the solution of OZ equation with PY closure.

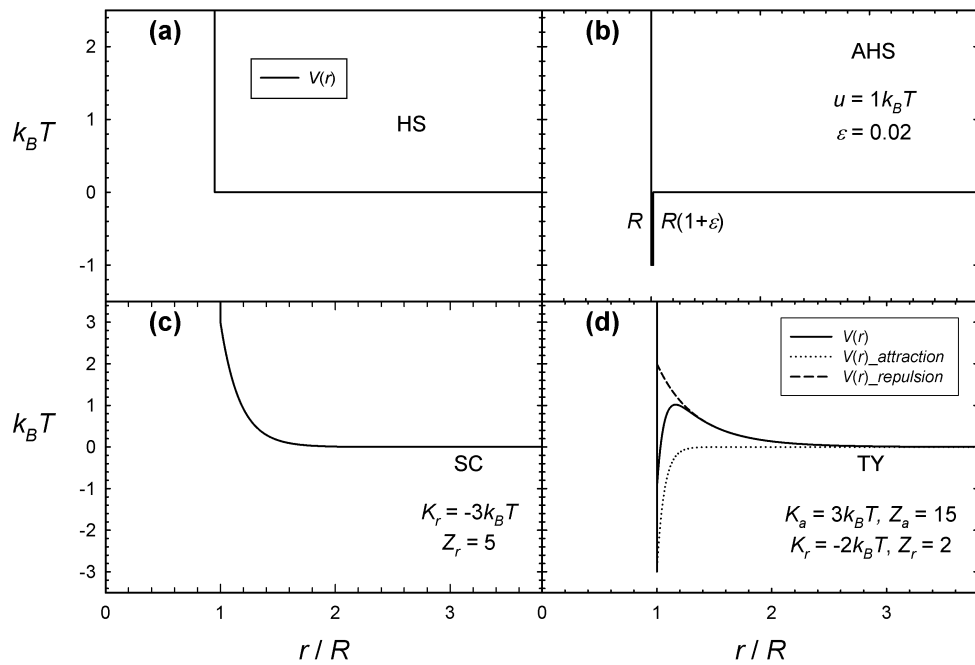


Figure 3.2: The interaction potential models used in the calculation of this study. (a) hard sphere (HS) potential, (b) adhesive hard sphere (AHS) potential, (c) screened Coulomb (SC) repulsion and (d) two-Yukawa (TY) potential.

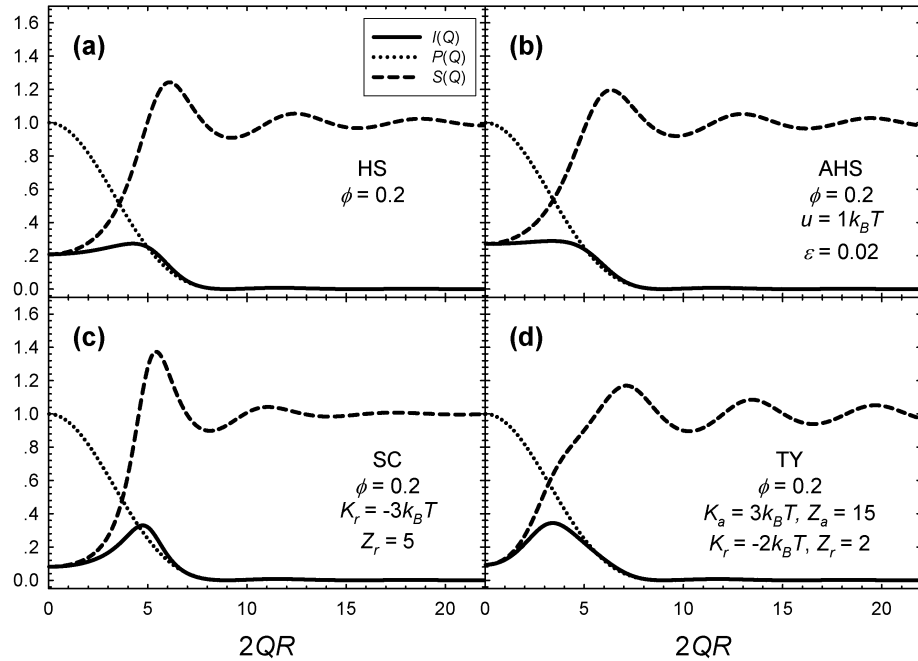


Figure 3.3: Calculated small angle coherent scattering cross sections $I(Q)$ of colloidal suspensions with different potential models displayed in Figure 3.2, along with the form factor $P(Q)$ (dotted lines) and the structure factor $S(Q)$ (dashed lines). In this calculation, the colloidal volume fraction ϕ is set at a constant value of 0.2. The corresponding potential parameters used in the calculation are also presented.

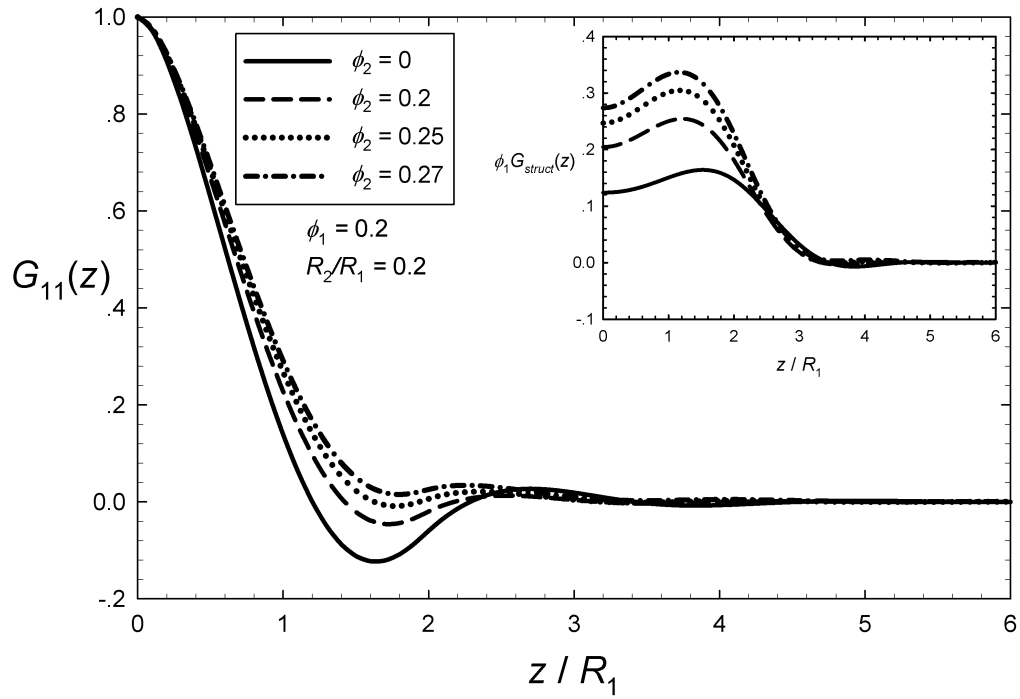


Figure 3.4: The dependence of the partial SESANS correlation functions $G_{11}(z)$ and its structural component $G_{11\text{struct}}(z)$ (inset) on the concentration of the secondary phase of small particle 2. The solid line gives the reference correlation functions of the colloidal suspensions without the presence of particle 2. Upon the increase of the second phase concentration, the attraction due to the depletion force is progressively strengthening which is reflected in the enhancing correlation within the range of $z/R_1 < 3$.

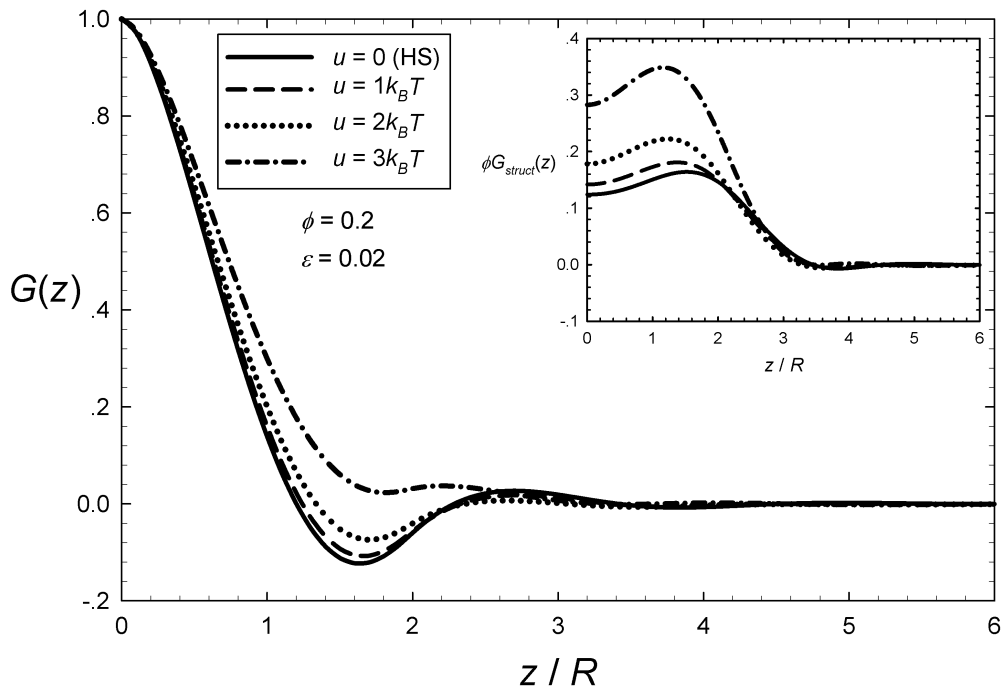


Figure 3.5: $G(z)$ of a colloidal suspension with adhesive hard sphere (AHS) potential whose parameters are specified in the figure. Similar to the features of Figure 3.4, the short range ($z/R < 3$) correlation is progressively enhanced upon increasing the attraction.

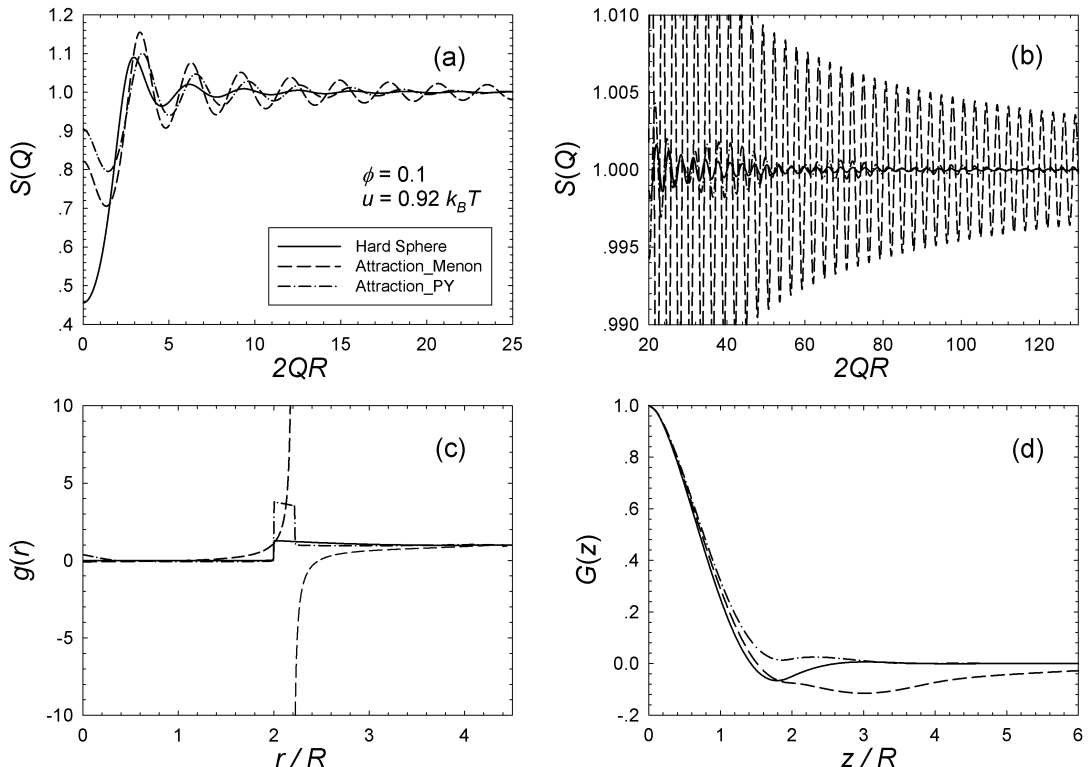


Figure 3.6: The structure factor $S(Q)$, pair distribution function $g(r)$ and SESANS spectrum were calculated with the same parameters selected in the paper from Uca and coworkers. (a) $S(Q)$ in the regular Q range, (b) $S(Q)$ in high Q range, in which the structure factor derived by Menon [25] has an enormous oscillation, (c) the pair distribution function $g(r)$ in which the divergence is observed, (d) SESANS spectrum $G(z)$. The negative part of the diverging $g(r)$ renders the decline of $G(z)$.

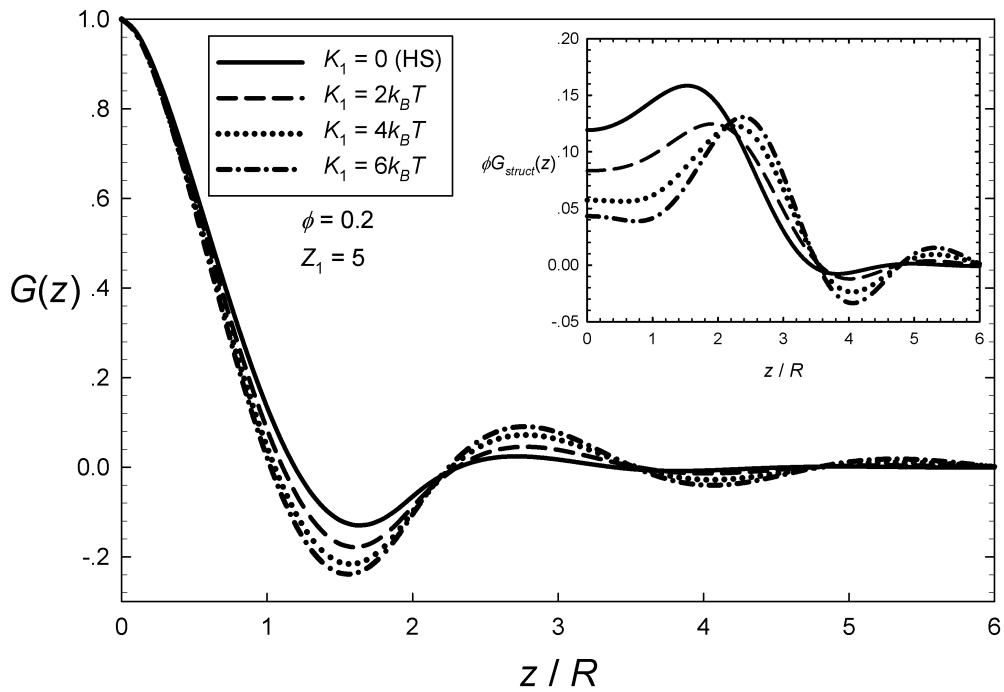


Figure 3.7: $G(z)$ for a colloidal suspension with screened Coulomb (SC) repulsion. The screening length Z_1^{-1} is fixed at 0.2. With the increase of repulsion strength K_1 , the fluctuation of $G(z)$ becomes more pronounced.

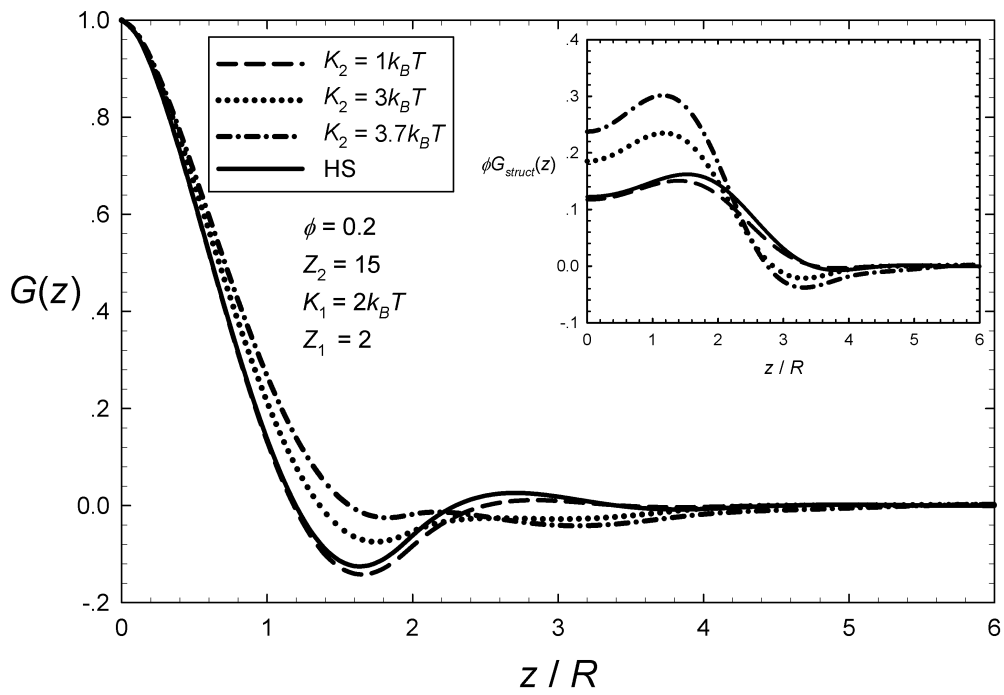


Figure 3.8: The dependence of $G(z)$ for a colloidal suspension with Two-Yukawa (TY) potential as a function of short-range attraction with a fixed repulsion. Detailed description is given in the text.

CHAPTER 4

Interaction in Soft Colloidal System

In Chapter 3, the interaction in concentrated colloidal system is discussed based on the model of impermeable hard spheres with different potential forms. Another unique scientific category, soft colloids, such as star polymers, dendrimers and polymer-based grafted nanoparticles, constitute the hybrids between polymers and colloids [46]. This polymer-colloid structural duality gives rise to rich and complex phase behaviors, leading to unique structural characteristics such as physicochemical homogeneity, environmental responsiveness, and a functionalizable architecture [47]. The emerging scientific understanding of such soft colloids is triggering extensive research activities geared towards their implementation in energy applications such as nanodevices for energy harvesting systems, organic light-emitting diodes, and photosensitizers [41]. With minor chemical modifications, they may be used as templates for anti-cancer, targeted drug and gene transfection delivery vehicles in biomedical applications [42], as well as pollutant getters in environmental technology [43].

There has been extensive interest in understanding the connection between the bulk properties of soft colloidal systems with their microscopic structural characteristics, and their response to variation of external thermodynamic parameters [44, 45]. Complemented by theoretical and computational studies, elastic scattering techniques, especially SANS, have been the principal tools for quantitatively exploring both the intracolloidal architecture and intercolloidal interactions, as well as their influences on collective macroscopic properties [43, 44, 45].

Soft colloids are characterized by an accessible molecular interior. Due to the continuous change in the scattering length density across the colloid/solvent interface, it is difficult to define the soft colloidal radius R without assumptions

²This chapter previously appeared as: Xin Li, Chwen-Yang Shew, Yun Liu, Roger Pynn, Emily Liu, Kenneth W. Herwig, Gregory S. Smith, J. Lee Robertson, and Wei-Ren Chen, “Prospect for characterizing interacting soft colloidal structures using spin-echo small angle neutron scattering”, *J. Chem. Phys.*, Vol. 134, 094504, 2011, pp. 1-13.

about solvent distributions based on some physical model. In other words, the partition of the intermolecular Debye function into γ_{ovl} (region for $g(r) = 0$) and γ_{cross} (region for $g(r) \neq 0$) is no longer meaningful in the case of interacting soft colloidal suspension. Instead of Eq. (3.1), the following equation must be used directly to calculate the soft colloidal $G(z)$ [18, 48]

$$\gamma(r) = \gamma_{auto}(r) + n \int_0^\infty \gamma_{cross}(r, a)[g(a) - 1]4\pi a^2 da, \quad (4.1)$$

where a is the distance between the centers of two particles.

Determination of an analytical equation for γ_{cross} has proven difficult within the framework of existing soft colloid models. For any given functional forms of the colloidal density profile $\rho(r)$ and pair distribution function $g(r)$, $G(z)$, which now takes the following form

$$G(z) = G_{auto}(z) + nG_{struct}(z), \quad (4.2)$$

can be calculated numerically based on the previously developed approach in Chapter 3. Note $nG_{struct}(z)$ comes from the Abel transform of the second term on RHS in Eq. (4.1).

4.1 Core-Shell Structure

Before going any further into the structural study of the soft colloids, it is instructive to consider the characteristics of the impermeable core-shell structure. Compared to homogeneous spheres, the effect of radial inhomogeneity is reflected in the correlation function, which will be discussed in this section.

As presented in Chapter 3, the spatial information rendered by conventional elastic scattering techniques such as SANS can be separated into a product of the intracolloidal correlation $P(Q)$, and the intercolloidal component, $S(Q)$. The traditional approach in SANS data analysis [1, 2, 23, 29, 49, 50, 51, 52, 53, 54] is to determine $P(Q)$ and $S(Q)$ independently by making measurements on dilute samples (to obtain $P(Q)$) and on more concentrated dispersions. However, the convolution relationships familiar for Fourier transforms are no longer valid in the Abel

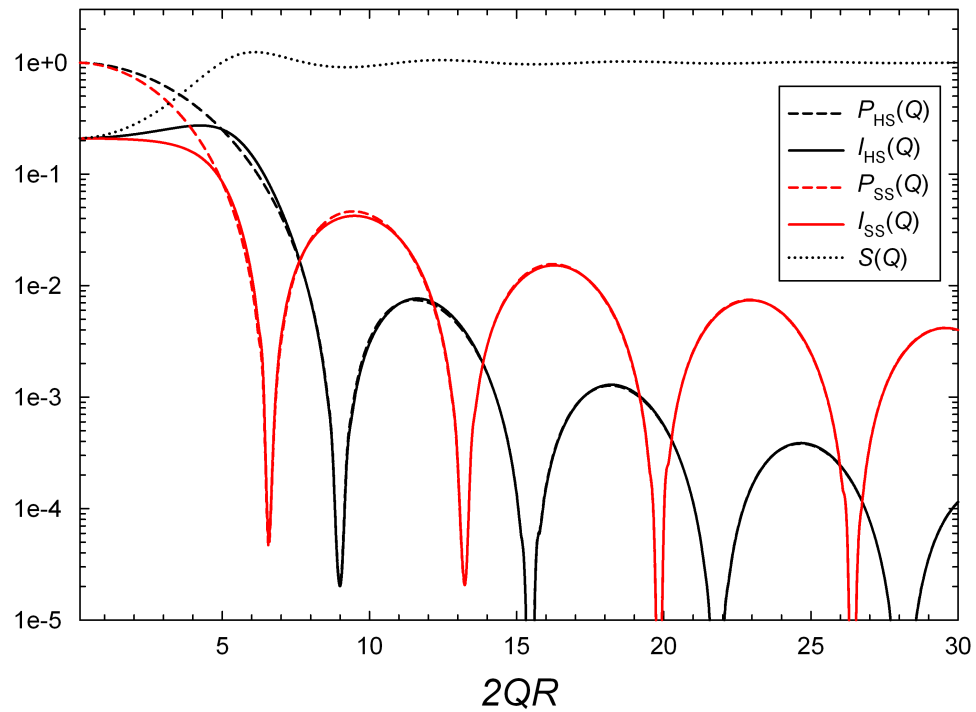


Figure 4.1: The semilog plots of the SANS coherent scattering cross section $I(Q)$ (solid lines), the form factor $P(Q)$ (dashed lines) and the structure factor $S(Q)$ (black dotted lines) for the uniform hard spheres (black) and spherical shell (red). The radius of the hard sphere R is identical to the outer radius of the shell radius. The volume fraction ϕ is set to be 0.2 in the calculation. The ratio of the shell thickness δ to R is 0.1. At low Q , $I_{SS}(Q)$ and $I_{HS}(Q)$ are seen to be characterized by a single peak originating from the suppression of scattering at $Q = 0$ by the structure factor, $S(Q)$.

transform. It is no longer possible to compartmentalize the hierachal ordering information in $G(z)$, in the way we did in Eqs. (3.7) to (3.9) for $I(Q)$. Therefore, in $G(z)$ the intracolloidal correlation is not only present in the first term on the RHS of Eq. (3.2), but also reflected in the second and third terms which represent the self-shadowing effect and intercolloidal correlation. This difference can be visualized by the following example: Figure 4.1 gives the SANS $I(Q)$, along with the constituent $P(Q)$ and $S(Q)$ corresponding respectively to a uniform hard sphere (HS) and a spherical shell (SS). The volume fraction ϕ used in this calculation is 0.2 and the surfaces for both cases are set to be impermeable. Therefore the two $S(Q)$, obtained from solving the Ornstein-Zernike (OZ) equation with Percus-Yevick (PY) closure [12], are identical to each other. The HS form factor $P_{HS}(Q, R)$ takes the following expression:

$$P_{HS}(Q, R) = \left[\frac{3[\sin(QR) - QR \cos(QR)]}{(QR)^3} \right]^2, \quad (4.3)$$

where R is the radius. The SS form factor $P_{SS}(QR)$ is found to be

$$P_{SS}(Q, R) = |F_{SS}(Q, R)|^2, \quad (4.4)$$

where

$$F_{SS}(Q, R) = \frac{(\Delta\rho_{in} - \Delta\rho_{shell})V(R - \delta)F_{HS}(Q, R - \delta) + \Delta\rho_{shell}V(R)F_{HS}(Q, R)}{(\Delta\rho_{in} - \Delta\rho_{shell})V(R - \delta) + \Delta\rho_{shell}V(R)}, \quad (4.5)$$

where $\Delta\rho_{in} \equiv \rho_{in} - \langle \rho \rangle$ represents the difference in the scattering length density of the spherical interior region (ρ_{in}) and that for the surrounding medium ($\langle \rho \rangle$). Likewise, $\Delta\rho_{shell}$ gives the difference between the shell scattering-length density ρ_{shell} and $\langle \rho \rangle$. δ is the thickness of the shell, R is the outer radius of the shell and $R - \delta$ is the inner radius. In this calculation, the ratio of $\frac{\delta}{R}$ is set to be 0.1 and $\Delta\rho_{shell}$ to be identical to the scattering length density difference in the SS case. The spherical shell model has been commonly used to quantify the vesicle structure in numerous SANS data analyses [2, 35]. As an example, $\Delta\rho_{in}$ is set to be zero in this study to simulate bilayer vesicles which enclose part of the solvent [55]. Within the SANS Q range,

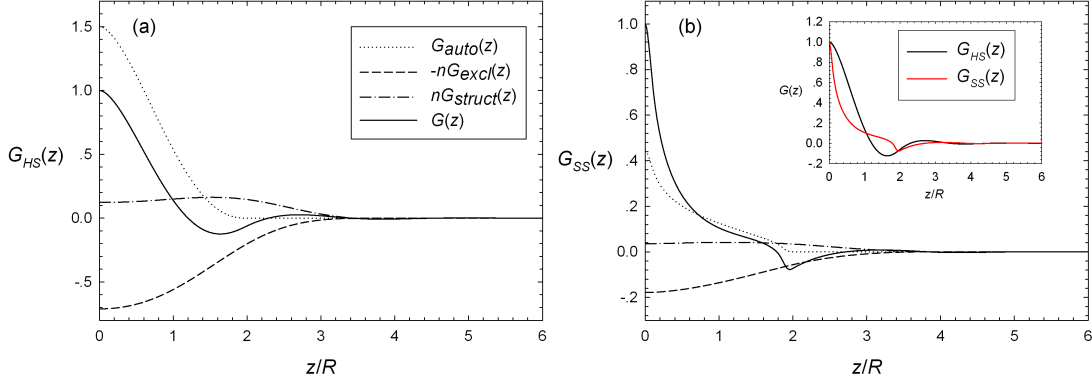


Figure 4.2: The SESANS correlation function $G(z)$ for hard sphere (a) and impermeable spherical shell (b) calculated based on the same structural parameters used in Figure 4.1. As shown in the inset of Figure 4.2(b), although $I_{SS}(Q)$ is seen to be qualitatively similar to $I_{HS}(Q)$ (Figure 4.1), $G_{SS}(z)$ is found to be characteristically different from $G_{HS}(z)$. The comparison of $G_{HS}(z)$ (black solid line) and $G_{SS}(z)$ (red solid line) is given in the inset of Figure 4.2(b). The observed difference, as discussed in the text, is attributed to the radial intraparticle inhomogeneity.

$P_{HS}(Q, R)$ is seen to shift towards higher Q , in comparison to $P_{SS}(Q, R)$ with the same contrast as $\Delta\rho_{shell}$. Given an identical $S(Q)$, both $I_{SS}(Q)$ and $I_{HS}(Q)$ exhibit at most a single maxima reflecting, in principle, the first interaction peak of $S(Q)$. Without additional information about the effective intercolloidal interaction, usually provided by other independent experimental techniques, it is therefore difficult to unambiguously determine the structural details of interacting colloidal suspensions by SANS data analysis alone especially when inevitable data smearing factors such as instrument resolution and thermodynamically driven polydispersity in global size are taken into consideration.

A qualitatively different picture is obtained from the $G(z)$ (Figure 4.2) calculated based on the same structural parameters used in Figure 4.1: Because the

intracolloidal self correlation is implicitly incorporated in γ_{cross} in the RHS of Eq. (3.1), $G_{SS_struct}(z)$ is seen to be different in magnitude from $G_{HS_struct}(z)$ even with identical correlations between colloidal particles (the same $S(Q)$). The same observation also applies to the differences between $G_{HS_excl}(z)$ and $G_{SS_excl}(z)$. Secondly, it is important to point out that the normalized SESANS correlation function $G(z)$ for interacting uniform spheres, such as the hard sphere $G_{HS}(z)$ shown in Figure 4.2(a) and those calculated based on various effective potential models in Chapter 3, are characterized by the presence of a minimum centered at a constant value of the SESANS correlation length z_{\min} , $z_{\min}/R \sim 1.6$ for colloidal solutions with volume fraction $\phi = 0.2$. Since SESANS measures the projection of the Debye correlation function $\gamma(r)$ onto the \hat{z} direction, the minimum of $G(z)$ at z_{\min} is a consequence of integration of $\gamma(r)$ over all \hat{r} directions. Therefore the location and amplitude of z_{\min} are determined by both $g(r)$ and $\Delta\rho(r)$ as suggested by Eqs. (3.1) and (3.2). In the spherical shell case, the position of z_{\min} is dominated by the intra-molecular structure (namely $\Delta\rho(r)$), which is different from that of hard sphere case which in principle reflects the feature of $g(r)$. Based on a Monte-Carlo computational study, Shew *et al.* [56] have recently discussed the quantitative spatial dependence of z_{\min} on the colloidal spatial distribution function $g(r)$ and determined the mathematical connection between the magnitude of this minimum in $G(z)$ and the contact value of the corresponding $g(r)$. However, this signature minimum, universally observed for colloidal systems consisting of particles with uniform intracolloidal density profile, is no longer present in $G_{SS}(z)$. Instead, as shown in Figure 4.2(b) and its inset, a qualitatively different minimum, with a more well-defined center located at $z_{\min}/R \sim 2$, is observed. The minimum in $G_{SS}(z)$ is clearly reflective of the $G_{auto}(z)$ of the spherical shell, but amplified by its exclusive counterpart. This differs significantly from the broad minimum in $G_{HS}(z)$ and those calculated previously which arises from the competition between their rapidly varying $G_{auto}(z)$ and $G_{excl}(z)$ (having opposite signs) with the length scale corresponding to the global particle size ($z/R < 2$). We further explore the dependence of $G_{HS}(z)$ and $G_{SS}(z)$ on the colloidal volume fraction ϕ in Figure 4.3. For hard spherical particles with uniform density profile [Figure 4.3(a)] the minimum of $G_{HS}(z)$ is seen to shift from 1.8 to 1.4

upon increasing ϕ from 0.1 to 0.3. However, for the impermeable hollow spherical system [Figure 4.3(b)], the locations of the minima for the $G_{SS}(z)$ corresponding to different ϕ remain close to a constant value of $z_{\min}/R \sim 2$. As indicated by the insets, our calculation suggests that the origin of this observed invariance in z_{\min} of $G_{SS}(z)$ is the suppressed $G_{SS_struct}(z)$ (right inset) due to radial inhomogeneity, in comparison to the significant increase in the evolving $G_{HS_struct}(z)$ for the hard sphere case (left inset). One common perception about analysis of SANS spectra collected from any colloidal system with non-negligible interactions is that determination of the intraparticle density profile in $P(Q)$, is often complicated by the presence of $S(Q)$ (in addition to other masking effects such as the incoherent background and several instrumental factors). In this regard, our calculation suggests that SESANS is not limited by these constraints and may be capable of resolving the intraparticle density inhomogeneities of interacting colloidal systems.

4.2 Soft Colloidal Structure

Unlike the impermeable colloidal particles discussed above, soft colloids feature a non-uniform intraparticle mass distribution which is intrinsically different from both the hollow spherical shell and the homogeneous solid sphere models. As indicated by the normalized intraparticle density profile $\rho(r)$ schematically depicted in Figure 4.4(a), the mass distribution of a general soft colloidal particle exhibits a maximum at its center and decays monotonically towards the peripheral region. As a result of this continuous change in density profile, accessibility of the colloidal interior is reflected in the soft effective intercolloidal interaction $V(r)$ characterized by a finite repulsive strength at the colloidal center, as opposed to exclusive repulsion for the case of a hard sphere potential [Figure 4.4(b)]. Depending on the structural details unique to each specific soft colloidal system, different models of the coherent scattering cross section have been used in SANS data analysis to quantify structural softness by parameterizing the corresponding $P(Q)$ and $S(Q)$ with varying degrees of mathematical sophistication [23, 44, 49, 57, 58, 59, 60, 61, 62]. It is not our intention to quantify the differences among the array of $G(z)$ calculated from the different soft colloidal models. Instead, our attention is confined to qualitatively addressing

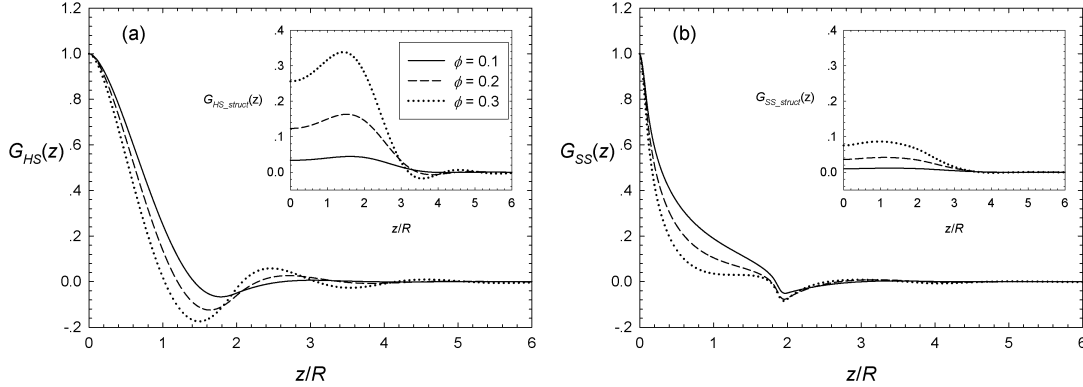


Figure 4.3: The dependence of the SESANS correlation function $G(z)$ on the colloidal volume fraction ϕ : (a) For the hard spherical particles with uniform density profile, upon increasing ϕ from 0.1 to 0.3, the minimum of $G_{HS}(z)$ is seen to shift from 1.8 to 1.4. (b) For the impermeable hollow spherical system, the locations of the minima for the $G_{SS}(z)$ corresponding to different ϕ , however, in principle remain at a constant value of $z_{\min}/R \sim 2$. As indicated by the insets, this invariance is mainly due to the difference in the evolution of $G_{\text{struct}}(z)$, and z_{\min} is strongly related to the peak position of $G_{\text{struct}}(z)$. However, in hollow spheres, $G_{\text{struct}}(z)$ is greatly suppressed, so its influence on the minimum position is diminished.

the general characteristics of the $G(z)$ of interacting soft colloids via comparison with its reference hard spherical counterpart. Here we consider the intracolloidal density profile [dotted line in Figure 4.4(a)] and intercolloidal interaction (dotted line in Figure 4.4(b)) as approximated by the soft ball model proposed by Likos which takes into account the additional softening effect, in comparison to the hard colloidal system, introduced by the structural openness at the colloidal periphery and interior [43, 49]. Moreover, the number density (n) range studied in this work is deliberately chosen to be less than the overlapping density n^* ($\approx 0.0379 \text{ nm}^{-3}$) where the factorization approximation of SANS coherent scattering cross section is

valid, with the particle volume referring to the experimental value of 9.818 nm^3 used by Likos [44, 49]. Given the same number density, spatial correlation functions are compared on the basis of equivalent global size. Specifically, for the ultrasoft colloidal model [49] the soft colloidal radius of gyration R_g is set to be identical to the radius of the hard sphere R . Figures 4.4(c) and 4.4(d) present respectively the calculated single particle scattering functions $P(Q)$ and $G_{auto}(z)$ for both cases.

In Figure 4.5 we present the dependence of the pair distribution function $g(r)$ on colloidal number density n for hard spherical system [$g_{HS}(r)$, panel (a)] and soft colloidal system [$g_{SC}(r)$, panel (b)]. Both $g_{HS}(r)$ and $g_{SC}(r)$ were obtained by solving the Ornstein-Zernike (OZ) equation with the Percus-Yevick (PY) closure [12, 49]. The evolution of $g_{HS}(r)$ presented in Figure 4.5(a) is characterized by two features: First, the contact value of $g_{HS}(r)$, namely $g_{HS}(2R)$ just beyond the prohibited region of $\frac{r}{R} < 2$ is seen to increase with increasing n . Secondly, oscillation of $g_{HS}(r)$ within the range of $2 < \frac{r}{R} < 6$ becomes progressively more pronounced with increasing n . Meanwhile for $g_{SC}(r)$ presented in Figure 4.5(b), the prohibited region no longer exists in the absence of the harsh exclusive repulsion of the hard sphere. Finite values of $g_{SC}(r)$ are observed within the colloidal central region ($\frac{r}{R} < 2$). Moreover, only a moderate increase in the magnitude of $g_{SC}(2R)$ and a smooth variation in $g_{SC}(r)$ when $2 < \frac{r}{R} < 6$ are seen as a function of n due to the ultrasoft intercolloidal interaction.

Figure 4.6 compares the SANS absolute intensity distributions $I(Q)$ for the hard spherical system [$I_{HS}(Q)$, panel(a)] and the soft colloidal system [$I_{SC}(Q)$, panel(b)], as a function of n . They are calculated based on $S_{HS}(Q)$ and $S_{SC}(Q)$ which are the Fourier components of $g_{HS}(r)$ and $g_{SC}(r)$ shown in Figure 4.5, and the corresponding form factors presented in Figure 4.4(c). Upon increasing n , the evolution of both the calculated $I_{HS}(Q)$ and $I_{SC}(Q)$, as well as those experimentally observed [23, 57, 63, 64], are characterized by the same qualitative feature: The interaction peak of $I(Q)$ is progressively established and gradually shifts towards the higher Q region, reflecting evolution of the first correlation peak of the corresponding $S(Q)$, as indicated in the insets. The main difference between $I_{HS}(Q)$ and $I_{SC}(Q)$ is seen to be quantitative: At each given n , the interaction peak of $I_{HS}(Q)$ is more

significant than that of $I_{SC}(Q)$ due to the more pronounced first correlation peak in $S_{HS}(Q)$ originating from the strong exclusive repulsion. However, a fundamental difference between the corresponding SESANS spatial correlation functions for hard spheres [$G_{HS}(z)$, panel 7(a)] and soft colloids [$G_{SC}(z)$, panel 7(b)] is revealed by our calculation: Although the increase in n renders a steady shift in the locations of the minima towards the lower $\frac{z}{R}$ region for both $G_{HS}(z)$ and $G_{SC}(z)$, the progressively increasing oscillation in $G_{HS}(z)$ [Figure 4.7(a)], beyond the minimum, no longer exists in $G_{SC}(z)$.

The reason for this observation is given in Figure 4.8, which displays the calculated $G_{HS}(z)$ and $G_{SC}(z)$, and their constituent components as given in Eq. (4.2), with a colloidal number density $n = 0.0241 \text{ nm}^{-3}$: It is evident that the oscillation of $G_{HS}(z)$ is a reflection of $G_{HS_struct}(z)$ because the contribution from the intra-particle self correlation $G_{HS_auto}(z)$ becomes vanishingly small when $\frac{z}{R} > 2$. In other words, structural softness is revealed in the absence of oscillations in $G_{SC}(z)$. This is the consequence of the fact that the intercolloidal ultrasoft Gaussian potential, in comparison to the hard sphere interaction with the same volume fraction, is unable to generate sufficient repulsion to sustain significant local ordering, as seen in $g_{HS}(r)$ in Figure 4.5(a). From the characteristically different $G_{HS}(z)$ and $G_{SC}(z)$ presented in the inset of Figure 4.8, one can appreciate the complementarity of the SESANS technique to conventional SANS techniques in characterizing interacting soft colloidal systems. This is partly due to SESANS capability to access length scales comparable to that of light scattering, but more importantly because of its considerable advantage in revealing unique features of soft interactions. While this theoretical study demonstrates the capability of the SESANS technique to identify soft interactions via comparison of $G_{HS}(z)$ and $G_{SC}(z)$, the focus has not been placed on quantifying structural softness due to the constraint of the mathematically convenient Gaussian model [49] used in this work which lacks any mechanism to account for the dependence of the effective soft colloidal interaction on the detailed intracolloidal density profile. Nevertheless, SESANS shows promise for quantitatively determining the degree of structural softness as well, but this will require additional complexity in the mathematical models.

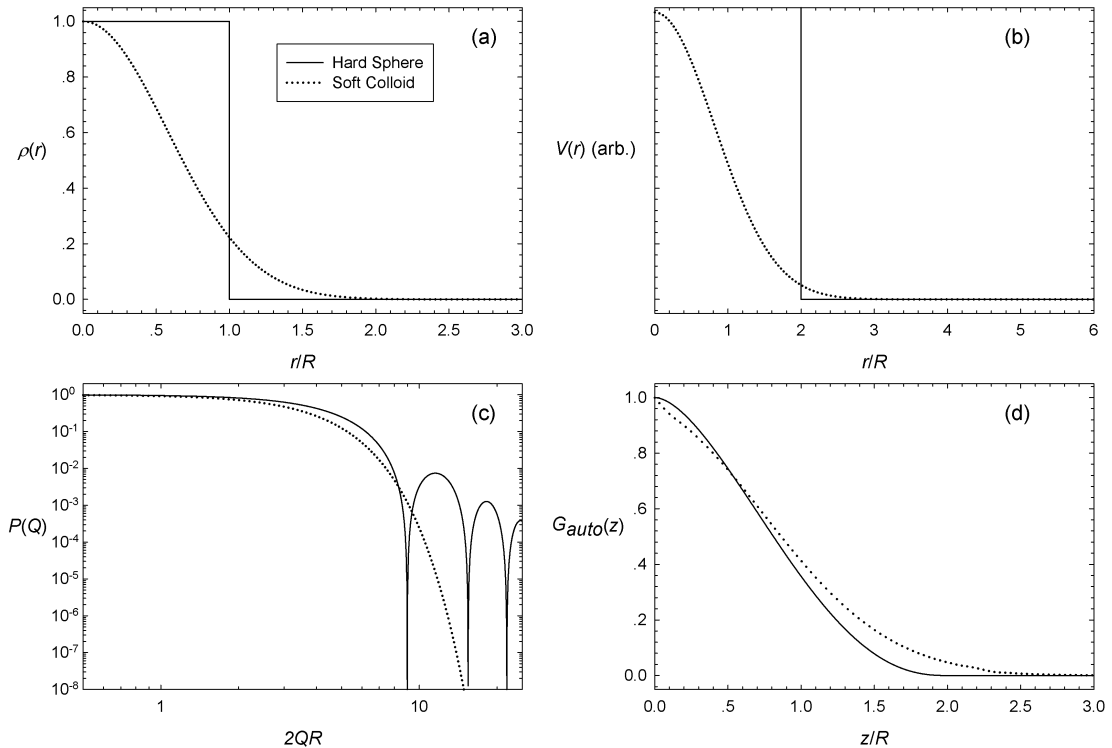


Figure 4.4: (a) The comparison of the intracolloidal density profile $\rho(r)$ for uniform hard sphere (solid line) and soft colloid (dotted line). (b) The schematic representation of the effective inter-colloidal interaction potential $V(r)$ for hard spheres and soft colloids. (c) The corresponding form factor $P(Q)$ and (d) SESANS correlation function $G(z)$. The Gaussian approximation proposed by Likos *et al* [49] is used to model the soft colloidal $\rho(r)$ and $V(r)$ in our calculation.

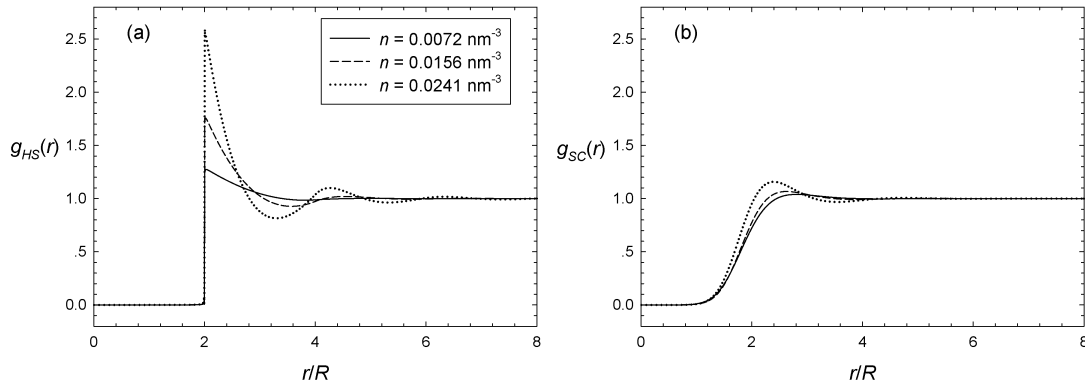


Figure 4.5: The dependence of the pair distribution function $g(r)$ on colloidal number density n for hard spherical system [$g_{HS}(r)$, panel (a)] and soft colloidal system [$g_{SC}(r)$, panel (b)]. Both $g_{HS}(r)$ and $g_{SC}(r)$ are calculated from the Ornstein-Zernike (OZ) equation with the Percus-Yevick (PY) closure. The selected number density for each curve corresponds to the volume fraction of 7.02%, 15.28%, and 23.69%, respectively, as in the experiment carried by Likos [49]. For the hard sphere case, the contact value of $g_{HS}(r)$, namely $g_{HS}(2R)$ just beyond the excluded region of $\frac{r}{R} < 2$ is seen to increase upon increasing n . Meanwhile, the oscillation of $g_{HS}(r)$ within the range of $2 < \frac{r}{R} < 6$ becomes progressively more pronounced. For the soft colloidal system, the prohibited region no longer exists in the absence of the harsh exclusive repulsion. A finite value of $g_{SC}(r)$ is observed within the colloidal central region ($\frac{r}{R} < 2$). Moreover, only a moderate increase in the magnitude of $g_{SC}(2R)$ and smooth variation in $g_{SC}(r)$ when $2 < \frac{r}{R} < 6$ are revealed as a function of n .

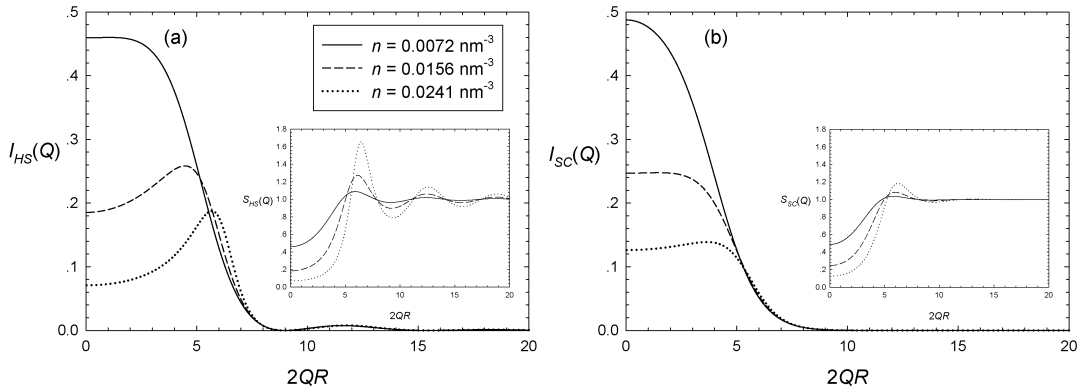


Figure 4.6: The SANS absolute intensity $I(Q)$ as a function of colloidal number density n for a hard spherical system [$I_{HS}(Q)$, panel(a)] and a soft colloidal system [$I_{SC}(Q)$, panel (b)]. Upon increasing n , both $I_{HS}(Q)$ and $I_{SC}(Q)$ are characterized by the same qualitative feature: The interaction peak of $I(Q)$ becomes more well-defined and shifts towards the higher Q region, which in principle reflects the evolution of $S(Q)$ given in the inset. However, quantitatively, the increase in the magnitude of $I_{HS}(Q)$ is more significant than that of $I_{SC}(Q)$, because of the stronger first correlation peak in $S_{HS}(Q)$ originating from the exclusive repulsion.

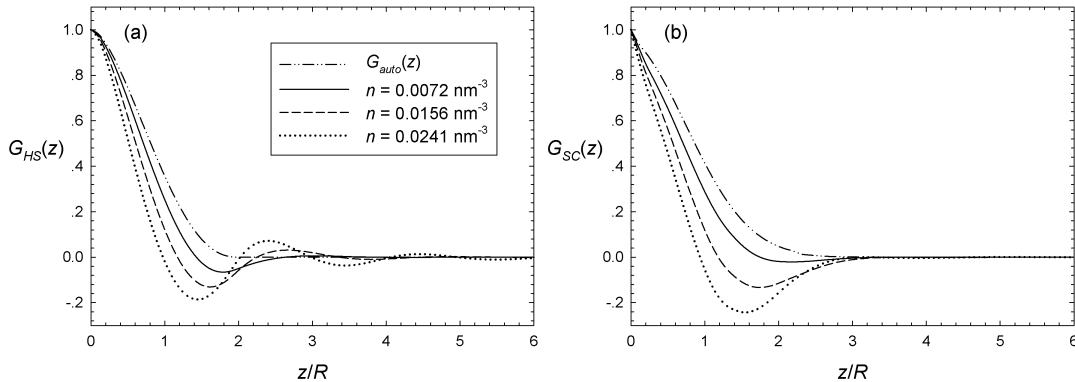


Figure 4.7: The SESANS spatial correlation function $G(z)$ as a function of colloidal number density n for a hard spherical system [$G_{HS}(z)$, panel(a)] and a soft colloidal system [$G_{SC}(z)$, panel(b)]. The most significant qualitative difference between $G_{HS}(z)$ and $G_{SC}(z)$ is the disappearance of the oscillation in the range of $\frac{z}{R}$ beyond the minimum of $G(z)$.

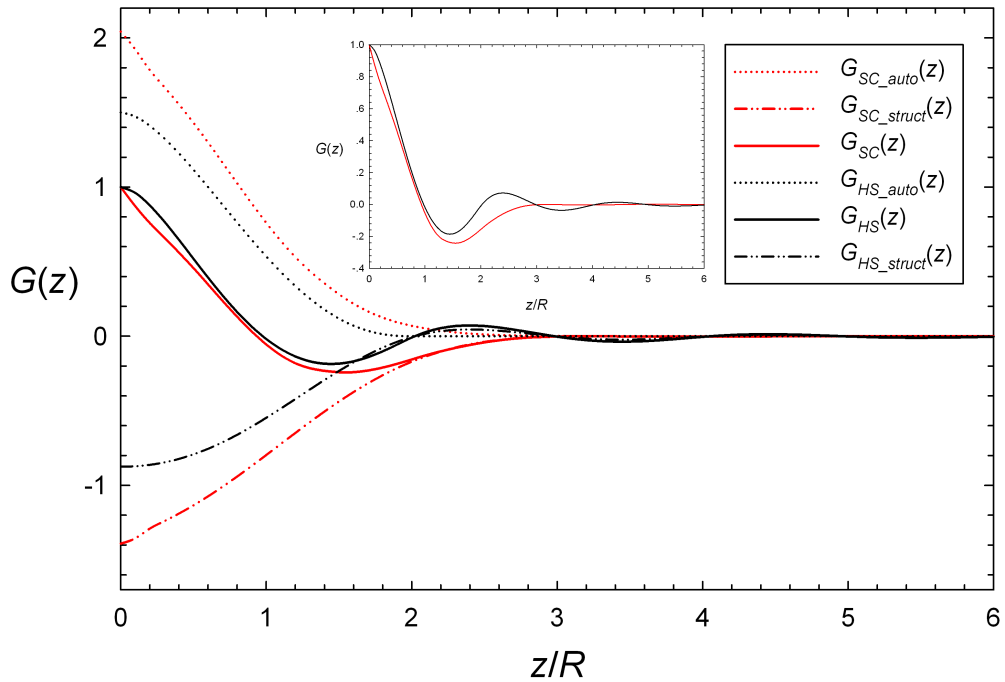


Figure 4.8: The calculated $G_{HS}(z)$ and $G_{SC}(z)$, and their constituent components given in Eq. (4.2), with colloidal number density $n = 0.0241 \text{ nm}^{-3}$. It is clear that the oscillation of $G_{HS}(z)$ is reminiscent of $G_{HS_struct}(z)$, which reflects the exclusive volume effect of the hard sphere system. The inset give an enlarged view of the $G_{HS}(z)$ and $G_{SC}(z)$.

CHAPTER 5

Contrast Variation in SESANS

Soft matter in all its forms is generally characterized by intrinsically complex structures with relevant length-scales ranging from nm to μm . Many commonly seen soft matter systems consist of atomic or molecular components which often contain a considerable amount of hydrogen. Therefore they are efficient neutron scatterers due to the large incoherent scattering cross section of hydrogen originating from the spin-dependent nature of the neutron-proton interaction [65]. When interacting with neutrons, deuterium exhibits distinctly different scattering properties as compared to hydrogen. It has been common practice to exploit this difference by isotopically substituting selected hydrogen atoms in the targeted soft matter system with deuterium without causing a radical change to the physical or chemical properties of the materials, and hence facilitate structural investigations using neutron scattering techniques. Evidenced by the documented scientific activities, the so-called contrast variation technique has been extensively used in numerous elastic neutron scattering experiments, such as SANS, in order to alter the contrast of the targeted system for the sake of selectively structural highlighting [66, 53, 2].

In SESANS experiment, the measurement of depolarization performed an automatic Fourier transform of the scattering intensity $I(Q)$ on \hat{z} direction which is the tilt direction perpendicular to both the incident beam and the magnetic field. So the total SESANS correlation function is

$$G_{total}(z) = \int_0^{\infty} I(Q) \cos(zQ_z) dQ_z$$

³This chapter previously appeared as: Xin Li, Bin Wu, Yun Liu, Roger Pynn, Chwen-Yang Shew, Gregory S. Smith, Kenneth W. Herwig, J. Lee Robertson, Wei-Ren Chen, and Li Liu, “Contrast variation in spin-echo small angle neutron scattering”, *J. Phys.: Condens. Matter* (In Press).

⁴Portion of this chapter previously appeared as: Xin Li, Chwen-Yang Shew, Lilin He, Flora Meilleur, Dean A. A. Myles, Emily Liu, Yang Zhang, Gregory S. Smith, Kenneth W. Herwig, Roger Pynn and Wei-Ren Chen, “Scattering functions of Platonic solids”, *J. Appl. Cryst.* Vol. 44, 2011, pp. 545-557.

$$= \int_0^\infty [I_{coh}(Q) + I_{inc}] \cos(zQ_z) dQ_z, \quad (5.1)$$

where $I_{coh}(Q)$ is the coherent part and I_{inc} is the constant incoherent contribution. The incoherent scattering, with a large enough Q_z range, will result in a $\delta(z)$ function at $z \rightarrow 0$, which will be excluded from the normally measured z range. Therefore the coherent contribution from $I_{coh}(Q)$ is usually the measured SESANS spectrum $G(z)$. In other words, the measured SESANS spectrum $G(z)$ only records the coherent scattering information in principle, while SANS $I(Q)$ collects both coherent and incoherent scattering and the strong incoherent background may inundate the signal with the variation of contrast. The focus of this chapter is to develop the application of contrast variation technique, which was commonly used in SANS study, in SESANS experiment thus allowing this new real-space scattering technique to resolve the structural characteristics with its full capability.

To illustrate the unique advantage and intrinsic limit of contrast variation embedded in each implementation of neutron scattering, the correlation functions measured by SANS and SESANS, respectively, are calculated based on several colloidal model systems to demonstrate the evolution of their main features upon changing the contrast level. To enhance the visibility of colloids, one frequently used method is to increase the contrast by varying the hydrogen to deuterium (H/D) ratio of their surrounding solvent. For such a practice, the molar ratio of deuterated solvent, which gives the deuteration level of the solvent, can be expressed as

$$\eta = \frac{n_{D_2O}}{n_{D_2O} + n_{H_2O}}, \quad (5.2)$$

where n_{D_2O} is the number density of D_2O and n_{H_2O} is the number density of H_2O . The single particle autocorrelation function is therefore defined as Eq. (3.4)

$$\gamma_{auto}(\mathbf{r}) = \int_V \Delta\rho(\mathbf{r}') \Delta\rho(\mathbf{r}' - \mathbf{r}) d^3\mathbf{r}', \quad (5.3)$$

where V is the sample volume with a single particle and $\Delta\rho(r)$ is the difference of the scattering contrast. The familiar form factor $P(Q)$ in SANS is given by the Fourier transform of $\gamma_{auto}(\mathbf{r})$,

$$P(Q) = \left\langle \int_V \gamma_{auto}(\mathbf{r}) \exp(-i\mathbf{Q} \cdot \mathbf{r}) d^3\mathbf{r} \right\rangle, \quad (5.4)$$

where the bracket represents the angular average and the scattering vector amplitude Q is a scalar connected to the scattering angle, θ , and the wavelength of the radiation, λ , by $Q = \frac{4\pi}{\lambda} \sin \frac{\theta}{2}$. Then the measured SANS scattering intensity $I(Q)$ can be expressed as

$$\begin{aligned} I(Q) &= I_{coh}(Q) + I_{inc} = nP(Q)S(Q) + I_{inc} \\ &= nP(0)P_{norm}(Q)S(Q) + I_{inc}, \end{aligned} \quad (5.5)$$

where $I_{coh}(Q)$ is the coherent part and I_{inc} is the constant incoherent contribution which is only related to the H/D ratio in the solvent. n is the number density and $S(Q)$ is the structure factor. Moreover, if the system consists of monodispersed spherical particles, the scattering power of this model colloidal system is given by

$$\begin{aligned} P(0) &= P(Q \rightarrow 0) = \int_V \gamma_{auto}(\mathbf{r}) d^3\mathbf{r} \\ &= \left\{ \int_V \Delta\rho(\mathbf{r}) d^3\mathbf{r} \right\}^2 = \left\{ \int_V 4\pi r^2 \Delta\rho(r) dr \right\}^2, \end{aligned} \quad (5.6)$$

Therefore, the normalized form factor $P_{norm}(Q)$, which decays from $P_{norm}(Q \rightarrow 0) = 1$, will only be related to the shape of $\Delta\rho(r)$ and $\gamma(r)$ rather than their absolute values.

Without loss of generality, the dependence of the scattering length density contrast between the solute and the solvent in the solvent contrast can be expressed as a function dependent of r and η , $\Delta\rho(r, \eta)$. In the special case that the intra-molecular density profile is variant with a constant factor within the whole real space range,

$$\Delta\rho(r, \eta) = C(\eta) \Delta\rho(r, \eta = 1), \quad (5.7)$$

where $C(\eta)$ is a scale factor for scattering ability which is a function of η and does not depend on r . $I_{coh}(Q)$ will be just proportional to $C^2(\eta)$, and $G(z)$ will not show any dependence on the contrast after normalized by the initial polarization. If one defines the following function

$$F(r, \eta) = \frac{\rho_{solvent}(r, \eta) - \rho_{background}(\eta)}{\rho_{colloid}(r)}, \quad (5.8)$$

where $\rho_{solvent}(r, \eta)$ is the intra-colloidal scattering length density distribution of solvent along the radial direction, $\rho_{background}(\eta)$ is the value of the scattering length density for the bulk solvent, and $\rho_{colloid}(r)$ is the intra-colloidal non-solvent scattering length density profile. When Eq. (5.7) is satisfied, the corresponding $F(r, \eta)$ is only related to η and independent of r and therefore can be further simplified as [10]

$$F(r, \eta) \equiv F(\eta), \quad (5.9)$$

Either Eq. (5.7) or (5.9) can be used as the criterion to define the system which can be applied for SESANS contrast variation technique. When Eq. (5.7) or (5.9) is valid, SESANS contrast variation spectra will not show any contrast dependence, and the coherent contribution in SANS spectra will be just scaled by the total scattering power. In this case SANS could provide the information such as average contrast based on the amplitude of $I(Q = 0)$ but SESANS is not sensitive here at all. Therefore, SESANS contrast variation technique should be used to investigate the change in the shape of the intra-molecular structure due to the variant contrast, which means $\Delta\rho(r, \eta)$ is dependent of r and Eq. (5.7) and (5.9) could not be valid.

Perhaps the simplest colloidal model, as shown in Figure 5.1(a), is the spherical particles with uniform density profile interacting via hard sphere potential. This so-called hard sphere model has been used to describe the structural features of many commonly encountered colloidal systems such as the micellar system of PMMA solutions [51]. In our calculation, the colloidal scattering length density is fixed at a constant value and the variation of the contrast between the colloid and the surrounding solvent is achieved by changing the H/D ratio of the solvent. Upon

increasing η , the corresponding SANS $I(Q)$ [Figure 5.1(b)] remains the qualitatively same shape as expected but exhibits a monotonic decrease in amplitude within the region of $2QR < 10$ and an increase when $2QR > 10$. From Eqs. (5.5), (5.7), and (5.9), this observed change of their magnitude is due to the decrease in the coherent scattering intensity $I_{coh}(Q)$ scaled down by a factor of square of $C(\eta)$, and the enhancing incoherent scattering contribution I_{inc} from the progressively increasing hydrogen introduced into the solvent, which also masks the features of $I_{coh}(Q)$ presenting in high- Q region. However, the corresponding SESANS $G(z)$ will remain invariant as shown in Figure 5.1(c). At this point, SESANS cannot pursue more information with the application of contrast variation on this homogeneous hard sphere system, as an example for the criterion of Eq. (5.7) and (5.9). The only difference among the various $G(z)$ corresponding to different η is reflected in the data statistics due to the variation of scattering power. Further discussion regarding the relationship between $G(z)$ and η is presented in Appendix B.

The calculated results presented in Figure 5.1 clearly show that the contrast variation SESANS technique is not sensitive to the variation of total scattering capability for any binary mixture system (solutes and solvent molecules) with uniformly distributed scattering length density in each phase. It is because of, as long as Eq. (5.7) (or equivalently Eq. (5.9)) is valid, that the shape of $\gamma(r)$ will remain unchanged as suggested by Eqs. (5.3) and (5.7), which results in the observed invariance of $G(z)$.

In the next two sections, several spatial correlation functions calculated from different representative colloidal models with various contrast are presented to illustrate the usefulness of contrast variation method in facilitating SANS and SESANS experiments for structural investigation.

5.1 Create a Contrast

The concept of spherical core particle surrounded by an outer concentric shell of another material with different scattering length density has been widely used as the model for many colloids such as grafted nanoparticle with silica core and polymeric out layer [35]. In this study, as shown in Figure 5.2, the core particle is

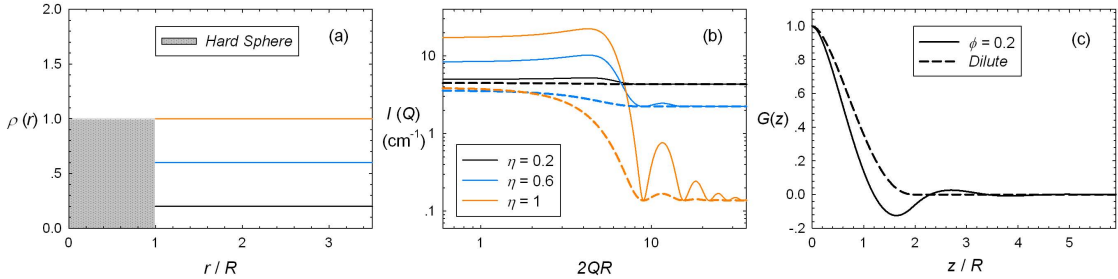


Figure 5.1: (a) The scattering length density profile for a homogeneous hard sphere particle. The scattering contrast is set to three different levels (orange, blue and black) by changing the H/D ratio of the surrounding solvent. (b) The calculated SANS $I(Q)$ at different levels of scattering contrast. The dash lines are the spectra for dilute solutions and the solid lines represent those for concentrated cases with a colloidal volume fraction of 0.2. (c) The corresponding SESANS correlation functions $G(z)$ are seen to be identical even though the absolute value of $\Delta\rho(r)$ changes significantly.

homogenous with a radius δ and a scattering length density 0 and 1 for the particle with (a) deuterated core and (b) deuterated shell, respectively, and the shell is homogeneous also with thickness $1 - \delta$ and a scattering length density 1 and 0 for (a) and (b), respectively. These two different composite particles are dispersed in a medium with three different levels of scattering length density given by the dotted, dashed, and solids line.

Unlike the invariance of $G(z)$ for particle with the homogeneous density profile given in Figure 5.1(c), Figures 5.3 and 5.4 clearly indicate that the contrast variation SESANS technique is capable of detecting the structural inhomogeneity reflected in the non-uniform intra-colloidal density profile given in Figure 5.2. It is true that the variation in the scattering contrast due to the uneven mass distribution is also manifested in the shift of characteristic peaks and bumps in the $I(Q)$ of contrast variation SANS experiments, as shown in panels (a) and (b) of Figures 5.3 and

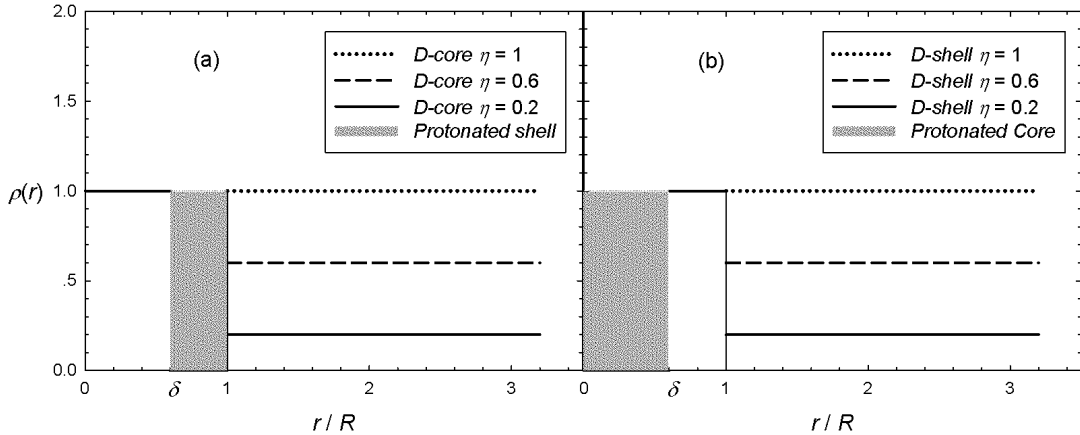


Figure 5.2: The scattering length density profile for a concentric sphere particle with (a) deuterated core and protonated shell and (b) protonated core and deuterated shell. The scattering contrast is set to three different levels (dotted, dashed, and solid lines) by changing the H/D ratio of the surrounding solvent.

5.4. However, in real SANS experiment these observed changes, especially for those presenting in the relatively high- Q region, are often smeared by the incoherent background which could compromise the quantitative structural determination. In SESANS, the structural variance will be reflected in the change of slope and shape in $G(z)$ within the region of the first two oscillations ($z/R < 3$) where SESANS has the best resolution in terms of data statistics.

Not only can the contrast variation SESANS technique reveal the intra-colloidal heterogeneity, our theoretical calculation suggests that it can also be applied to resolve the partial structure factor in a colloidal suspension in which part of the constituent particles are isotopically substituted. As shown in the middle panel of Figure 5.5, considering a colloidal system as a binary mixture of protonated particles and substituted ones whose scattering length density is set to be identical to that of solvent, the corresponding SESANS spectra can be conveniently calculated based on our previous derivation of $G_{ij,excl}(z)$ and $G_{ij,struct}(z)$ with $i, j = 1, 2$ as the cross

correlation between any two given components, given the fact that the inter-colloidal interaction can be described by hard-sphere interaction. If one defines the relative ratio for the number density of each component as following:

$$\begin{aligned} x_1 &= \frac{n_1}{n_1 + n_2} \\ x_2 &= \frac{n_2}{n_1 + n_2}, \end{aligned} \quad (5.10)$$

If the volume fractions of each phase are ϕ_1 and ϕ_2 , the total scattering function in SESANS representation can be expressed as:

$$\begin{aligned} G(z) = & x_1 G_{1,auto}(z) + x_2 G_{2,auto}(z) \\ & - x_1 \phi_1 G_{11,excl}(z) - x_2 \phi_2 G_{22,excl}(z) - 2\sqrt{x_1 x_2 \phi_1 \phi_2} G_{12,excl}(z) \\ & + x_1 \phi_1 G_{11,struct}(z) + x_2 \phi_2 G_{22,struct}(z) + 2\sqrt{x_1 x_2 \phi_1 \phi_2} G_{12,struct}(z), \end{aligned} \quad (5.11)$$

As indicated by Eq. (5.11), $G(z)$ is proportional to the square of the scattering length density contrast, therefore only the contribution from the protonated colloids exists. The contribution from the deuterated particles, which matches the solvent scattering length density in our calculation, as well as the cross correlation, will be eliminated according to the input parameters in our calculation.

The predicted SANS $I(Q)$, calculated from the method proposed by Kinoshita, and the SESANS $G(z)$, are presented in Figure 5.6. It is instructive to discuss the comparison between the partial SESANS correlation functions for the protonated colloids in Figure 5.5(b) (dashed line) and the $G(z)$ for the case of Figure 5.5(c) (dotted line). In our previous report, we have identified the strengthened local ordering due to an additional short-range inter-colloidal attraction which is reflected in the increase in magnitude of $G(z)$ within the range of correlation lengths around $1 < z/R < 3$. It is therefore clear that in the case of Figure 5.6(b), the short-range correlation of the protonated particles is enhanced by the depletion effect due to the

presence of their deuterated counterparts, in comparison to the $G(z)$ of hard sphere reference system (Figure 5.5(c)) with same colloidal volume fraction of 0.2. The same conclusion can also be drawn from the comparison of various $I(Q)$ presented in Figure 5.6(a).

5.2 Sensitivity to the Geometric Shape

It is worth comparing our theoretical results with the existing experimental SANS work of colloidal systems with non-uniform intra-colloidal density profiles. There have been several SANS studies on different species of icosahedral viruses to understand the organized viral structures in aqueous solutions and their structural evolution as a function of thermodynamic parameters [67, 68, 69]. As an example, we create the scattering length density profiles of icosahedral virus based on the multi-layer spherical shell architecture proposed by He and coworkers in their recent experimental work [69]. As shown in Figure 5.7, two different global geometric shapes, sphere [Figure 5.7(a)] and icosahedron [Figure 5.7(b)] are used with the isovolumic constraint to calculate the scattering functions at two different levels of scattering contrast (dashed ($\eta = 1$) and solid ($\eta = 0.6$) lines).

The form factor $P(Q)$ of multi-layer shell colloid can be expressed as

$$P(Q) = \left\{ \frac{\sum_i F_i(Q) V_i}{\sum_i V_i} \right\}^2, \quad (5.12)$$

where $F_i(Q)$ is the scattering amplitude for each shell layer and V_i the corresponding volume. The scattering amplitude $F(Q)$ for icosahedron has been presented in our previous work and also listed in Appendix E. The SESANS correlation function $G(z)$ is the Hankel transform of the SANS spectrum $I(Q)$. Therefore, the corresponding autocorrelation function can be calculated using

$$G(z) = \frac{1}{2\pi\xi} \int_0^\infty J_0(zQ) I(Q) Q dQ, \quad (5.13)$$

where $J_0(zQ)$ is the zeroth-order Bessel function. The SANS $I(Q)$ calculated from spherical model (red lines) and icosahedral model (black lines) are given in Figure

5.8(a) as a function of η . Despite the apparent difference in the global geometric appearance, viruses with icosahedral symmetry have been described as particles with spherical symmetry in SANS data analysis [67, 68, 69]. As pointed out in our previous theoretical study, the difference of $I(Q)$ between the spherical and icosahedral models is reflected in the subtle disagreements of the maxima and minima presented in the high- Q region (dashed lines), which can be easily smeared out by the instrumental resolution effect. Moreover, upon increasing the number of hydrogens in the solvent (namely reducing η), this difference is no longer distinguishable due to the enhancing incoherent background (solid lines). However, the calculated SESANS correlation functions [Figure 5.8(b)] corresponding to the spherical shell model (black line) and the icosahedral one (red line) exhibit considerable difference upon changing η . This observation proves the usefulness of contrast variation SESANS technique in revealing the structural details which are masked by the Fourier transform procedure of the spatial correlation occurring in the event of conventional elastic neutron scattering.

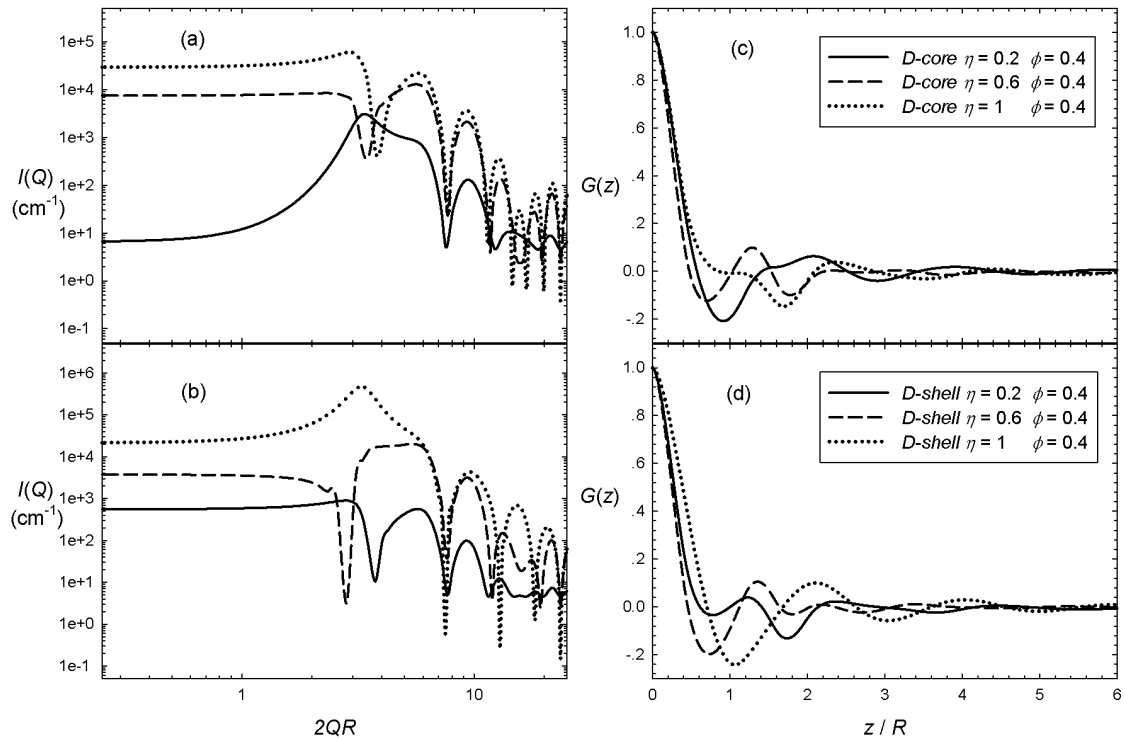


Figure 5.3: The SANS $I(Q)$ (a) and SESANS $G(z)$ (c) calculated from the model of core-shell particle with a deuterated core and the SANS $I(Q)$ (b) and SESANS $G(z)$ (d) corresponding to the particle with deuterated shell. The colloidal volume fraction ϕ and the core radius δ in this calculation are set to be 0.4 and 0.6 respectively. The dotted, dashed, and solid lines correspond to the $I(Q)$ and $G(z)$ with the three different levels of scattering length density given in Figure 5.2.

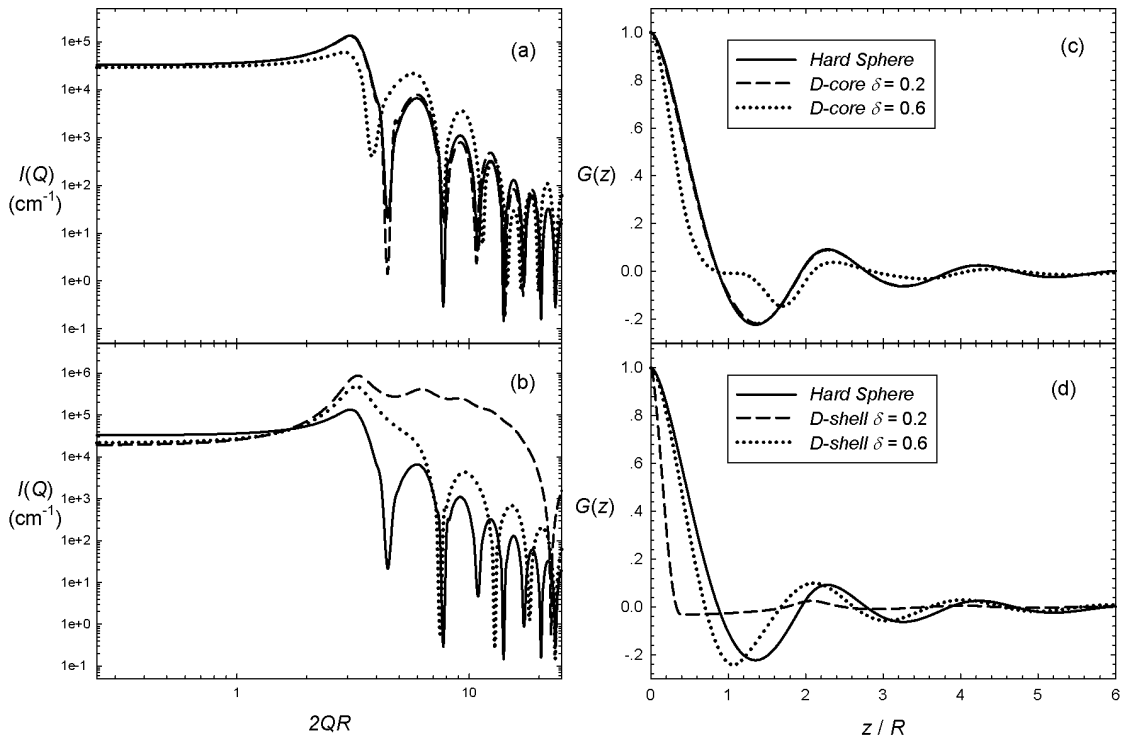


Figure 5.4: The SANS $I(Q)$ (a) and SESANS $G(z)$ (c) calculated from the model of core-shell particle with deuterated core and the SANS $I(Q)$ (b) and SESANS $G(z)$ (d) corresponding to the particle with deuterated shell. The colloidal volume fraction ϕ and η in this calculation are set to be 0.4 and 1 respectively. The dotted, dashed, and solid lines are corresponding to the $I(Q)$ and $G(z)$ with the three different levels of scattering length density given in Figure 5.2.

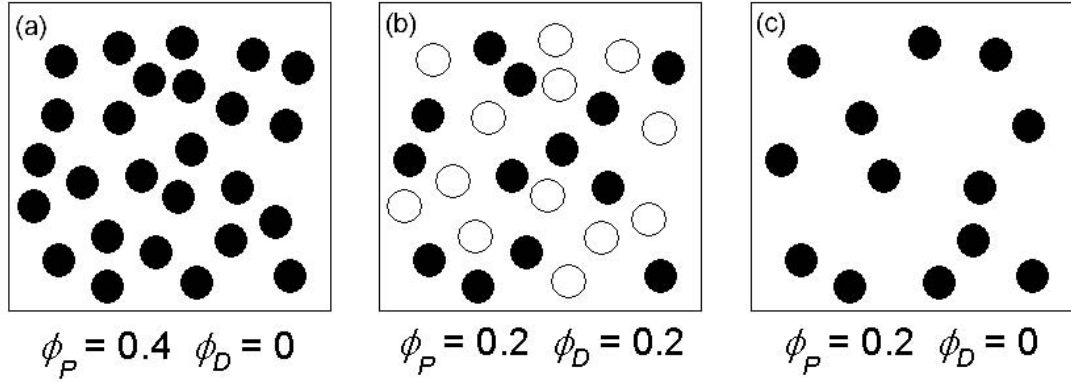


Figure 5.5: The schematic representation of a colloidal suspension consisting of (a) protonated particles with a volume fraction of 0.4 and deuterated solvent; (b) protonated particles with volume fraction of 0.2, deuterated particles whose scattering length density matches that of the solvent with a volume fraction of 0.2, and deuterated solvent; (c) protonated particles with volume fraction of 0.2 and deuterated solvent.

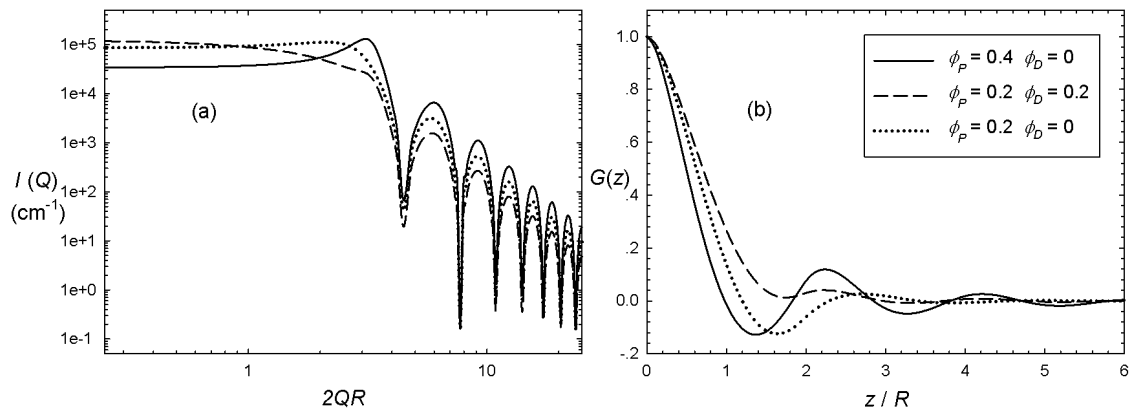


Figure 5.6: The SANS $I(Q)$ and SESANS $G(z)$ calculated from the models of colloidal suspensions presented in Figure 5.5.

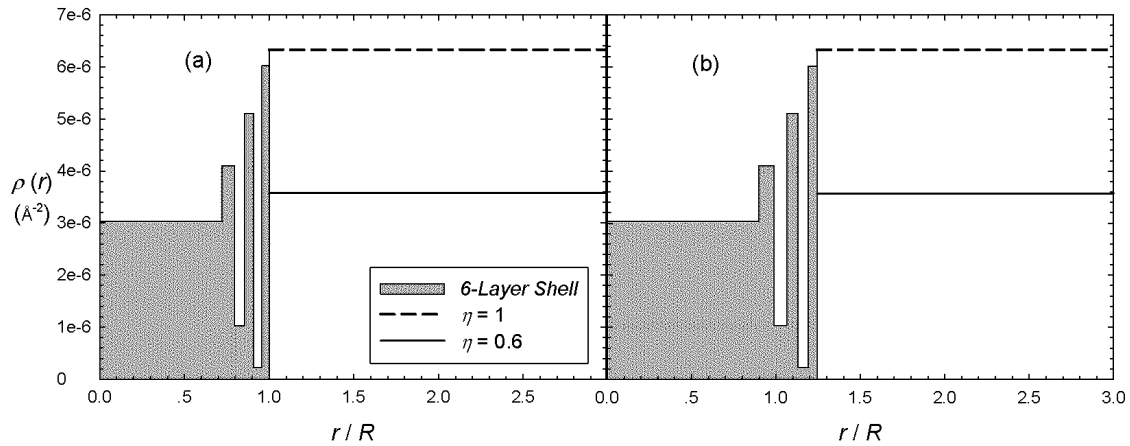


Figure 5.7: The theoretical model for the density profile of a multi-layered virus. The variation of the scattering length density along the radial direction is based on the organized intra-viral structure revealed by a SANS experiment by He and coworkers using a multi-layer spherical shell model, as shown in panel (a). Panel (b) gives the icosahedral counterpart with the isovolumic constraint.

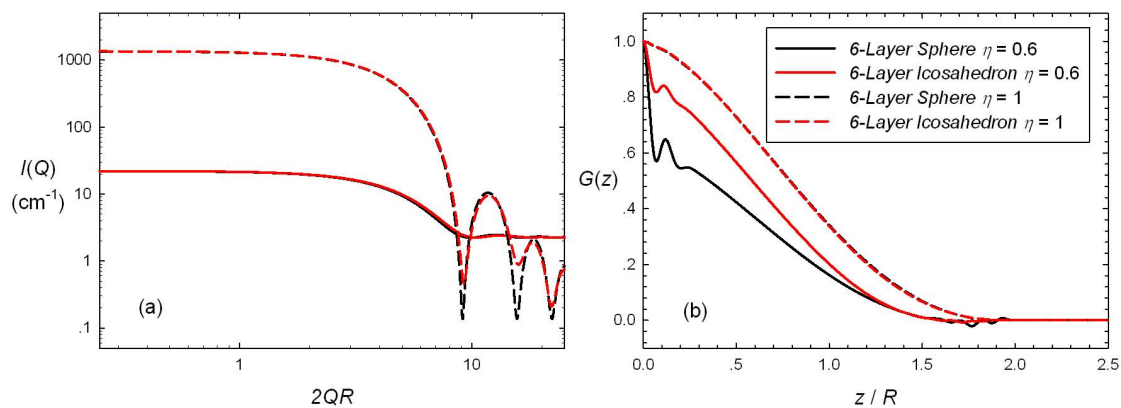


Figure 5.8: The SANS $I(Q)$ and SESANS $G(z)$ calculated from the viral model shown in Figure 5.7.

LITERATURE CITED

- [1] G. Kostorz, *Neutron Scattering, Treatise on Materials Science and Technology*, Vol. 15, Academic, New York, 1979.
- [2] P. Linder and Th. Zemb, *Neutron, X-rays and Light: Scattering Methods Applied to Soft Condensed Matter*, North-Holland, Amsterdam, 2002.
- [3] R. Borsali and R. Pecora, *Soft-Matter Characterization*, Springer, Berlin, 2008.
- [4] R. Pynn, in *Neutron Spin Echo*, edited by F. Mezei, Springer-Verlag, Berlin, 1980.
- [5] M. T. Rekveldt, “Novel SANS instrument using Neutron Spin Echo”, *Nucl. Instr. and Meth.in Phys. Res. B*, Vol. 114, 1996, pp. 366-370.
- [6] L. Van Hove, “Correlations in Space and Time and Born Approximation Scattering in Systems of Interacting Particles”, *Phys. Rev.*, Vol. 95, 1954, pp. 249-262.
- [7] P. Debye and A. M. Bueche, “Scattering by an Inhomogeneous Solid”, *J. Appl. Phys.*, Vol. 20, 1949, pp. 518-525.
- [8] R. Bracewell, *The Fourier Transform and Its Applications*, 3rd ed. McGraw-Hill Science/Engineering/Math, New York, 1999.
- [9] F. Mezei, “Neutron Spin Echo: A New Concept in Polarized Thermal Neutron Techniques”, *Z. Physik*, Vol. 255, 1972, pp. 146-160.
- [10] R. A. Andersson, L. F. van Heijkamp, I. M. de Schepper, and W. G. Bouwman, “Analysis of spin-echo small-angle neutron scattering measurements”, *J. Appl. Cryst.*, Vol. 41, 2008, pp. 868-885.
- [11] W. B. Russel, D. A. Saville, and W. R. Schowalter, *Colloidal Dispersions*, Cambridge University Press, Cambridge, 1989.
- [12] J.-P. Hansen and I. R. McDonald, *Theory of Simple Liquids*, 3rd ed. Elsevier, Amsterdam, 2006.
- [13] J.-P. Hansen, D. Levesque, and J. Zinn-Justin, *Liquids, Freezing and Glass Transition, Les Houches 1989 Session LI*, North-Holland, Amsterdam, 1989.
- [14] G. Nägele, “On the dynamics and structure of charge-stabilized suspensions”, *Phys. Rep.*, Vol. 272, 1996, pp. 215-372.

- [15] W. Brown, *Light Scattering: Principle and Development*, Clarendon, Oxford, 1996.
- [16] T. Krouglov, W. G. Bouwman, J. Plomp, M. T. Rekveldt, G. J. Vroege, A. V. Petukhov, and D. M. E. Thies-Weesie, “Structural transitions of hard-sphere colloids studied by spin-echo small-angle neutron scattering”, *J. Appl. Cryst.*, Vol. 36, 2003, pp. 1417-1423.
- [17] O. Glatter, “Computation of Distance Distribution Functions and Scattering Functions of Models for Small Angle Scattering Experiments”, *Acta Phys. Austriaca*, Vol. 52, 1980, pp. 243-256.
- [18] T. Krouglov, “Correlation function of the excluded volume”, *J. Appl. Cryst.*, Vol. 38, 2005, pp. 716-720.
- [19] D. Chandler and H. C. Anderson, “Optimized Cluster Expansions for Classical Fluids. II. Theory of Molecular Liquids”, *J. Chem. Phys.*, Vol. 57, 1972, pp. 1930-1937.
- [20] M. Kotlarchyk and S.-H. Chen, “Analysis of small angle neutron scattering spectra from polydisperse interacting colloids”, *J. Chem. Phys.*, Vol. 79, 1983, pp. 2461-2469.
- [21] K. S. Schweizer and J. G. Curro, “PRISM theory of the structure, thermodynamics, and phase transitions of polymer liquids and alloys”, *Adv. Polym. Sci.*, Vol. 116, 1994, pp. 319-377.
- [22] F. Rogers and D. Young, “New, thermodynamically consistent, integral equation for simple fluids”, *Phys. Rev. A*, Vol. 30, 1984, pp. 999-1007.
- [23] M. Laurati, J. Stellbrink, R. Lund, L. Willner, E. Zaccarelli, and D. Richter, “Asymmetric poly(ethylene-alt-propylene)-poly(ethylene oxide) micelles: A system with starlike morphology and interactions”, *Phys. Rev. E*, Vol. 76, 041503, 2007, pp. 1-14.
- [24] W.-R. Chen, F. Mallamace, and S.-H. Chen, “Small-angle neutron scattering study of the temperature-dependent attractive interaction in dense L64 copolymer micellar solutions and its relation to kinetic glass transition”, *Phys. Rev. E*, Vol. 66, 021403, 2002, pp. 1-12.
- [25] S. V. G. Menon, C. Manohar, and K. S. Rao, “A new interpretation of the sticky hard sphere model”, *J. Chem. Phys.*, Vol. 95, 1991, pp. 9186-9190.
- [26] P. Linse, “Accurate solution of a highly asymmetric electrolyte: Molecular dynamics simulation and integral equation”, *J. Chem. Phys.*, Vol. 93, 1990, pp. 1376-1385.

- [27] K. S. Schmitz, *Macroions in Solution and Colloidal Suspension*, VCH, New York, 1993.
- [28] J. Mahanty and B. W. Ninham, *Dispersion Force*, Academic, London, 1976.
- [29] A. Guinier and G. Fournet, *Small-Angle Scattering of X-rays*, Wiley, New York, 1955.
- [30] R. Roth and M. Kinoshita, “Depletion potential between large spheres immersed in a multicomponent mixture of small spheres”, *J. Chem. Phys.*, Vol. 125, 084910, 2006, pp. 1-6.
- [31] J. Lebowitz, “Exact Solution of Generalized Percus-Yevick Equation for a Mixture of Hard Spheres”, *Phys. Rev.*, Vol. 133, 1964, pp. A895-A899.
- [32] N. Ashcroft and D. Langreth, “Structure of Binary Liquid Mixtures. I”, *Phys. Rev.*, Vol. 156, 1967, pp. 685-692.
- [33] A. Vrij, “Mixtures of hard spheres in the Percus-Yevick approximation. Light scattering at finite angles”, *J. Chem. Phys.*, Vol. 71, 1979, pp. 3267-3270.
- [34] O. Uca, W. G. Bouwman, and M. T. Rekveldt, “Model calculations for the spin-echo small-angle neutron-scattering correlation function”, *J. Appl. Cryst.*, Vol. 36, 2003, pp. 109-116.
- [35] R. H. Ottewill and R. A. Richardson, “Studies of particle-particle interactions using polystyrene latices and time-average light scattering”, *Colloid Polym. Sci.*, Vol. 260, 1982, pp. 708-719.
- [36] M. O. Robbins, K. Kremer, and G. S. Grest, “Phase diagram and dynamics of Yukawa systems”, *J. Chem. Phys.*, Vol. 88, 1988, pp. 3286-3312.
- [37] H. Löwen, J.-N. Roux, and J.-P. Hansen, “Mapping of charge polydispersity onto size polydispersity in colloidal suspensions”, *J. Phys.: Condens. Matter*, Vol. 3, 1991, pp. 997-1002.
- [38] R. Borsali and R. Pecora, *Structure and Dynamics of Polymer and Colloidal Systems*, Kluwer, Dordrecht, 1999.
- [39] J. S. Pedersen, “Small-angle scattering from precipitates: Analysis by use of a polydisperse hard-sphere model”, *Phys. Rev. B*, Vol. 47, 1993, pp. 657-665.
- [40] E.-W. Huang, P. K. Liaw, L. Porcar, Y. Liu, Y.-L. Liu, J.-J. Kai, and W.-R. Chen, “Study of nanoprecipitates in a nickel-based superalloy using small-angle neutron scattering and transmission electron microscopy”, *Appl. Phys. Lett.*, Vol. 93, 161904, 2008, pp. 1-3.

- [41] D. Astruc, E. Boisselier, and C. Ornelas, “Dendrimers Designed for Functions: From Physical, Photophysical, and Supramolecular Properties to Applications in Sensing, Catalysis, Molecular Electronics, Photonics, and Nanomedicine”, *Chem. Rev.*, Vol. 110, 2010, pp. 1857-1959.
- [42] S. Svenson, *Carrier-Based Drug Delivery*, American Chemical Society, Washington, DC, 2004.
- [43] M. Ballauff and C. N. Likos, “Dendrimers in Solution: Insight from Theory and Simulation”, *Angew. Chem. Int. Ed.*, Vol. 43, 2004, pp. 2998-3020.
- [44] C. N. Likos, “Soft matter with soft particles”, *Soft Matter*, Vol. 2, 2006, pp. 478-498.
- [45] I. Prigogine and S. A. Rice, *Polymer Systems: Advances in Chemical Physics*, Vol. XCIV, Wiley, New York, 1996.
- [46] T. A. Witten and P. A. Pincus, *Structured Fluids: Polymers, Colloids, Surfactants*, Oxford University Press, Oxford, 2004.
- [47] R. A. Jones, *Soft Condensed Matter*, Oxford University Press, Oxford, 2002.
- [48] T. Krouglov, *Spin-Echo Small-Angle Neutron Scattering Applied to Colloidal Systems*, IOS Press, Delft, 2005.
- [49] C. N. Likos, S. Rosenfeldt, N. Dingenouts, M. Ballauff, P. Linder, N. Werner, and F. Vögtle, “Gaussian effective interaction between flexible dendrimers of fourth generation: A theoretical and experimental study”, *J. Chem. Phys.*, Vol. 117, 2002, pp. 1869-1877.
- [50] O. Glatter and O. Kratky, *Small-Angle X-ray Scattering*, Academic, London, 1982.
- [51] S.-H. Chen, “SMALL ANGLE NEUTRON SCATTERING STUDIES OF THE STRUCTURE AND INTERACTION IN MICELLAR AND MICROEMULSION SYSTEMS”, *Annu. Rev. Phys. Chem.*, Vol. 37, 1986, pp. 351-399.
- [52] L. A. Fergin and D. I. Svergun, *Structure Analysis by Small-Angle X-ray and Neutron Scattering*, Plenum, New York, 1987.
- [53] H. Brumberger, *Modern Aspects of Small-Angle Scattering*, Kluwer, Dordrecht, 2010.
- [54] J. Gapinski, A. Wilk, A. Patkowski, W. Häußler, A. J. Banchio, R. Pecore, and G. Nägele, “Diffusion and microstructural properties of solutions of charged nanosized proteins: Experiment versus theory”, *J. Chem. Phys.*, Vol. 123, 054708, 2005, pp. 1-13.

- [55] H. T. Jung, B. Coldren, J. A. Zasadzinski, D. J. Iampietro, and E. W. Kaler, “The origins of stability of spontaneous vesicles”, *Proc. Natl. Acad. Sci. U. S. A.*, Vol. 98, 2001, pp. 1353-1357.
- [56] Chwen-Yang Shew and Wei-Ren Chen, “*Structural sensitivity of SESANS for high-density hard sphere liquids*” (unfinished).
- [57] C. N. Likos, H. Löwen, M. Watzlawek, B. Abbas, O. Jucknischke, J. Allgaier, and D. Richter, “Star Polymers Viewed as Ultrasoft Colloidal Particles”, *Phys. Rev. Lett.*, Vol. 80, 1998, pp. 4450-4453.
- [58] T. Hashimoto, A. Todo, H. Itoi, and H. Kawai, “Domain-Boundary Structure of Styrene-Isoprene Block Copolymer Films Cast from Solutions. 2. Quantitative Estimation of the Interfacial Thickness of Lamellar Microphase Systems”, *Macromolecules*, Vol. 10, 1977, pp. 377-384.
- [59] M. Gradzielski, D. Langvin, L. Magid, and R. Strey, “Small-Angle Neutron Scattering from Diffuse Interfaces. 2. Polydisperse Shells in Water-*n*-Alkane- $C_{10}E_4$ Microemulsions”, *J. Phys. Chem.*, Vol. 99, 1995, pp. 13232-13238.
- [60] Y. C. Liu, S.-H. Chen, and J. S. Huang, “Small-Angle Neutron Scattering Analysis of the Structure and Interaction of Triblock Copolymer Micelles in Aqueous Solution”, *Macromolecules*, Vol. 31, 1998, pp. 2236-2244.
- [61] J. S. Pedersen, “Structure factors effects in small-angle scattering from block copolymer micelles and star polymers”, *J. Chem. Phys.*, Vol. 114, 2001, pp. 2839-2846.
- [62] S. Rathgeber, M. Monkenbusch, M. Kreitschmann, V. Urban, and A. Brulet, “Dynamics of star-burst dendrimers in solution in relation to their structural properties”, *J. Chem. Phys.*, Vol. 117, 2002, pp. 4047-4062.
- [63] W. D. Dozier, J. S. Huang, and L. J. Fetters, “Colloidal Nature of Star Polymer Dilute and Semidilute Solutions”, *Macromolecules*, Vol. 24, 1991, pp. 2810-2814.
- [64] L. Willner, O. Jucknischke, D. Richter, B. Farago, L. J. Fetters, and J. S. Huang, “Ordering Phenomena of Star Polymers in Solution by SANS.”, *Europhys. Lett.*, Vol. 19, 1992, pp. 297-303.
- [65] D. E. Parks, M. S. Nelkin, J. R. Beyster, and N. F. Wikner, *Slow Neutron Scattering and Thermalization*, New York: W. A. Benjamin, Inc., 1970.
- [66] P. Linder and T. Zemb, *Neutron, X-ray and Light Scattering: Introduction to an Investigation Tool for Colloidal and Polymeric Systems*, Amsterdam: North-Holland, 1991.

- [67] M. A. Canady, H. Tsuruta, R. W. Hendrix, R. L. Duda, and J. E. Johnson, “Analysis of Rapid, Large-scale Protein Quaternary Structural Changes: Time-resolved X-ray Solution Scattering of *Nudaurelia capensis* ω Virus ($N\omega V$) Maturation”, *J. Mol. Biol.*, Vol. 311, 2001, pp. 803-814.
- [68] K. K. Lee, L. Gan, H. Tsuruta, R. W. Hendrix, R. L. Duda, and J. E. Johnson, “Evidence that a Local Refolding Event Triggers Maturation of HK97 Bacteriophage Capsid”, *J. Mol. Biol.*, Vol. 340, 2004, pp. 419-433.
- [69] L. He, A. Piper, F. Meilleur, D. A. A. Myles, R. Hernandez, D. T. Brown, and W. T. Heller, “The Structure of Sindbis Virus Produced from Vertebrate and Invertebrate Hosts as Determined by Small-Angle Neutron Scattering”, *J. Virol.*, Vol. 84, 2010, pp. 5270-5276.

APPENDIX A

Mathematical Transforms in SESANS

In scattering technology, Fourier transform is commonly applied, while the mathematical expression of SESANS is based on Abel transform. Here it is useful to have a brief summary about their connection.

The forward and backward Fourier transforms are expressed as follow:

$$\begin{aligned} F(k) &= \int_{-\infty}^{+\infty} \exp(ikx) f(x) dx \\ f(x) &= \frac{1}{2\pi} \int_{-\infty}^{+\infty} \exp(-ikx) F(k) dk. \end{aligned} \quad (\text{A.1})$$

In an n -dimensional space, we will have the transform relation as

$$\begin{aligned} F(\mathbf{k}) &= \int_{-\infty}^{+\infty} \exp(i\mathbf{k} \cdot \mathbf{x}) f(\mathbf{x}) d^n \mathbf{x} \\ f(\mathbf{x}) &= \frac{1}{(2\pi)^n} \int_{-\infty}^{+\infty} \exp(-i\mathbf{k} \cdot \mathbf{x}) F(\mathbf{k}) d^n \mathbf{k}, \end{aligned} \quad (\text{A.2})$$

where x and k are both n -dimensional vectors.

In our three dimensional space, when transferring to spherical or polar coordinates, Abel and its inverse transforms are also widely used. Assuming $f(r)$ drops to zero more quickly than $\frac{1}{r}$, one has

$$\begin{aligned} F(z) &= 2 \int_z^{\infty} \frac{f(r)r}{\sqrt{r^2 - z^2}} dr \\ f(r) &= -\frac{1}{\pi} \int_r^{\infty} F'(z) \frac{dz}{\sqrt{z^2 - r^2}}, \end{aligned} \quad (\text{A.3})$$

where $F'(z)$ is the first order derivative of $F(z)$.

The physical interpretation of Abel transform is that $F(z)$ is the projection of a spherically symmetric function $f(\mathbf{r})$ onto \hat{z} direction. Without the loss of generality,

considering the measurement implemented along the \hat{z} direction in reciprocal space,

$$F(\mathbf{k}) = \int \exp(i\mathbf{k} \cdot \mathbf{r}) f(r) d^3\mathbf{r}, \quad (\text{A.4})$$

where the projection direction \mathbf{k} will be put along $\theta = 0$ axis which is \hat{z} direction. The Fourier transform in Eq. (A.4) can be described in polar coordinates as

$$F(k) = F(\mathbf{k}) = \int_{r=0}^{\infty} \int_{\theta=0}^{2\pi} \exp(ikr \cos \theta) f(r, \theta) r dr d\theta, \quad (\text{A.5})$$

where θ is the angle between \mathbf{k} and \mathbf{r} vectors. In a system with the thermodynamic functions isotropically distributed, $f(r, \theta) \equiv f(r)$ is no longer dependent on θ and the integration over θ can be separately performed as

$$\langle \exp(i\mathbf{k} \cdot \mathbf{r}) \rangle = \int_0^{2\pi} \exp(ikr \cos \theta) d\theta = 2\pi J_0(kr), \quad (\text{A.6})$$

where the bracket means the spatial average and $J_0(kr)$ is the zero-order Bessel function. Then the Fourier transform is now written as

$$F(k) = 2\pi \int_0^{\infty} J_0(kr) f(r) r dr, \quad (\text{A.7})$$

which is the so-called zero-order Hankel transform.

APPENDIX B

Data Statistics in SESANS

The physical quantity directly measured in SESANS experiment is the depolarization $P(z)$. Its relation with SESANS correlation function $G(z)$ is found to be

$$P(z) = T_R^{1-G(z)}, \quad (\text{B.1})$$

where T_R is the transmission of the sample, which is strongly related to the solvent contrast and the sample concentration. Therefore, with the measured statistical error $\delta P(z)$, the error in SESANS spectrum $G(z)$ can be expressed as

$$\delta G(z) = -\frac{\delta P(z)}{P(z) \ln T_R}. \quad (\text{B.2})$$

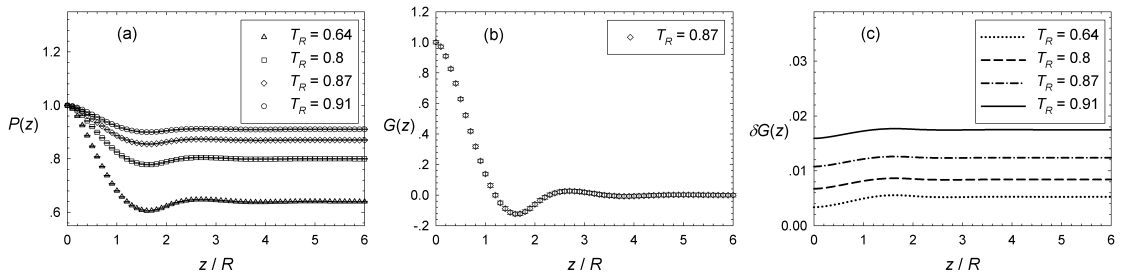


Figure B.1: SESANS spectra for a hard sphere system with different transmission values and the corresponding statistical error levels. (a) The measured depolarization $P(z)$ spectra with different transmission values. (b) The SESANS correlation function $G(z)$ which is exactly the same for different contrasts but with different errors. For the sake of simplicity, the case of $T_R = 0.87$ is only presented. (c) The statistical error level rises with the increase of sample transmission. Different symbols and line types are used for the corresponding transmission values, as shown in the legend.

From Figure B.1(b), we observe that $G(z)$ is invariant with regard to different transmission values. However, it is obvious that $P(z)$ changes with transmission [Figure B.1(a)]. This change of $P(z)$ leads the error in SESANS spectrum, $\delta G(z)$, to change in accord with transmission [Figure B.1(c)]. The statistical error of the depolarization $\delta P(z)$ is set with 0.0015 and with the transmission around 0.9, the error in SESANS spectrum $\delta G(z)$ is around 0.015, ten times larger than $\delta P(z)$. Since the molar ratio of deuterated solvent, η , is directly related with the scattering power (transmission), the various $G(z)$ corresponding to different η will only show different statistics due to different $\delta G(z)$.

APPENDIX C

SESANS Correlation Function for Dumbbell

From theoretical aspect, in a many-particle system, any two particles can be viewed as a single dumbbell. The Debye correlation function $\gamma(r)$ for the binary colloidal mixture can therefore be derived accordingly in an analytical manner. When the inter-particle distance $a \geq (R_1 + R_2)$, where R_1 and R_2 are the radii of particles 1 (large hard sphere) and 2 (small hard sphere), $\gamma(r)$ takes the following expression:

$$\gamma(r, a) = \frac{p(r)}{r^2} \left(\frac{1}{V_1} + \frac{1}{V_2} \right), \quad (\text{C.1})$$

where $p(r)$ is the pair distance distribution function (PDDF) for dumbbells with two hard spheres separated by a distance a whose mathematical expressions are known [17]. $V_1 = \frac{4\pi}{3}R_1^3$ and $V_2 = \frac{4\pi}{3}R_2^3$ are the volumes of the large hard spheres and the small ones respectively.

The SESANS correlation function for the excluded volume and the structure correlation function are the Abel transformation of the corresponding Debye correlation functions.

$$G_{excl,struct}(z) = \frac{2}{\xi} \int_z^\infty \frac{\gamma_{excl,struct}(r)r}{\sqrt{r^2 - z^2}} dr, \quad (\text{C.2})$$

and the Debye correlation functions are the integration of the correlation of the overlapped volume and the cross correlation in the corresponding region respectively. For spherical particles,

$$\begin{aligned} \gamma_{excl}(r) &= \int_0^{R_1+R_2} \gamma_{ovl}(r, a) 4\pi a^2 da \\ \gamma_{struct}(r) &= \int_{R_1+R_2}^\infty \gamma_{cross}(r, a) [g(a) - 1] 4\pi a^2 da. \end{aligned} \quad (\text{C.3})$$

During the numerical integration of Abel transformation, a singular point may be imported when r approaches z , so in order to avoid the error in numerical calcu-

lation, the sequence of integral could be exchanged as follows,

$$\begin{aligned}
G_{excl}(z) &= \int_0^{R_1+R_2} G_{ovl}(z, a) 4\pi a^2 da \\
&= \frac{2}{\xi} \int_0^{R_1+R_2} 4\pi a^2 da \int_z^\infty \frac{\gamma_{ovl}(r, a)r}{\sqrt{r^2 - z^2}} dr \\
G_{struct}(z) &= \int_{R_1+R_2}^\infty G_{cross}(z, a)[g(a) - 1] 4\pi a^2 da \\
&= \frac{2}{\xi} \int_{R_1+R_2}^\infty [g(a) - 1] 4\pi a^2 da \int_z^\infty \frac{\gamma_{cross}(r, a)r}{\sqrt{r^2 - z^2}} dr. \quad (\text{C.4})
\end{aligned}$$

The SESANS correlation function for the overlapped volume $G_{ovl}(z, a)$ and the cross correlation function $G_{cross}(z, a)$ take the following forms and are solved analytically,

I) $a = 0$:

$$\begin{aligned}
1) \quad 0 \leq r \leq R_2 - R_1 &\quad G_1(z) \\
2) \quad R_2 - R_1 \leq r \leq R_2 + R_1 &\quad G_2(z) \\
3) \quad R_2 + R_1 \leq r &\quad 0
\end{aligned} \quad (\text{C.5})$$

II) $(0 < a \leq R_1 \text{ and } R_1 \leq \frac{R_2}{2})$ or $(0 < a \leq R_2 - R_1 \text{ and } R_1 \geq \frac{R_2}{2})$:

$$\begin{aligned}
1) \quad 0 \leq r \leq (R_2 - R_1) - a &\quad G_1(z) \\
2) \quad (R_2 - R_1) - a \leq r \leq (R_2 - R_1) + a &\quad G_6(z) \\
3) \quad (R_2 - R_1) + a \leq r \leq (R_2 + R_1) - a &\quad G_{5ar}(z) \\
4) \quad (R_2 + R_1) - a \leq r \leq (R_2 + R_1) + a &\quad G_{3ar}(z) \\
5) \quad (R_2 + R_1) + a \leq r &\quad 0
\end{aligned} \quad (\text{C.6})$$

III) $R_1 \leq a \leq (R_2 - R_1) \text{ and } R_1 \leq \frac{R_2}{2}$:

$$\begin{aligned}
1) \quad 0 \leq r \leq (R_2 - R_1) - a &\quad G_1(z) \\
2) \quad (R_2 - R_1) - a \leq r \leq (R_2 + R_1) - a &\quad G_6(z) \\
3) \quad (R_2 + R_1) - a \leq r \leq (R_2 - R_1) + a &\quad G_4(z) \\
4) \quad (R_2 - R_1) + a \leq r \leq (R_2 + R_1) + a &\quad G_{3ar}(z) \\
5) \quad (R_2 + R_1) + a \leq r &\quad 0
\end{aligned} \quad (\text{C.7})$$

IV) $R_2 - R_1 \leq a \leq R_1$ and $R_1 \geq \frac{R_2}{2}$:

$$\begin{aligned}
 1) \quad & 0 \leq r \leq a & G_{5ra}(z) \\
 2) \quad & a \leq r \leq (R_2 - R_1) + a & G_{5ar}(z) \\
 3) \quad & (R_2 - R_1) + a \leq r \leq (R_2 + R_1) - a & G_{5ar}(z) \\
 4) \quad & (R_2 + R_1) - a \leq r \leq (R_2 + R_1) + a & G_{3ar}(z) \\
 5) \quad & (R_2 + R_1) + a \leq r & 0
 \end{aligned} \tag{C.8}$$

V) $(R_1 \leq a \leq R_2 \text{ and } R_1 \geq \frac{R_2}{2})$ or $(R_2 - R_1 \leq a \leq R_2 \text{ and } R_1 \leq \frac{R_2}{2})$:

$$\begin{aligned}
 1) \quad & 0 \leq r \leq a - (R_2 - R_1) & G_{5ra}(z) \\
 2) \quad & a - (R_2 - R_1) \leq r \leq (R_2 + R_1) - a & G_6(z) \\
 3) \quad & (R_2 + R_1) - a \leq r \leq (R_2 - R_1) + a & G_4(z) \\
 4) \quad & (R_2 - R_1) + a \leq r \leq (R_2 + R_1) + a & G_{3ar}(z) \\
 5) \quad & (R_2 + R_1) + a \leq r & 0
 \end{aligned} \tag{C.9}$$

VI) $R_2 \leq a \leq (R_2 + R_1)$:

$$\begin{aligned}
 1) \quad & 0 \leq r \leq (R_2 + R_1) - a & G_{5ra}(z) \\
 2) \quad & (R_2 + R_1) - a \leq r \leq a - (R_2 - R_1) & G_{3ra}(z) \\
 3) \quad & a - (R_2 - R_1) \leq r \leq a + (R_2 - R_1) & G_4(z) \\
 4) \quad & a + (R_2 - R_1) \leq r \leq a + (R_2 + R_1) & G_{3ar}(z) \\
 5) \quad & (R_2 + R_1) + a \leq r & 0
 \end{aligned} \tag{C.10}$$

VII) $(R_2 + R_1) \leq a$:

$$\begin{aligned}
 1) \quad & 0 \leq r \leq a - (R_2 + R_1) & 0 \\
 2) \quad & a - (R_2 + R_1) \leq r \leq a - (R_2 - R_1) & G_{3ra}(z) \\
 3) \quad & a - (R_2 - R_1) \leq r \leq a + (R_2 - R_1) & G_4(z) \\
 4) \quad & a + (R_2 - R_1) \leq r \leq a + (R_2 + R_1) & G_{3ar}(z) \\
 5) \quad & (R_2 + R_1) + a \leq r & 0,
 \end{aligned} \tag{C.11}$$

where

$$G_1(z) = \frac{4\pi}{3} R_1^3 T_1(z)$$

$$\begin{aligned} G_2(z) &= \frac{2\pi}{3}(R_1^3 + R_2^3)T_1(z) - \frac{\pi}{2}(R_1^2 + R_2^2)T_2(z) \\ &- \frac{\pi}{4}(R_1^2 - R_2^2)^2F_0(z, a) + \frac{\pi}{12}T_4(z) \end{aligned}$$

$$\begin{aligned} G_{3ra}(z) &= \frac{\pi}{2a}[\frac{1}{3}(R_1^3 + R_2^3)(R_1 + R_2)^2F_0(z, a) - \frac{1}{3}(R_1^3 + R_2^3)F_2(z, a) \\ &- \frac{1}{6}(R_1^2 + R_2^2)(R_1 + R_2)^3F_0(z, a) + \frac{1}{6}(R_1^2 + R_2^2)F_3(z, a) \\ &- \frac{1}{4}(R_1^2 - R_2^2)^2(R_1 + R_2)F_0(z, a) + \frac{1}{4}(R_1^2 - R_2^2)^2F_1(z, a) \\ &+ \frac{1}{60}(R_1 + R_2)^5F_0(z, a) - \frac{1}{60}F_5(z, a)] \end{aligned}$$

$$\begin{aligned} G_{3ar}(z) &= \frac{\pi}{2a}[\frac{1}{3}(R_1^3 + R_2^3)(R_1 + R_2)^2F_0(z, a) - \frac{1}{3}(R_1^3 + R_2^3)F_2(z, a) \\ &- \frac{1}{6}(R_1^2 + R_2^2)(R_1 + R_2)^3F_0(z, a) - \frac{1}{6}(R_1^2 + R_2^2)F_3(z, a) \\ &- \frac{1}{4}(R_1^2 - R_2^2)^2(R_1 + R_2)F_0(z, a) - \frac{1}{4}(R_1^2 - R_2^2)^2F_1(z, a) \\ &+ \frac{1}{60}(R_1 + R_2)^5F_0(z, a) + \frac{1}{60}F_5(z, a)] \end{aligned}$$

$$\begin{aligned} G_4(z) &= \frac{\pi}{2a}\{\frac{2}{3}R_1^3(R_2 - R_1)^2F_0(z, a) - \frac{2}{3}R_1^3F_2(z, a) \\ &+ \frac{4}{3}(R_1^3 + R_2^3)R_1R_2F_0(z, a) - \frac{1}{6}(R_1^2 + R_2^2)[(R_1 + R_2)^3 \\ &- (R_2 - R_1)^3]F_0(z, a) - \frac{1}{2}(R_1^2 - R_2^2)^2R_1F_0(z, a) \\ &+ \frac{1}{60}[(R_1 + R_2)^5 - (R_2 - R_1)^5]F_0(z, a)\} \end{aligned}$$

$$\begin{aligned} G_{5ra}(z) &= \frac{\pi}{2a}[\frac{4}{3}(R_1^3 + R_2^3)aT_1(z) + \frac{1}{6}(R_1^2 + R_2^2)F_3(z, -a) \\ &+ \frac{1}{6}(R_1^2 + R_2^2)F_3(z, a) + \frac{1}{4}(R_1^2 - R_2^2)^2F_1(z, -a) \\ &+ \frac{1}{4}(R_1^2 - R_2^2)^2F_1(z, a) - \frac{1}{60}F_1(z, -a) - \frac{1}{60}F_1(z, a)] \end{aligned}$$

$$\begin{aligned} G_{5ar}(z) &= \frac{\pi}{2a}[\frac{4}{3}(R_1^3 + R_2^3)aT_1(z) + \frac{1}{6}(R_1^2 + R_2^2)F_3(z, -a) \\ &- \frac{1}{6}(R_1^2 + R_2^2)F_3(z, a) + \frac{1}{4}(R_1^2 - R_2^2)^2F_1(z, -a) \end{aligned}$$

$$\begin{aligned}
& - \frac{1}{4}(R_1^2 - R_2^2)^2 F_1(z, a) - \frac{1}{60}F_1(z, -a) + \frac{1}{60}F_1(z, a)] \\
G_6(z) &= \frac{\pi}{2a}[\frac{2}{3}R_1^3(R_2 - R_1)^2 F_0(z, a) - \frac{2}{3}R_1^3 F_2(z, a) \\
&+ \frac{1}{6}(R_1^2 + R_2^2)F_3(z, -a) + \frac{1}{6}(R_1^2 + R_2^2)(R_2 - R_1)^3 F_0(z, a) \\
&+ \frac{1}{4}(R_1^2 - R_2^2)^2 F_1(z, -a) + \frac{1}{4}(R_1^2 - R_2^2)^2(R_2 - R_1)F_0(z, a) \\
&+ \frac{1}{60}F_5(z, -a) - \frac{1}{60}(R_2 - R_1)^5 F_0(z, a) \\
&+ \frac{1}{3}(R_1^3 + R_2^3)F_2(z, -a) - \frac{1}{3}(R_1^3 + R_2^3)(R_2 - R_1)^2 F_0(z, a)], \quad (\text{C.12})
\end{aligned}$$

where the integrations

$$T_n(z) = \int_{\alpha}^{\beta} \frac{r^n}{\sqrt{r^2 - z^2}} dr \quad (n = 1, 2, 4) \quad (\text{C.13})$$

$$F_n(z, a) = \int_{\alpha}^{\beta} \frac{(a - r)^n}{\sqrt{r^2 - z^2}} dr \quad (n = 0, 1, 2, 3, 5), \quad (\text{C.14})$$

are solved by substituting $r = z \sec \theta$. α and β are the lower and upper limits of the region where the specific $G_{ovl}(z, a)$ and $G_{cross}(z, a)$ are corresponding to.

Alternatively, $\gamma(r)$ can also be calculated numerically based on its definition of the two-point correlation of density fluctuations $\Delta\rho(\mathbf{r}) \equiv \rho(\mathbf{r}) - \langle \rho(\mathbf{r}) \rangle$.

$$\gamma(\mathbf{r}) = \frac{\int_V \Delta\rho(\mathbf{r}') \Delta\rho(\mathbf{r}' + \mathbf{r}) d^3\mathbf{r}'}{\int_V \Delta\rho(\mathbf{r}') \Delta\rho(\mathbf{r}') d^3\mathbf{r}'} \quad (\text{C.15})$$

It is straightforward to see that for an isotropic system, Eq. (C.15) can be further simplified by setting $\gamma(\mathbf{r}) = \gamma(r)$. The corresponding $G(z)$ and the hierarchical components obtained from the analytical expression (denoted by solid lines) and numerical solution (denoted by symbols), presented in Figure C.1, are in close agreement with each other. It is important to point out that, as found in nature, colloidal dispersions are in general polydisperse in size distribution, elongated, even flexible in shape. Given this increasing complexity, the analytical equation approach is unable to characterize such systems with sufficient accuracy in terms of tractable mathematics. The advantage of the numerical approach is reflected in its capability of bypassing the inherent limitation of analytical method and render an alternative

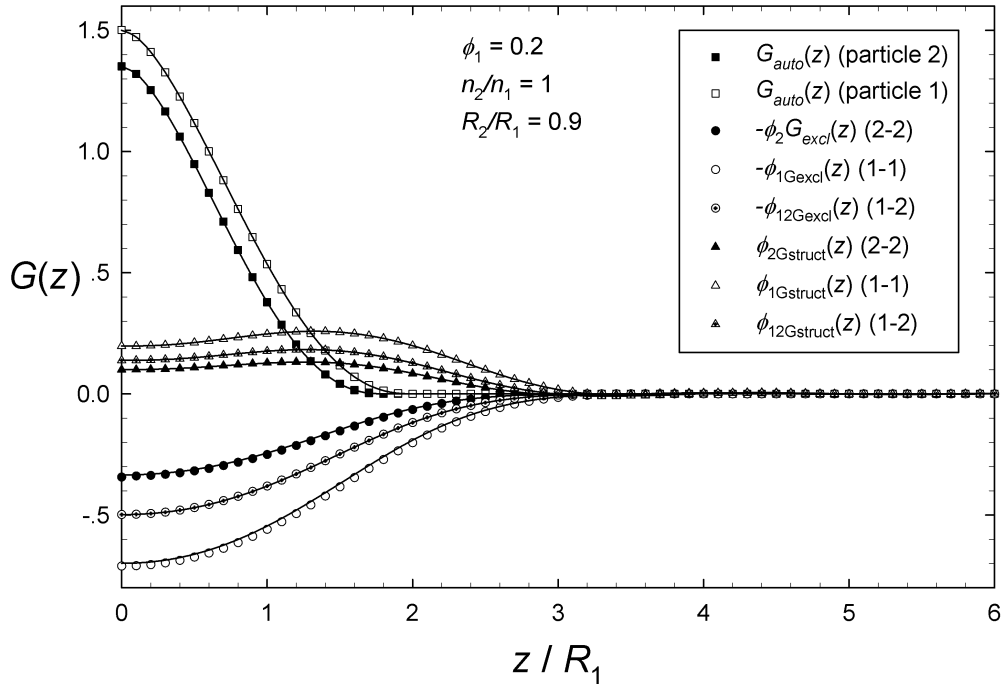


Figure C.1: Numerically and analytically calculated $G(z)$ of a binary mixture system. The symbols of square (autocorrelation function), circle (the correlation function of excluded volume) and triangle (structure correlation function) represent the numerical solutions, while the solid lines are the analytically calculated results. For the sake of clarity, the ratio of number density n_2/n_1 is set to be 1 and the size ratio $R_2/R_1 = 0.9$. ϕ_1 is kept at fixed value of 0.2. For the contribution from the interaction between particles, 1 – 1 denotes the interaction among the large particles, 2 – 2 the interaction within the small ones, and 1 – 2 the interaction between the large and small ones with the effective volume fraction $\phi_{12} = \sqrt{\phi_1\phi_2}$. This agreement promises the prospect of numerically calculating the $G(z)$ corresponding to the mathematically intractable complex systems such as concentrated colloidal suspensions consisting of particle with non-uniform density profile and irregular shape.

but equally accurate way for structural characterization for any general system with the minimum amount of extra approximations.

APPENDIX D

SESANS Correlation Function for Soft Colloid

The purpose of this appendix is to derive the direct expression of the Debye correlation function for interacting permeable soft spheres, which provides the mathematical foundation for calculating the corresponding SESANS correlation function and SANS coherent scattering cross section via Abel and Fourier transformations respectively.

Transformation of variables is first made to bypass the singularity at $r = z$ in the integrand of Eq. (2.14):

$$r = z \sec \beta. \quad (\text{D.1})$$

Substituting Eq. (D.1) into Eq. (2.14), $G(z)$ becomes

$$G(z) = \frac{2}{\xi} \int_0^{\frac{\pi}{2}} \gamma(z \cos \beta) \sec^2 \beta \, d\beta. \quad (\text{D.2})$$

It is not possible to derive the equivalent analytical expression of Eq. (D.2) for any given soft colloid due to the following reason: Figure D.2(a) gives the two dimensional projection of the spatial correlation of two overlapping spheres. For the case of uniform spheres with homogeneous mass distribution, the scattering length density ρ is a constant value within the intersection region and therefore the $\gamma_{cross}(r, a)$ in the integrand of Eq. (4.1) can be solved analytically. However, for the soft colloidal with a density profile $\rho(r)$ which is radially dependent, analytic derivation of the γ_{cross} term is no longer tractable mathematically. Instead, in this study the soft colloidal $G(z)$ is obtained numerically based on the previously developed method in Appendix C.

The geometric relations among the spatial variables of x , y , z , a , r_1 and r_2 required for the evaluation of $\gamma(r)$ are specified in Figure D.2(a): a is the distance between the centers of two spheres. r_1 and r_2 respectively represent the radii of the two spheres. θ is the angle between the unit vector \mathbf{r}_1 and \mathbf{r}_2 according to Figure

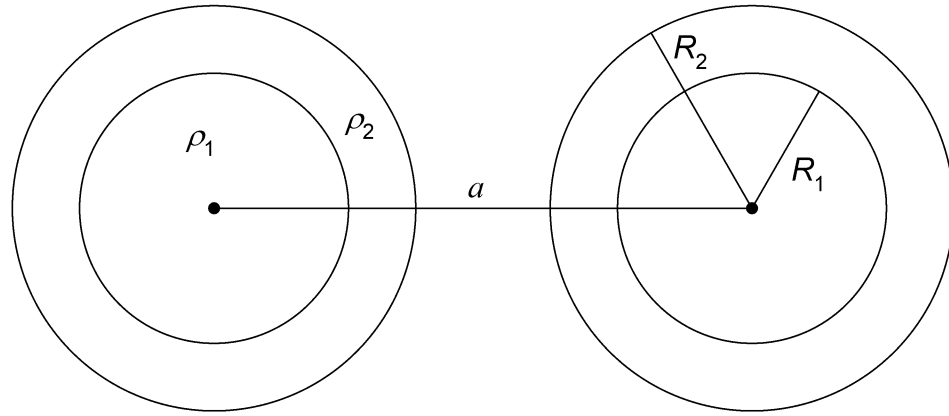


Figure D.1: Schematic representation of two spherical core particles with radius R_1 and scattering length density ρ_1 , surrounded by an outer concentric shell of another material characterized by R_2 and ρ_2 . The particle-particle distance used in our calculation of the corresponding Debye correlation function is given by a .

D.2(b), which gives an enlarged view of the circled area in Figure D.2(a). When $|r_1 - r_2| < a < r_1 + r_2$, converting from Cartesian to polar coordinates requires

$$\begin{aligned} x^2 + z^2 &= r_1^2 \\ y^2 + z^2 &= r_2^2 \\ x + y &= a \\ \cos \theta &= \frac{1}{2r_1 r_2} (r_1^2 + r_2^2 - a^2). \end{aligned} \tag{D.3}$$

One can express x , y , z , as a function of a , r_1 and r_2 after a few simple manipulations:

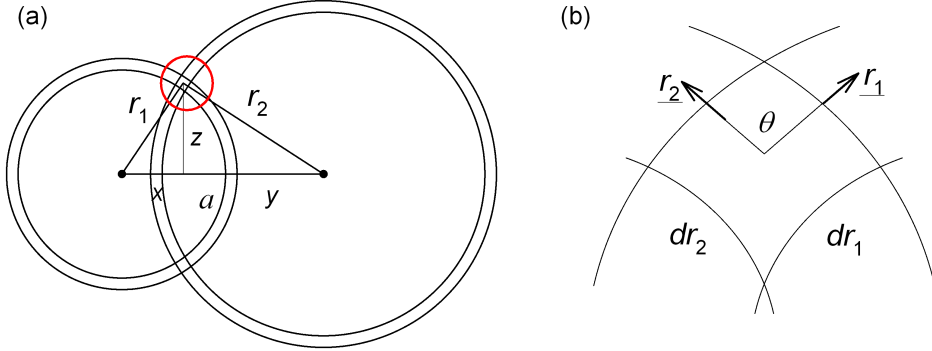


Figure D.2: (a) Two dimensional projection of the spatial correlation of two overlapping spheres. The geometric relations among the spatial variables of x , y , z , a , r_1 and r_2 required for the evaluation of $\gamma(r)$ of the spherical systems in this study. (b) The enlarged view of the red circled area in panel (a). θ is used to define the angle between r_1 and r_2 .

$$\begin{aligned} x &= \frac{a}{2} + \frac{1}{2a} (r_1^2 - r_2^2) \\ y &= \frac{a}{2} - \frac{1}{2a} (r_1^2 - r_2^2) \\ z &= \frac{1}{2a} (-r_1^4 - r_2^4 - a^4 + 2a^2r_1^2 + 2a^2r_2^2 + 2r_1^2r_2^2)^{1/2}. \end{aligned} \quad (\text{D.4})$$

To facilitate the calculation, we define the following functional of $\rho(r)$ which is the double derivative of $\gamma(r)$ with respect to the dummy variables r_1 and r_2

$$\begin{aligned} F[r_1, r_2, a, \rho(r)] &\equiv \frac{d^2\gamma(r)}{dr_1 dr_2} \\ &= \begin{cases} 2\pi z \rho(r_1) \rho(r_2) / \sin \theta & \text{when } |r_1 - r_2| < a < r_1 + r_2 \\ 0 & \text{otherwise} \end{cases} . \end{aligned}$$

r_1 and r_2 are bounded by the colloidal size. Based on the definition of self

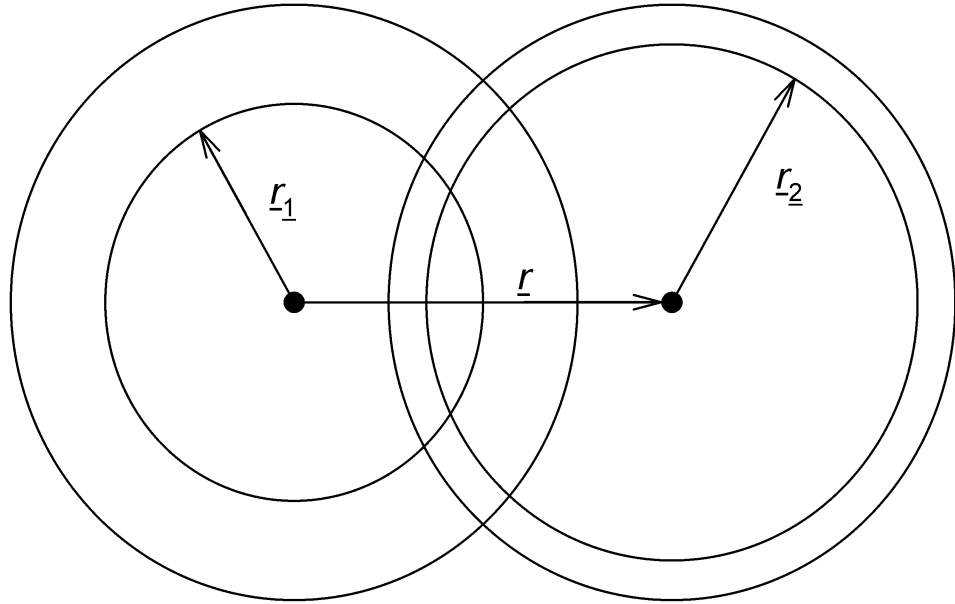


Figure D.3: Visualization of self correlation a sphere: $\gamma_{auto}(\mathbf{r})$ is determined by the overlapping volume between the referential sphere (the left one) and its virtual one (the right one) separate by \mathbf{r} .

correlation given in Eq. (3.4), $\gamma_{auto}(\mathbf{r})$ of a sphere can be evaluated by computing the overlapping volume between the referential sphere and its virtual one separate by \mathbf{r} . For the isotropic system, $\gamma_{auto}(\mathbf{r})$ can be simplified as $\gamma_{auto}(r)$, regardless the detailed intracolloidal mass distribution. Based on the visualization of this concept given in Figure D.3, $\gamma_{auto}(r)$ can be expressed in terms of $F[r_1, r_2, a, \rho(r)]$ as following

$$\gamma_{auto}(r) = \int_0^\sigma dr_1 \int_0^\sigma dr_2 F[r_1, r_2, r, \rho(r)], \quad (\text{D.5})$$

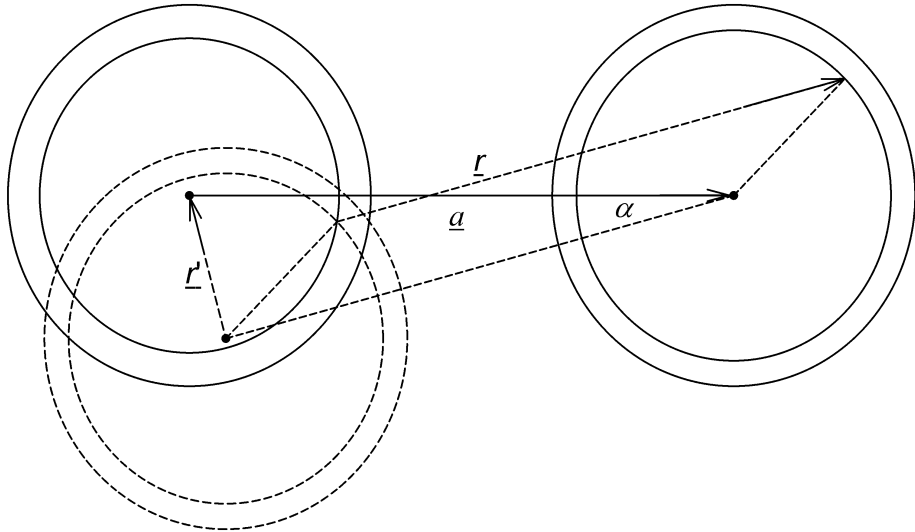


Figure D.4: Schematic representation regarding the determination of cross correlation in this study: $\gamma_{cross}(r)$ is calculated by the intersection volume of a second sphere (circle of solid lines on the left) with the virtual one (circle of dashed lines on the left) corresponding to the first referential sphere [16, 48] (circle of solid lines on the right).

where σ is the cutoff molecular boundary which can be specified based on different definitions suitable for different systems [23, 60].

Moreover, it was first shown by Kruglov that the γ_{cross} of the two spheres can be alternatively determined by the intersection volume of a second sphere with the virtual one corresponding to the first referential sphere. According to the geometric relations of the relevant spatial variables defined in Figure D.4, the mathematical expression of the above argument is found to be

$$\gamma_{cross}(\mathbf{r}, \mathbf{a}) = \gamma_{auto}(\mathbf{r}') = \gamma_{auto}(\mathbf{r} - \mathbf{a}), \quad (\text{D.6})$$

where

$$\begin{aligned} r' &= |\mathbf{r} - \mathbf{a}| \\ &= (r^2 + a^2 - 2ar \cos \alpha)^{1/2}, \\ &\text{when } \max(0, a - 2\sigma) < |r| < a + 2\sigma. \end{aligned} \quad (\text{D.7})$$

Under this condition, α is found to be within the following angular range:

$$0 \leq \alpha \leq \alpha_{\max}, \quad (\text{D.8})$$

where

$$\alpha_{\max} = \cos^{-1} \frac{a^2 + r^2 - 4\sigma^2}{2ar}. \quad (\text{D.9})$$

In other words,

$$\frac{a^2 + r^2 - 4\sigma^2}{2ar} \leq \cos \alpha \leq 1. \quad (\text{D.10})$$

Define $\xi = \cos \alpha$, Eq. (D.7) becomes

$$r' = (r^2 + a^2 - 2ar\xi)^{1/2}. \quad (\text{D.11})$$

If we further define

$$\xi_0 \equiv \frac{a^2 + r^2 - 4\sigma^2}{2ar}, \quad (\text{D.12})$$

and

$$\xi_{\min} = \begin{cases} \xi_0 & \text{when } a + r \geq 2\sigma \\ -1 & \text{when } a + r < 2\sigma \end{cases}, \quad (\text{D.13})$$

from Eq. (D.5) one finds that $\gamma_{cross}(r)$ can be expressed as

$$\begin{aligned} \gamma_{cross}(r, a) &= \gamma_{auto}(r') \\ &= \int_0^\sigma dr_1 \int_0^\sigma dr_2 \int_{\xi_{\min}}^1 d\xi \sqrt{1 - \xi^2} F[r_1, r_2, r', \rho(r)]. \end{aligned} \quad (\text{D.14})$$

Substituting Eqs. (D.5) and (D.14) into Eq. (D.2), $G(z)$ of interacting colloidal system consisting of particles with intraparticle inhomogeneous mass distribution along the radial direction can therefore be numerically calculated, as long as

the mathematical expression of $\rho(r)$ is known.

APPENDIX E

Scattering Amplitude for Icosahedron

Define the following parameters

$$\varphi = \frac{1 + \sqrt{5}}{2}, \quad (\text{E.1})$$

$$\gamma = 3 + \sqrt{5}, \quad (\text{E.2})$$

$$I_{1ij} = (7 + 3\sqrt{5}) Q_i^4 - 4Q_i^2 Q_j^2 + (7 - 3\sqrt{5}) Q_j^4, \quad (\text{E.3})$$

where $i = x, y, z$.

$$I_{2ij\pm\pm} = 2\varphi Q_i \pm (1 - \sqrt{5}) Q_j \pm 2Q_k \quad (\text{E.4})$$

$$I_{3ij\pm} = \sin(\varphi Q_i \pm Q_j), \quad (\text{E.5})$$

$$I_{4ij\pm\pm} = \gamma Q_i \pm (1 - \sqrt{5}) Q_j \pm 2Q_k, \quad (\text{E.6})$$

$$I_{5ij\pm} = \sin\left(\frac{\gamma}{2\varphi} Q_i \pm Q_j\right), \quad (\text{E.7})$$

$$I_{6ij\pm} = 2\varphi Q_i \pm (1 - \sqrt{5}) Q_j, \quad (\text{E.8})$$

$$I_{7ij\pm} = \gamma Q_i^2 \pm (3 - \sqrt{5}) Q_j^2, \quad (\text{E.9})$$

$$I_{8ij\pm} = \sin\left(\frac{2Q_i}{\alpha} \pm Q_j\right), \quad (\text{E.10})$$

$$I_{9ij\pm\pm} = \sin\left[\frac{4Q_i \pm \alpha Q_j \pm 2\varphi Q_k}{2\varphi}\right]. \quad (\text{E.11})$$

The scattering amplitude of the icosahedron, which we denote as F_I , can be expressed as a function of the components of scattering vector \mathbf{Q} along the \hat{x} , \hat{y} and \hat{z} directions (Q_x , Q_y and Q_z respectively). For the sake of mathematical convenience, the triangular edge length of icosahedron a_I is normalized to 2 with a resulting volume $V_I = \frac{10(3+\sqrt{5})}{3}$ and Q_x, Q_y, Q_z are also scaled by the length unit and become dimensionless. The explicit expression of the icosahedral scattering amplitude $F_I =$

$F_I(Q_x, Q_y, Q_z)$ can be analytically expressed in terms of the parameters defined in Eqs. (E.1) to (E.11):

$$\begin{aligned}
F_I = & \frac{8\gamma(Q_x^2 - Q_y^2) \cos(\varphi Q_y) \sin Q_z}{Q_z I_{1xy}} \\
& + \frac{4Q_x}{Q_y(Q_x^2 - Q_y^2)} \left(\frac{I_{3xy-} - I_{3yz+}}{I_{2xy-+}} - \frac{I_{3xy-} + I_{3yz+}}{I_{2xy--}} \right. \\
& \quad \left. + \frac{I_{3yz-} + I_{3yz+}}{I_{2xy++}} + \frac{I_{3xy+} - I_{3yz+}}{I_{2xy+-}} \right) \\
& + \frac{4}{(Q_x^2 - Q_y^2)} \left(\frac{I_{3xy-} + I_{3yz+}}{I_{2xy-+}} + \frac{I_{3xy-} + I_{3yz-}}{I_{2xy--}} \right. \\
& \quad \left. + \frac{I_{3xy+} - I_{3yz-}}{I_{2xy++}} + \frac{I_{3xy+} - I_{3yz+}}{I_{2xy+-}} \right) \\
& - 4\varphi Q_x^2 \left(\frac{I_{5xy-} + I_{5yz+}}{I_{4xz++}} + \frac{I_{5xy-} + I_{5yz-}}{I_{4xz-+}} \right) \\
& \times \left[\frac{12}{(I_{6xy+})(I_{6xy-})(I_{7xy-})} + \frac{\sqrt{5}}{I_{1xy}} \right] \\
& + \left(\frac{I_{5xy-} + I_{5yz+}}{I_{4xz++}} + \frac{I_{5xy-} + I_{5yz-}}{I_{4xz-+}} \right) \\
& \times 4 \left(\frac{7\varphi Q_x^3}{Q_y I_{1xy}} - \frac{3\varphi \sqrt{5} Q_x^3}{Q_y I_{1xy}} + \frac{2\varphi Q_x Q_y}{I_{1xy}} + \frac{3\varphi Q_y^2}{I_{1xy}} - \frac{\sqrt{5}\varphi Q_y^2}{I_{1xy}} \right) \\
& - 4\varphi Q_x^2 \left(\frac{I_{5xy+} + I_{5yz-}}{I_{4xz+-}} + \frac{I_{5xy+} + I_{5yz+}}{I_{4xz--}} \right) \\
& \times \left[\frac{12}{(I_{6xy+})(I_{6xy-})(I_{7xy-})} + \frac{\sqrt{5}}{I_{1xy}} \right] \\
& + \left(\frac{I_{5xy+} + I_{5yz-}}{I_{4xz+-}} + \frac{I_{5xy+} + I_{5yz+}}{I_{4xz--}} \right) \\
& \times 4 \left(\frac{7\varphi Q_x^3}{Q_y I_{1xy}} - \frac{3\varphi \sqrt{5} Q_x^3}{Q_y I_{1xy}} + \frac{2\varphi Q_x Q_y}{I_{1xy}} + \frac{3\varphi Q_y^2}{I_{1xy}} - \frac{\sqrt{5}\varphi Q_y^2}{I_{1xy}} \right) \\
& + \frac{2\alpha}{Q_x^2 - Q_y^2} \left(\frac{I_{8yz-} + I_{3zx+}}{I_{2yz-+}} + \frac{I_{8yz+} - I_{3zx-}}{I_{2yz++}} \right) \\
& - \frac{2\alpha Q_x}{(Q_x^2 - Q_y^2) Q_y} \left(\frac{I_{8yz-} + I_{3zx+}}{I_{2yz-+}} + \frac{I_{8yz+} - I_{3zx-}}{I_{2yz++}} \right) \\
& + \frac{2\alpha}{Q_x^2 - Q_y^2} \left(\frac{-I_{8yz-} - I_{3zx-}}{I_{2zy-+}} + \frac{I_{8zy-} - I_{3zx+}}{I_{2yz--}} \right) \\
& + \frac{2\alpha Q_x}{(Q_x^2 - Q_y^2) Q_y} \left(\frac{I_{8yz-} - I_{3zx-}}{I_{2yz-+}} + \frac{I_{8yz+} - I_{3zx+}}{I_{2yz+-}} \right)
\end{aligned}$$

$$\begin{aligned}
& + \frac{4\varphi}{Q_x^2 - Q_y^2} \left(\frac{I_{8xy-} - I_{9xy--}}{I_{2zx-+}} - \frac{I_{5xy-} - I_{9xy++}}{I_{2zx++}} \right. \\
& \quad \left. + \frac{I_{5xy+} - I_{9xy+-}}{I_{2zx-+}} - \frac{I_{5xy+} + I_{9xy++}}{I_{2zx-+}} \right) \\
& + \frac{4\varphi Q_x}{Q_y(Q_x^2 - Q_y^2)} \left(\frac{I_{8xy-} - I_{9xy--}}{I_{2zx-+}} - \frac{I_{5xy-} - I_{9xy++}}{I_{2zx++}} \right. \\
& \quad \left. + \frac{I_{5xy+} - I_{9xy+-}}{I_{2zx-+}} - \frac{I_{5xy+} + I_{9xy++}}{I_{2zx-+}} \right) \\
& + \frac{4\varphi}{Q_x Q_y} \left(\frac{I_{8yz-} - I_{8zx-}}{I_{2yz+-}} - \frac{I_{8yz-} - I_{8zx-}}{I_{2yz--}} \right. \\
& \quad \left. - \frac{I_{8yz-} - I_{8zx-}}{I_{2yz-+}} - \frac{I_{8yz+} - I_{8zx-}}{I_{2yz++}} \right) \\
& + \frac{4\varphi}{Q_x^2 - Q_y^2} \left(\frac{I_{9xy--} + I_{3zx-}}{I_{2zx--}} + \frac{I_{9xy+-} + I_{3zx-}}{I_{2zx-+}} \right. \\
& \quad \left. + \frac{I_{9xy-+} + I_{3zx+}}{I_{2zx++}} - \frac{I_{9xy++} - I_{3zx+}}{I_{2zx-+}} \right) \\
& + \frac{4\varphi Q_x}{Q_y(Q_x^2 - Q_y^2)} \left(\frac{-I_{9xy++} + I_{5zx+}}{I_{2zx++}} + \frac{I_{9xy-+} - I_{5zx+}}{I_{2zx-+}} \right. \\
& \quad \left. + \frac{I_{9xy-+} - I_{5zx-}}{I_{2zx--}} - \frac{I_{9xy--} + I_{5zx-}}{I_{2zx-+}} \right). \tag{E.12}
\end{aligned}$$

APPENDIX F

Issues about the Structure Characterization in Metallic Systems

There have been several models of $S(Q)$ proposed to describe the spatial correlations of the spherical precipitates forming in the matrix of superalloy systems, including the hard sphere potential [39] and a phenomenological model which circumvents the problem concerning the ill-defined inter-precipitate potential resulting from the validity of the OCM due to the motionlessness of precipitates [40]. As a result, both calculated inter-precipitate structure factors $S(Q)$ show nearly identical quantitative feature around the first interaction peak region, except a slight disagreement in the peak position. The major difference between these two models, as indicated in Figure F.1, is reflected in the higher order correlation peaks of $S(Q)$, which can not be revealed by the corresponding $I(Q)$ (inset of Figure F.1) with the presence of $P(Q)$. Further considering the smearing effect due to the size polydispersity the instrument resolution, it is expected that both models are equally satisfactory in terms of small angle scattering data fitting quality.

In contrast, within the correlation length scales experimentally accessible by SESANS, the corresponding $G(z)$, presented in Figure F.2, obtained from these two models indeed show easily discernible qualitative features. This distinct difference illustrates another example regarding the unique sensitivity of SESANS towards the interparticle interaction, which cannot be achieved by the conventional scattering tools.

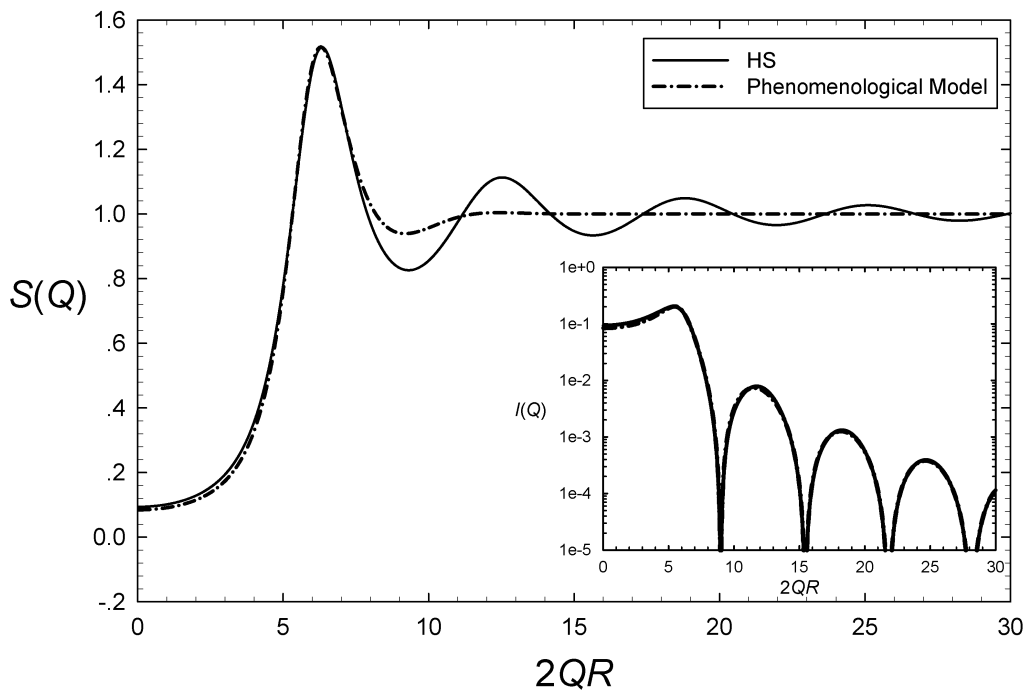


Figure F.1: The inter-precipitate structure factors $S(Q)$ calculated from a HS model with PY closure [12] and a phenomenological one [40]. A reasonably good agreement for the $S(Q)$ in the Q range around the first interaction peak is generally found, which gives rise to the nearly identical $I(Q)$ (inset) with the same $P(Q)$.

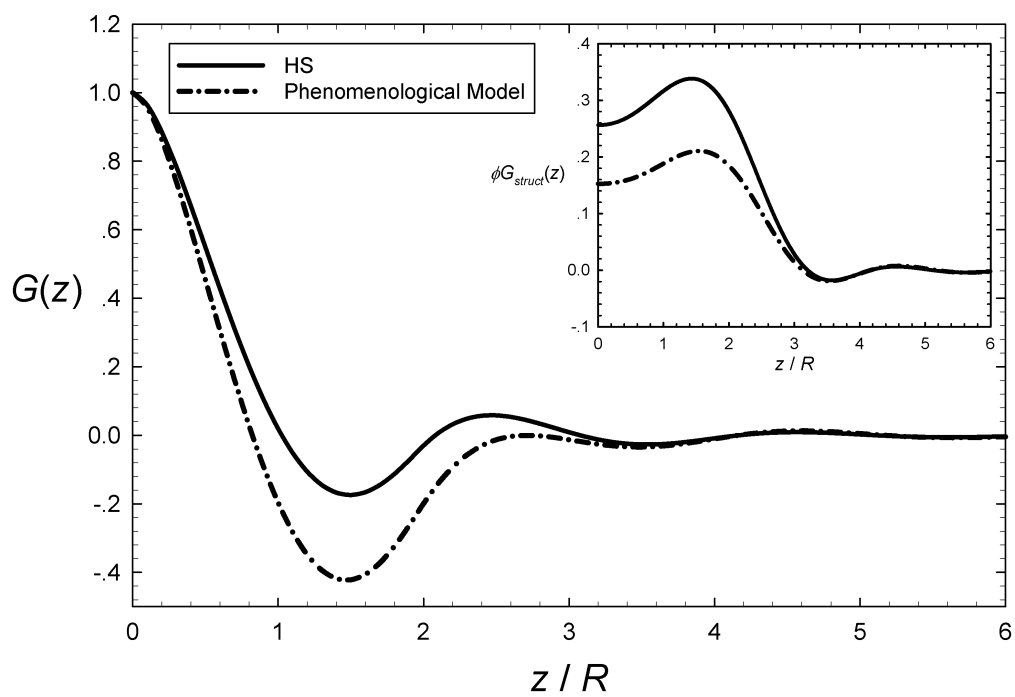


Figure F.2: The corresponding $G(z)$ for the two structural models presented in Figure F.1. A distinct difference between two correlation functions is clearly seen.

APPENDIX G

Issues about the Partial Strucutre Factor in Binary Hard Sphere System

On the basis of the exact solution of the PY closure, the resulting partial structure factor $S_{ij}(Q)$ ($i, j = 1, 2$) of this model system calculated from the OZ equation is analytically expressed as

$$\begin{aligned} S_{11}(Q) &= \frac{1 - n_2 C_{22}(Q)}{1 - n_1 C_{11}(Q) - n_2 C_{22}(Q) + n_1 n_2 C_{11}(Q) C_{22}(Q) - n_1 n_2 C_{12}^2(Q)} \\ S_{22}(Q) &= \frac{1 - n_1 C_{11}(Q)}{1 - n_1 C_{11}(Q) - n_2 C_{22}(Q) + n_1 n_2 C_{11}(Q) C_{22}(Q) - n_1 n_2 C_{12}^2(Q)} \\ S_{12}(Q) &= \frac{\sqrt{n_1 n_2} C_{12}(Q)}{1 - n_1 C_{11}(Q) - n_2 C_{22}(Q) + n_1 n_2 C_{11}(Q) C_{22}(Q) - n_1 n_2 C_{12}^2(Q)}, \end{aligned} \quad (\text{G.1})$$

where $C_{ij}(Q)$ is the Fourier component of $c_{ij}(r)$ and n_i the number density of species i . $C_{ij}(Q)$, and therefore $S_{ij}(Q)$, can be further expressed explicitly as the function of particle size and volume fraction of the constituent components. Details of the derivation can be found elsewhere [31, 32, 33].

Alternatively $S_{ij}(Q)$ of the binary colloidal mixture can be calculated with the closure in which the bridge function $b(r)$ in Eq. (3.11) is incorporated with the following expressions [30]

$$b_{ij}(r) = \begin{cases} -\frac{[h(r)-c(r)]^2}{2\{1+0.8[h(r)-c(r)]\}} & \text{if } h(r) \geq c(r) \\ -\frac{[h(r)-c(r)]^2}{2\{1-0.8[h(r)-c(r)]\}} & \text{if } h(r) < c(r) \text{ and } i \neq j \\ 0 & \text{if } h(r) < c(r) \text{ and } i = j \end{cases}. \quad (\text{G.2})$$

The validity of this numerical scheme for the asymmetric mixture has been rigorously tested against the density functional theory (DFT) with quantitative agreement over a wide range of packing fraction and particle size [30].

The partial structure factor of the first phase (large particles) in the binary

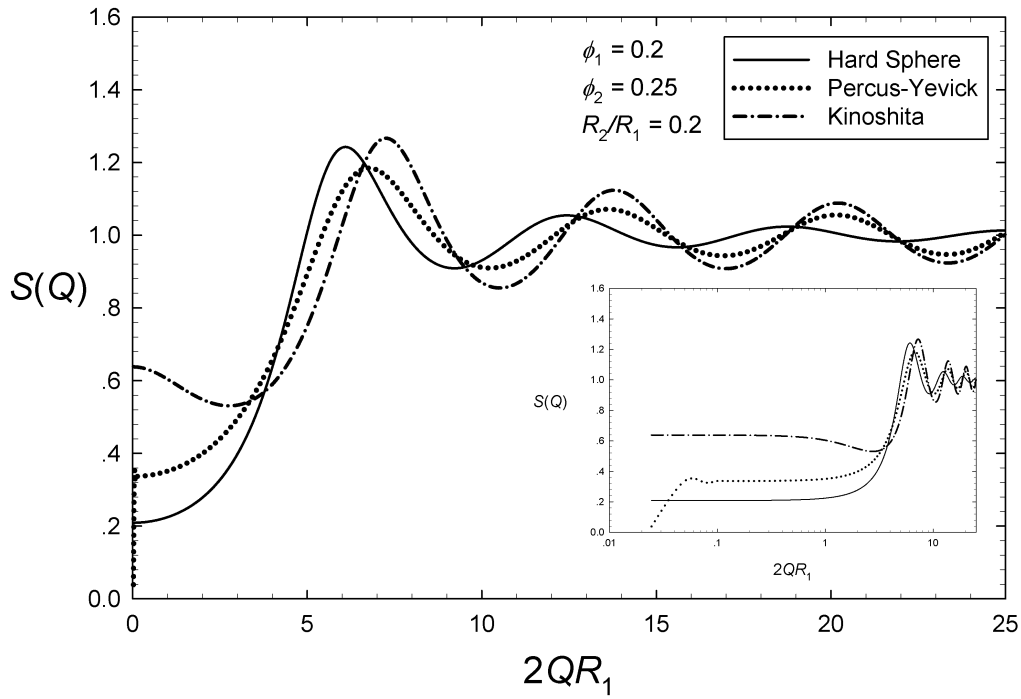


Figure G.1: The total structure factors for an asymmetric colloidal mixture with parameters specified in the figures, along with the reference HS system. In comparison to the $S(Q)$ obtained from the model proposed by Roth and Kinoshita [30], the $S(Q)$ calculated from the OZ/PY approach [31, 32, 33] is seen to underestimate the low- Q enhancement. Moreover, an artificial sudden decrease in the low- Q region of the $S(Q)$ from the solution of OZ/PY approach is clearly observed in the inset.

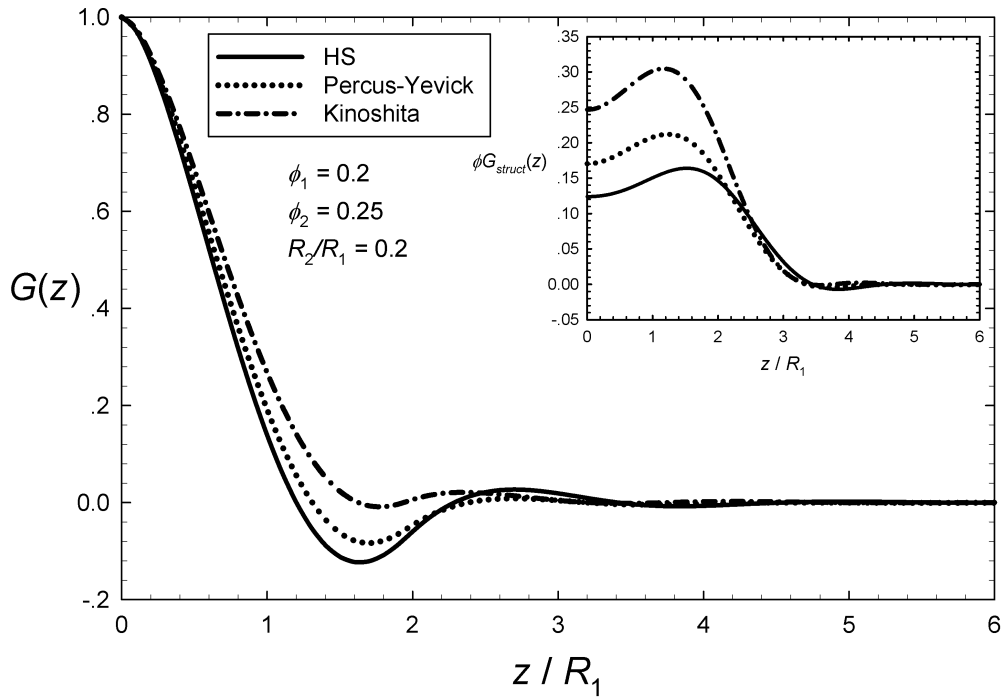


Figure G.2: Consistent with the results presented in Figure G.1, the PY closure is seen to underestimate the short-range correlation due to the underestimation of the short-range attraction.

mixture, $S_{11}(Q)$, is presented in Figure G.1. The reference single component hard sphere structure factor with volume fraction $\phi = 0.2$ is also displayed (solid line, calculated by PY closure). Due to the depletion effect introduced by the presence of the second smaller phase ($\phi_2 = 0.23$, $R_2/R_1 = 0.2$), the interaction peaks of the corresponding structure factors calculated from both approximations are found to shift to the higher Q region in comparison to those of the hard-sphere case. However, probably due to the negligence of $b(r)$ which causes the loss of higher order correlation and the expansion of the closure equation of Eq. (3.11), the PY approach is seen to underestimate the low angle coherent scattering, in comparison

to the more rigorous numerical scheme. Moreover, as shown in the inset, for the the $S_{11}(Q)$ calculated by the PY model, an artificial decrease presenting in the low- Q region is clearly revealed.

APPENDIX H

List of Publications

- X. Li, B. Wu, Y. Liu, R. Pynn, C.-Y. Shew, G. S. Smith, K. W. Herwig, J. L. Robertson, W.-R. Chen and L. Liu, “Contrast variation in spin-echo small angle neutron scattering”, *J. Phys: Condens. Matter* (In Press).
- K. Hong, Y. Liu, L. Porcar, D. Liu, C. Y. Gao, G. S. Smith, K. W. Herwig, S. Cai, X. Li, B. Wu, W.-R. Chen and L. Liu, “Structural response of polyelectrolyte dendrimer toward the molecular protonation: the inconsistence revealed by SANS and NMR”, *J. Phys: Condens. Matter* (In Press).
- X. Li, C.-Y. Shew, L. He, F. Meilleur, D. A. A. Myles, E. Liu, G. S. Smith, K. W. Herwig, R. Pynn and W.-R. Chen, “Scattering functions of Platonic solids”, *J. Appl. Cryst.*, Vol. 44, 2011, pp. 545-557.
- X. Li, C.-Y. Shew, Y. Liu, R. Pynn, E. Liu, K. W. Herwig, G. S. Smith, J. Lee Robertson and W.-R. Chen, “Prospect for characterizing interacting soft colloidal structures using spin-echo small angle neutron scattering”, *J. Chem. Phys.*, Vol. 134, 094504, 2011, pp. 1-13.
- X. Li, M. Zamponi, K. Hong, L. Porcar, C.-Y. Shew, T. Jenkins, L. Liu, G. S. Smith, K. W. Herwig, Y. Liu and W.-R. Chen, “pH Responsiveness of Polyelectrolyte Dendrimers: A Dynamical Perspective”, *Soft Matter*, Vol. 7, 2011, pp. 618-622.
- X. Li, K. Hong, Y. Liu, C.-Y. Shew, L. Liu, K. W. Herwig, G. S. Smith, J. Zhao, G. Zhang, S. Pispas and W.-R. Chen, “Water distributions in PS-b-P(S-g-PEO) block grafted copolymers aggregates in aqueous solutions revealed by contrast variation SANS study”, *J. Chem. Phys.*, Vol. 133, 144912, 2010, pp. 1-8.
- X. Li, C.-Y. Shew, Y. Liu, R. Pynn, L. Liu, K. W. Herwig, G. S. Smith, J. L. Robertson, and W.-R. Chen, “Theoretical studies on the structure of

interacting colloidal suspensions by spin-echo small angle neutron scattering”, *J. Chem. Phys.*, Vol. 132, 174509, 2010, pp. 1-14.

- Y. Liu, L. Porcar, K. Hong, C.-Y. Shew, X. Li, L. Liu, P. D. Butler, K. W. Herwig, G. S. Smith and W.-R. Chen, “Effect of counterion valence on the pH responsiveness of polyamidoamine dendrimer structure”, *J. Chem. Phys.*, Vol. 132, 124901, 2010, pp. 1-6.
- Y. Liu, C.-Y. Chen, H.-L. Chen, K. Hong, C.-Y. Shew, X. Li, L. Liu, K. W. Herwig, G. S. Smith, L. Porcar and W.-R. Chen, “Electrostatic Swelling and Conformational Variation Observed in High-Generation Polyelectrolyte Dendrimers”, *J. Phys. Chem. Lett.*, Vol. 1, 2010, pp. 2020-2024.